Research & Technology Transfer

# Condition Dependent Performance Based Seismic Design – Phase 1

## FINAL REPORT



**Prepared by:**
**David Comaniciu, M.S.**
**Mervyn Kowalsky, Ph.D., Principal Investigator**
**Moe Pourghaz, Ph.D., Principal Investigator**

**Raleigh, North Carolina**
**Report # FHWA-AK-RD-4000(211)**
**March 14th, 2025**

**Prepared for:**
Alaska Department of Transportation & Public Facilities Statewide Research Office
3132 Channel Drive
Juneau, AK 99801-7898

# REPORT DOCUMENTATION PAGE

Form approved OMB No.

Public reporting for this collection of information is estimated to average 1 hour per response, including the time for reviewing instructions, searching existing data sources, gathering and maintaining the data needed, and completing and reviewing the collection of information. Send comments regarding this burden estimate or any other aspect of this collection of information, including suggestion for reducing this burden to Washington Headquarters Services, Directorate for Information Operations and Reports, 1215 Jefferson Davis Highway, Suite 1204, Arlington, VA 22202-4302, and to the Office of Management and Budget, Paperwork Reduction Project (0704-1833), Washington, DC 20503

| 1. AGENCY USE ONLY (LEAVE BLANK) | 2. REPORT DATE | 3. REPORT TYPE AND DATES COVERED |
|---|---|---|
| FHWA-AK-RD-4000(211) | March 14th, 2025 | Final Report, June 2022 through November 2024 |

4. TITLE AND SUBTITLE

Condition Dependent Performance Based Seismic Design – Phase 1

5. FUNDING NUMBERS

HFHWY00267
FHWA-AK-RD-4000(211)

6. AUTHOR(S)

David Comaniciu, M.S.
Mervyn J. Kowalsky, Ph.D., Principal investigator
Moe Pourghaz, Ph.D., Principal investigator

7. PERFORMING ORGANIZATION NAME(S) AND ADDRESS(ES)

Department of Civil, Construction, and Environmental Engineering
North Carolina State University
Raleigh, NC 27606

8. PERFORMING ORGANIZATION REPORT NUMBER

9. SPONSORING/MONITORING AGENCY NAME(S) AND ADDRESS(ES)

State of Alaska, Alaska Dept. of Transportation and Public Facilities
Research and Technology Transfer
3132 Channel Drive
Juneau, AK 99801-7898

10. SPONSORING/MONITORING AGENCY REPORT NUMBER

FHWA-AK-RD-4000(211)

11. SUPPLEMENTARY NOTES

12a. DISTRIBUTION / AVAILABILITY STATEMENT

No restrictions

12b. DISTRIBUTION CODE

N/A

13. ABSTRACT (Maximum 200 words)

This report investigates the seismic performance of corroded reinforced concrete (RC) bridge columns, focusing on how corrosion affects material degradation and overall structural response. Corrosion of reinforcing steel, a prevalent issue in coastal and cold regions, severely impacts the structural integrity of bridges, particularly under seismic loads. The research integrates both material-level tests and largescale column tests, with varying corrosion levels up to 50%, to evaluate the mechanical and global effects of corrosion. Four large-scale RC columns were subjected to quasi-static cyclic loading to mimic seismic conditions. Corroded specimens showed reduced strength, stiffness, and energy dissipation capacity compared to uncorroded counterparts, and failure was dominated by buckling and fracture of longitudinal reinforcement. A portable 3D scanner was employed to measure pitting and mass loss in corroded bars, allowing for precise quantification of material degradation. This method provided critical data for correlating the material-level corrosion effects with the global seismic performance of the columns. The findings highlight the necessity of incorporating corrosion effects into seismic design and retrofitting strategies, with recommendations provided for future research and practical design considerations. The results contribute to performance-based seismic design frameworks, offering insights for more resilient infrastructure in environments prone to corrosion and seismic activity.

14- KEYWORDS :

Corrosion, Seismic Performance, Material Degradation, 3D Scanning, Large-Scale Tests, Material Tests

15. NUMBER OF PAGES

157

16. PRICE CODE

N/A

| 17. SECURITY CLASSIFICATION OF REPORT | 18. SECURITY CLASSIFICATION OF THIS PAGE | 19. SECURITY CLASSIFICATION OF ABSTRACT | 20. LIMITATION OF ABSTRACT |
|---|---|---|---|
| Unclassified | Unclassified | Unclassified | N/A |



# Constructed Facilities Laboratory

Environmental Engineering

Research Report
No. RD-24-4000(211)

# CONDITION DEPENDENT PERFORMANCE BASED SEISMIC DESIGN – PHASE 1

## Prepared by:

**David Comaniciu, M.S.**
**Mervyn Kowalsky, Ph.D., Principal Investigator**
**Moe Pourghaz, Ph.D., Principal Investigator**

## Prepared for:

**Alaska Department of Transportation and Public Facilities (AKDOT&PF)**

**Constructed Facilities Laboratory**
**2414 Campus Shore Drive**
**North Carolina State University**
**Raleigh, NC 27695-7533**
**Tel: (919) 513-1733**
**Fax: (919) 513-1765**
**Email: cfl@ncsu.edu**
**Web Site: www.cfl.ncsu.edu**

November 2024

# CONDITION DEPENDENT PERFORMANCE BASED SEISMIC DESIGN – PHASE 1

## Final Report

March 2025

*The research described in this report is supported by the Alaska Department of Transportation and Public Facilities. Their support is gratefully acknowledged. The conclusions are those of the authors alone and should not be construed as to imply endorsement by AKDOT&PF.*

**Notice**

This document is disseminated under the sponsorship of the U.S. Department of Transportation in the interest of information exchange. The U.S. Government assumes no liability for the use of the information contained in this document. The U.S. Government does not endorse products or manufacturers. Trademarks or manufacturers' names appear in this report only because they are considered essential to the objective of the document.

**Quality Assurance Statement**

The Federal Highway Administration (FHWA) provides high-quality information to serve Government, industry, and the public in a manner that promotes public understanding. Standards and policies are used to ensure and maximize the quality, objectivity, utility, and integrity of its information. FHWA periodically reviews quality issues and adjusts its programs and processes to ensure continuous quality improvement.

**Author's Disclaimer**

Opinions and conclusions expressed or implied in the report are those of the author. They are not necessarily those of the Alaska DOT&PF or funding agencies.

# EXECUTIVE SUMMARY

This research investigates the seismic performance of corroded reinforced concrete (RC) bridge columns, focusing on how corrosion affects material degradation and overall structural response. Corrosion of reinforcing steel, a prevalent issue in coastal and cold regions due to chloride exposure, severely impacts the structural integrity of bridges, particularly under seismic loads. This research integrates both material-level tests and large-scale column tests, with varying corrosion levels up to 50%, to evaluate the mechanical and global effects of corrosion. Four large-scale RC columns were subjected to quasi-static cyclic loading to mimic seismic conditions. Corroded specimens showed reduced strength, stiffness, and energy dissipation capacity compared to uncorroded counterparts, and failure was dominated by buckling and fracture of longitudinal reinforcement. A portable 3D scanner was employed to measure pitting and mass loss in corroded bars, allowing for precise quantification of material degradation and correlation to global seismic performance of the columns. The findings highlight the necessity of incorporating corrosion effects into seismic design and retrofitting strategies, with recommendations provided for future research and practical design considerations. The results contribute to performance-based seismic design frameworks, offering insights for more resilient infrastructure in environments prone to corrosion and seismic activity.

# TABLE OF CONTENTS

**EXECUTIVE SUMMARY** ..... **VII**
**TABLE OF CONTENTS** ..... **VIII**
**LIST OF TABLES** ..... **XI**
**LIST OF FIGURES** ..... **XII**
**LIST OF SYMBOLS** ..... **XVI**
**CHAPTER 1: INTRODUCTION** ..... **1**
1.1 BACKGROUND ..... 1
1.2 RESEARCH OBJECTIVE ..... 2
1.3 SCOPE ..... 2
*1.3.1 Column Tests* ..... *2*
*1.3.2 Material Tests* ..... *2*
1.4 OVERVIEW OF FOLLOWING REPORT CONTENTS ..... 3
**CHAPTER 2: LITERATURE REVIEW** ..... **4**
2.1 STRESS-STRAIN RELATIONSHIP ..... 4
2.2 IMPACTS OF CORROSION ON MATERIAL AND MEMBER RESPONSE ..... 6
*2.2.1 Almusallam, A. A. (2001)* ..... *6*
*2.2.2 Kashani et al. (2012)* ..... *9*
2.3 IMPACTS OF CORROSION ON THE STRUCTURAL LEVEL ..... 12
*2.3.1 Meda et al. (2014)* ..... *12*
*2.3.2 Andisheh et al. (2021)* ..... *15*
2.4 DISCUSSION AND KNOWLEDGE GAPS ..... 18
**CHAPTER 3: STRUCTURAL MEMBER CHARACTERIZATION** ..... **19**
3.1 TEST SPECIMENS AND CONSTRUCTION ..... 19
*3.1.1 Column Test Specimens* ..... *19*
*3.1.2 Accelerated Corrosion* ..... *21*
*3.1.2 Column Construction* ..... *24*
3.2 EXPERIMENTAL TEST SETUP ..... 29
*3.2.1 Test Setup* ..... *29*
*3.2.2 Instrumentation* ..... *31*
*3.2.3 Load Protocol* ..... *31*
**CHAPTER 4: SUMMARY OF COLUMN TESTS** ..... **33**
4.1 COLUMN TEST 1 SUMMARY ..... 33
*4.1.1 Damage Progression* ..... *36*
*4.1.2 Special Note About Column Test 1* ..... *43*

*4.1.3 Hysteretic Energy Dissipation* ..... *44*
4.2 COLUMN TEST 2 SUMMARY ..... 46
*4.2.1 Damage Progression* ..... *49*
*4.2.2 Strain Analysis* ..... *54*
*4.2.3 Components of Displacement* ..... *57*
*4.2.4 Hysteretic Energy Dissipation* ..... *60*
*4.2.5 Strain Limit States* ..... *61*
4.3 COLUMN TEST 3 SUMMARY ..... 63
*4.4.1 Damage Progression* ..... *66*
*4.4.2 Strain Analysis* ..... *70*
*4.4.3 Components of Displacement* ..... *73*
*4.4.4 Hysteretic Energy Dissipation* ..... *76*
*4.4.5 Strain Limit States* ..... *76*
4.4 COLUMN TEST 4 SUMMARY ..... 78
*4.3.1 Damage Progression* ..... *81*
*4.3.2 Strain Analysis* ..... *87*
*4.3.3 Components of Displacement* ..... *88*
*4.3.4 Hysteretic Energy Dissipation* ..... *91*
*4.3.5 Strain Limit States* ..... *91*

**CHAPTER 5: MATERIAL LEVEL CHARACTERIZATION ..... 93**

5.1 TENSION TESTS ..... 93
*5.1.1 Tension Test Procedure* ..... *93*
*5.1.2 Tension Test Results* ..... *93*
5.2 BUCKLED BAR TENSION TESTS ..... 94
*5.2.1 Buckled Bar Tension Test Procedure* ..... *94*
*5.2.2 BBT Test Results* ..... *96*
5.3 THREE-DIMENSIONAL SCANNING OF CORRODED BARS ..... 98
*5.3.1 Scanning of Large-Scale Tests* ..... *98*
*5.3.2 Column Test Scanning Results* ..... *100*
*5.3.3 Scanning of Material Test Specimens* ..... *101*
*5.3.4 Material Test Scanning Results* ..... *101*

**CHAPTER 6: RESULTS AND CORRELATION BETWEEN LARGE-SCALE TESTS AND MATERIAL TESTS ..... 106**

6.1 LARGE-SCALE TESTS RESULTS ..... 107
*6.1.1 Global Response* ..... *107*
*6.1.2 Axial Strain Demands* ..... *113*
*6.1.3 Damage Limit States* ..... *116*
*6.1.4 Bending Strain* ..... *117*
*6.1.5 Cumulative Energy Dissipation* ..... *119*
6.2 LARGE-SCALE TESTS AND MATERIAL TESTS ..... 119

**CHAPTER 7: SUMMARY AND DESIGN RECOMMENDATIONS ..... 122**

7.1 CONCLUSIONS ..... 122
7.2 DESIGN RECOMMENDATIONS ..... 123

**CHAPTER 8: REFERENCES** ..... **125**

**APPENDICES** ..... **128**

**APPENDIX A: STANDARD OPERATION PROCEDURE FOR ACCELERATED CORROSION** ..... **129**

*Chemicals and Equipment* ..... *129*
*Safety Equipment* ..... *130*
*Procedure* ..... *130*
*Cleaning Procedure* ..... *132*

**APPENDIX B: STANDARD OPERATION PROCEDURE FOR 3D SCANNING** ..... **134**

*Equipment and Software* ..... *134*
*Procedure* ..... *134*

**APPENDIX C: 3D SCAN RESULTS** ..... **137**

*Tension Tests* ..... *137*
*BBT Tests* ..... *137*
*Large-Scale Tests* ..... *138*

**APPENDIX D: DATA FROM PREVIOUS RESEARCH** ..... **140**

# LIST OF TABLES

Table 2-1: Summary of corrosion duration of test specimens. Kashani et al. (2012) ..... 9
Table 2-2: Bar specimens. Meda et al. (2014) ..... 12
Table 2-3: Cyclic test results. Meda et al. (2014) ..... 14
Table 2-4: Experimental corrosion test results and theoretical prediction results. Andisheh et al. (2021) ..... 15
Table 3-1: Displacement ductility ..... 32
Table 4-1: Column test 1 parameters and results summary ..... 33
Table 4-2: Column test 1 material tension test results ..... 34
Table 4-3: Column test 1 concrete compression strength results ..... 35
Table 4-4: Column test 2 parameters and results summary ..... 46
Table 4-5: Column test 2 material tension test results ..... 47
Table 4-6: Column test 2 concrete compression strength results ..... 47
Table 4-7: Performance limit states. Kowalsky (2000) ..... 61
Table 4-8: Column test 2 strain at damage limit states ..... 62
Table 4-9: Column test 3 parameters and results summary ..... 63
Table 4-10: Column test 3 material tension test results ..... 64
Table 4-11: Column test 3 concrete compression strength results ..... 64
Table 4-12: Column test 3 strain at damage limit states ..... 77
Table 4-13: Column test 4 parameters and results summary ..... 78
Table 4-14: Column test 4 material tension test results ..... 79
Table 4-15: Column test 4 concrete compression strength results ..... 79
Table 4-16: Column test 4 strain at damage limit states ..... 92
Table 5-1: BBT test matrix ..... 96
Table 6-1: Column test matrix ..... 106
Table 6-2: Axial tension strain summary ..... 113
Table 6-3: Axial compression strain summary ..... 113
Table 6-4: Damage limit states comparison ..... 116
Table 6-5: Comparison summary critical bending strains of BBT vs. column tests ..... 120
Table 6-6: Critical bending strains and 3D scans ..... 121

# LIST OF FIGURES

Figure 2-1: Stress-strain model proposed for monotonic loading of confined and unconfined concrete. Mander et al. (1988b) ..... 5
Figure 2-2: Schematic representation of the accelerated corrosion test setup. Almusallam (2001)6
Figure 2-3: Load-elongation curves for 6-mm diameter steel bars with varying degrees of corrosion. Almusallam (2001) ..... 7
Figure 2-4: Effect of 75% corrosion on rebar configuration. Almusallam (2001) ..... 8
Figure 2-5: Mean stress-strain curves of tension tests for the 8 mm diameter. Kashani et al. (2012) ..... 10
Figure 2-6: Trend lines of test experiments of all groups of bars: (a) yield stress; (b) ultimate stress. Kashani et al. (2012) ..... 11
Figure 2-7: Load-strain relationship and bars after the test. Meda et al. (2014) ..... 13
Figure 2-8: Cyclic behaviour: horizontal load versus horizontal displacement. Meda et al. (2014) ..... 14
Figure 2-9: Stress-strain relationship of concrete with varying degrees of corrosion and confinement arrangements. Andisheh et al. (2021) ..... 17
Figure 3-1: Test specimen geometry ..... 19
Figure 3-2: Footing reinforcement plan ..... 20
Figure 3-3: Reinforcement details ..... 20
Figure 3-4: Accelerated corrosion process ..... 21
Figure 3-5: Corrosion setup: (a) material tests; (b) large-scale tests ..... 23
Figure 3-6: Column cage construction: (a) longitudinal bars inside of spiral; (b) longitudinal bars attached in circular configuration to plywood forms; (c) spiral tying; (d) spiral tying close-up .. 24
Figure 3-7: Footing construction: (a) footing formwork with block outs; (b) completed footing top view; (c) completed footing side view ..... 25
Figure 3-8: Footing casting: (a) pouring of concrete; (b) concrete setting ..... 26
Figure 3-9: Column and cap beam construction and casting: (a) concrete cover block-out for test instrumentation; (b) placing form tube on column cage; (c) capbeam frame; (d) casting column and capbeam; (e) cleaning column; (f) final column ..... 28
Figure 3-10: Loading sign convention and extreme longitudinal bar labeling ..... 29
Figure 3-11: Test setup: (a) side view; (b) front view ..... 30
Figure 3-12: Actual test setup ..... 30
Figure 3-13: Optotrak markers ..... 31
Figure 4-1: Column test 1 stress-strain response material tests ..... 34
Figure 4-2: Column test 1 force-displacement response ..... 35
Figure 4-3: Column test 1 load history ..... 36
Figure 4-4: Column test 1 crack distribution end of ductility one: (left) south side; (right) north side ..... 37
Figure 4-5: Column test 1 crack distribution end of ductility two: (left) south side; (right) north side ..... 38
Figure 4-6: Column test 1 crack distribution end of ductility three: (left) south side; (right) north side ..... 38
Figure 4-7: Column test 1 crushing of concrete ductility four: (left) south side; (right) north side ..... 39
Figure 4-8: Column test 1 early signs of buckling ductility five - bar S3 ..... 40

Figure 4-9: Column test 1 signs of buckling ductility six: (left) bar S3; (right) bar N3 ..... 40
Figure 4-10: Column test 1 fractured bars ductility seven: (left) bar N3; (right) bar N2 ..... 41
Figure 4-11: Column test 1 fractured bars ductility seven: (left) bar S4; (right) bar S3..... 41
Figure 4-12: Column test 1 fractured bars after test: (left) bar N3; (right) bar N2..... 42
Figure 4-13: Column test 1 fractured bars after test: (left) bar S4; (right) bar S3 ..... 42
Figure 4-14: Jacobsen's damping calculation example ..... 44
Figure 4-15: Column test 1 hysteretic damping..... 45
Figure 4-16: Column test 2 stress-strain response material tests..... 47
Figure 4-17: Column test 2 force-displacement response..... 48
Figure 4-18: Column test 2 load history ..... 49
Figure 4-19: Column test 2 crack distribution end of ductility one: (left) south side; (right) north side ..... 50
Figure 4-20: Column test 2 crack distribution end of ductility two: (left) south side; (right) north side ..... 51
Figure 4-21: Column test 2 crack distribution end of ductility three: (left) south side; (right) north side ..... 51
Figure 4-22: Column test 2 crushing of concrete ductility four: (left) south side; (right) north side ..... 52
Figure 4-23: Column test 2 buckling during ductility six: (left) bar N3; (right) bar S3 ..... 53
Figure 4-24: Column test 2 fractured bar ductility seven – bar N3 ..... 53
Figure 4-25: Column test 2 fractured bar ductility seven – bar S3..... 54
Figure 4-26: Column test 2 strain profiles after yield: (a) bar N3; (b) bar S3 ..... 55
Figure 4-27: Column test 2 strain vs. displacement: (a) bar N3; (b) bar S3..... 56
Figure 4-28: LEDs on buckled bar..... 57
Figure 4-29: Column test 2 bond slip of extreme fiber bars: (a) south side under push cycles; (b) north side under pull cycles ..... 58
Figure 4-30: Column test 2 curvature profile ..... 59
Figure 4-31: Column test 2 components of displacement ..... 60
Figure 4-32: Column test 2 hysteretic damping..... 61
Figure 4-33: Column test 3 stress-strain response material tests..... 64
Figure 4-34: Column test 3 force-displacement response..... 65
Figure 4-35: Column test 3 load history ..... 66
Figure 4-36: Column test 3 crack distribution end of ductility one: (left) south side; (right) north side ..... 67
Figure 4-37: Column test 3 crack distribution end of ductility two: (left) south side; (right) north side ..... 67
Figure 4-38: Column test 3 crushing of concrete ductility three: (left) south side; (right) north side ..... 68
Figure 4-39: Column test 3 buckling during ductility six: (left) bar S3; (right) bar N3 ..... 69
Figure 4-40: Column test 3 fractured bar ductility six – bar S3 ..... 69
Figure 4-41: Column test 3 fractured bar ductility seven – bar N3 ..... 70
Figure 4-42: Column test 3 fractured bar ductility seven – bar N2 ..... 70
Figure 4-43: Column test 3 strain profiles after yield: (a) bar N3; (b) bar S3 ..... 71
Figure 4-44: Column test 3 strain vs. displacement: (a) bar N3; (b) bar S3; (c) bar N2 ..... 72
Figure 4-45: Column test 3 bond slip of extreme fiber bars: (a) south side under push cycles; (b) north side under pull cycles ..... 74

Figure 4-46: Column test 3 curvature profile ..... 75
Figure 4-47: Column test 3 components of displacement ..... 75
Figure 4-48: Column test 3 hysteretic damping..... 76
Figure 4-49: Column test 4 stress-strain response material tests..... 79
Figure 4-50: Column test 4 force-displacement response..... 80
Figure 4-51: Column test 4 load history ..... 81
Figure 4-52: Column test 4 crack distribution end of ductility one: (left) south side; (right) north side ..... 82
Figure 4-53: Column test 4 crack distribution end of ductility two: (left) south side; (right) north side ..... 83
Figure 4-54: Column test 4 crushing of concrete ductility three - south side..... 83
Figure 4-55: Column test 4 fractured bar during ductility three – bar S3..... 84
Figure 4-56: Column test 4 buckling during ductility five – bar N3 ..... 85
Figure 4-57: Column test 4 fractured bar ductility six – bar N3..... 85
Figure 4-58: Column test 4 fractured bar ductility six – bar S2 ..... 86
Figure 4-59: Column test 4 fractured bar ductility six – bar N2..... 86
Figure 4-60: Column test 4 strain profiles after yield: (a) bar N3; (b) bar S3 ..... 87
Figure 4-61: Column test 4 strain vs. displacement: (a) bar N3; (b) bar S3 ..... 88
Figure 4-62: Column test 4 bond slip of extreme fiber bars: (a) south side under push cycles; (b) north side under pull cycles ..... 89
Figure 4-63: Column test 4 curvature profile ..... 90
Figure 4-64: Column test 4 components of displacement ..... 90
Figure 4-65: Column test 4 hysteretic damping..... 91
Figure 5-1: Tension test results – stress vs. strain at different corrosion levels ..... 93
Figure 5-2: BBT test sequence. Barcley and Kowalsky (2019)..... 94
Figure 5-3: BBT failure types: (a) ductile failure; (b) brittle failure ..... 95
Figure 5-4: BBT results – bending strain at different corrosion levels..... 97
Figure 5-5: Portable 3D scanner ..... 98
Figure 5-6: Scanning of large-scale columns: (a) scanning column; (b) scanner interface..... 99
Figure 5-7: Measuring column pit geometry – units not to scale ..... 100
Figure 5-8: Pit depth and bar diameter ratio versus bending strain before fracture ..... 101
Figure 5-9: Pit depth and bar diameter ratio versus maximum tensile stress ..... 102
Figure 5-10: Pit depth and bar diameter ratio versus strain at fracture..... 103
Figure 5-11: Pit depth and bar diameter ratio versus bending strain ..... 104
Figure 5-12: Comparison of column tests and BBT pit depth and bar diameter ratio versus bending strain equations ..... 105
Figure 6-1: Load history comparison of all column tests ..... 109
Figure 6-2: Backbone comparison of all column tests: (a) first cycle; (b) third cycle ..... 110
Figure 6-3: Comparison of experimental vs. CUMBIA backbone curve: (a) 5% corrosion; (b) 10% corrosion; (c) 30% corrosion; (d) 50% corrosion..... 112
Figure 6-4: Tension strain profiles: (a) 5% corrosion; (b) 30% corrosion; (c) 50% corrosion .. 115
Figure 6-5: Compression strain profiles: (a) 5% corrosion; (b) 30% corrosion; (c) 50% corrosion ..... 116
Figure 6-6: Column tests bending strain history: red – 5% corrosion; orange – 30% corrosion; green – 50% corrosion ..... 118
Figure 6-7: Energy dissipation comparison ..... 119

Figure 6-8: Comparison of critical bending strains of BBT vs. column tests..... 120

# LIST OF SYMBOLS

| | |
|---|---|
| $f_{c'}$ | Concrete Compressive Strength |
| $f_u$ | Ultimate Stress of Longitudinal Steel |
| $F_{y'}$ | First Yield Force of Column |
| $g$ | Gravitational Constant |
| $L$ | Height of Column |
| $L_c$ | Clear Height of Column |
| $L_{eff}$ | Effective Length |
| $L/D$ | Column Aspect Ratio (AR) |
| $L_p$ | Equivalent Plastic Hinge Length |
| $L_0$ | Initial Length |
| $P$ | Column Axial Load |
| $\Delta_{max}$ | Maximum Displacement |
| $\Delta_y$ | Column Displacement at First Yield |
| $\Delta_y$ | Column Displacement at Equivalent Yield |
| $\Delta\varepsilon_{cr}$ | Range of Critical Bending Strain |
| $\varepsilon$ | Axial Strain of Steel |
| $\varepsilon_b$ | Bending Strain |
| $\varepsilon_c$ | Axial Compression Strain of Steel |
| $\xi_{hyst}$ | Hysteretic Damping |
| $\mu\Delta$ | Displacement Ductility of Column |
| $\rho_l$ | Longitudinal Steel Ratio |
| $\rho_s$ | Transverse Volumetric Steel Ratio |
| φ | Curvature |

# CHAPTER 1: INTRODUCTION

## 1.1 Background

One of the greatest challenges faced by bridge engineers today is the continuous deterioration of reinforced concrete (RC) bridges that play a vital role in our infrastructure. One of the most common deterioration mechanisms found in RC bridges is the corrosion of reinforcing steel. The corrosion of steel is primarily caused by the presence of extreme amounts of chloride in the air and seawater (Mohammed et al., 2016). Bridges subjected to such environmental conditions are most commonly found in coastal regions where the salinity content in the air is high and where structures may be physically located in salt water, or in cold regions where excessive amounts of de-icing salts are used. Many of these bridges are also located in regions with high seismic activity, which further increases the risk of failure. As a result, careful consideration must be given to the effect that corrosion will have on the nonlinear response of these bridges (Kashani et al., 2012).

The corrosion of steel in concrete is an electrochemical process that involves the oxidation of steel at the interface between the steel and concrete (Ghods et al., 2009). The concrete surrounding the reinforcing steel provides a highly alkaline environment (pH > 13.0), in which the steel is protected by a passive oxide film (Muthulingam & Rao, 2014). In addition, the concrete provides a physical barrier from the chlorides. Although small amounts of material loss in the reinforcing steel is expected, corrosion generally does not become a concern until the chloride content at the concrete steel interface reaches a critical threshold which destroys the protective layer (Muthulingam & Rao, 2014). With the passive layer gone, depassivation begins and the steel is more susceptible to higher rates of corrosion. According to Ghods et al. (2006), some of the other components that affect the depassivation and corrosion of the steel include “pH of the pore solution around the reinforcement, the physical and chemical properties of the concrete, surface characteristics and the chemical composition of the steel, and the presence of mechanical stresses” (p. 2).

High corrosion rates in RC structures lead to increased material loss, affecting structural integrity. Previous research has shown that corrosion will modify the mechanical properties of reinforcing steel (Yuan et al., 2017). Consequences of corrosion include a reduction in the bond between the concrete and steel as well as loss of steel cross-sectional area. Prior studies on

corroded reinforcing steel have revealed a reduction in strength and elongation and a decrease in ductility which can lead to more brittle failures (Zhao et al., 2011).

## 1.2 Research Objective

This report aims to contribute to the existing body of literature on the seismic performance of corroded reinforced concrete columns. The aims of this study are to: (1) Investigate the influence of corrosion on the seismic performance of bridge columns through large-scale experiments; (2) Validate mechanical degradation models integrated within a computational framework; (3) Outline the parameters for upcoming project stages.

## 1.3 Scope

In order to further understand the effects that corrosion has on the seismic performance of reinforced concrete columns, material tests with corroded steel as well as large-scale tests with corroded longitudinal steel were performed. The results from the material tests and large-scale tests were compared to tests with uncorroded steel.

### *1.3.1 Column Tests*

Four large-scale circular reinforced concrete columns were constructed and tested in the Constructed Facilities Laboratory (CFL) at North Carolina State University (NC State). The four columns featured different levels of corrosion (defined by material loss) in the plastic hinge. All the columns were subjected to a three-cycle quasi-static loading protocol using a hydraulic actuator. To measure strain in longitudinal and transverse steel, an optical 3D measurement system was utilized. The system used was Optotrak Certus HD, a camera system capable of capturing three-dimensional spatial coordinate history of LED markers.

### *1.3.2 Material Tests*

Various material tests were performed on corroded reinforcing steel samples. Material tests included tension tests and Buckled Bar Tension (BBT) tests. Optotrak Certus HD was used to measure the strain in the test specimens.

## 1.4 Overview of Following Report Contents

**Chapter two** covers a literature review of past experimental work on corrosion on the material and structural level. This chapter also includes a discussion of the gaps of knowledge in the literature.

**Chapter three** discusses the design and construction of the four large-scale columns. This chapter also discusses the test setup including instrumentation used and loading protocol.

**Chapter four** covers the results from each column test. Each column test includes a summary of strength, displacement, and strain at various performance level states.

**Chapter five** outlines the material level characterization, including Tension tests, and Bucked Bar Tension tests. In addition, the use of 3D scanning for quantifying corrosion is discussed.

**Chapter six** aims to find the connection between the material tests and the large-scale tests.

**Chapter seven** summarizes the design recommendations for preventing corrosion, as well as assessing when intervention is needed for current structures with corrosion.

**Appendix A** outlines the standard operating procedure (SOP) for accelerated corrosion that was used during this research project.

**Appendix B** outlines the standard operating procedure (SOP) for 3D scanning and processing corroded steel specimens.

**Appendix C** presents the results from the 3D scans of both the material tests and the large-scale tests.

**Appendix D** presents data from previous research conducted at NC. This section aims to provide comparisons with the research presented in this report.

# CHAPTER 2: LITERATURE REVIEW

The corrosion of steel in reinforced concrete (RC) columns found in structures such as bridges can lead to a significant reduction in service life as well as unexpected failure. These concerns are further elevated in high seismic regions where structures are subjected to large cyclic dynamic loads. Understanding how corrosion affects such structures can lead to advances in future design as well as improvements to current structures. The purpose of this literature review is to provide a brief overview of corrosion in RC columns followed by an in-depth discussion on the impacts that corrosion has on material, member, and structural response. Although corrosion is the main focus, the overall goal of this literature review is to assess the impacts that corrosion has on the seismic behavior of systems, rather than just a review of everything related to corrosion. A series of papers will be reviewed that discuss the following topics: the stress-strain relationship of confined RC columns as well as the ductility, buckling, and subsequent fracture of reinforcement. The chapter concludes with a synthesis of the literature and identification of knowledge gaps that informed the conduct of the research described in this report.

## 2.1 Stress-Strain Relationship

In the seismic design of RC columns, careful consideration must be taken to ensure that seismic capacity in the plastic hinge region is greater than the demand. To meet the required capacity and ductility demands, sufficient transverse reinforcement is needed to properly confine the compressed concrete (Mander et al., 1988b). According to Andisheh et al. (2021), the effects of transverse confinement were first studied in detail by Richart et al. (1928, 1929), who proposed an early stress-strain model. Since then, multiple stress-strain models have been proposed, the most famous and widely accepted one being developed by Mander et al. in 1988. The model proposed by Mander et al. (1988b) can be used to predict the stress-strain behavior of RC columns with various configurations of confining steel such as spiral, circular, or rectangular hoops. The proposed stress-strain model is illustrated in Figure 2-1 below:

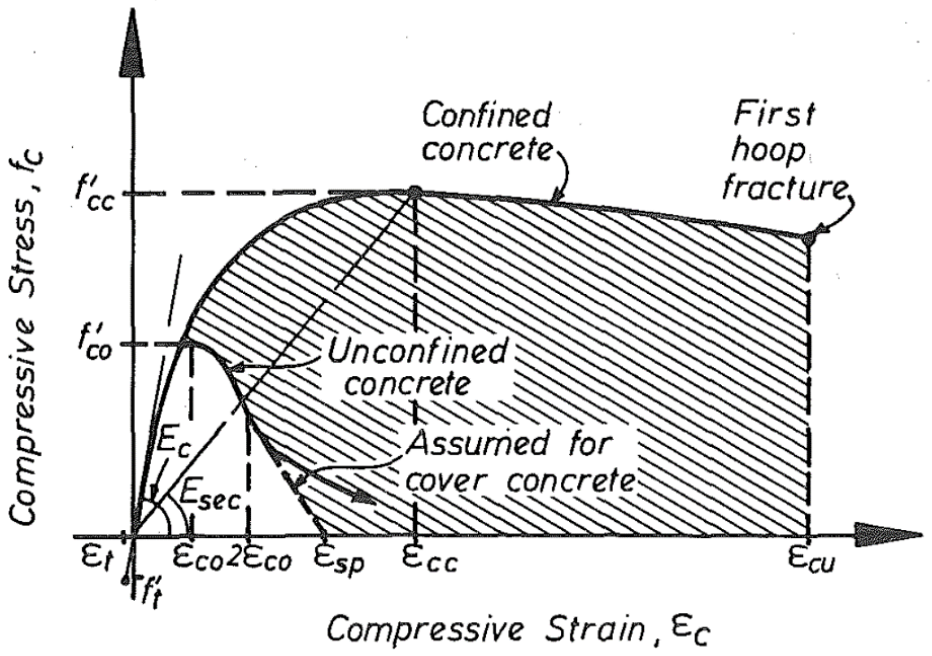



*Figure 2-1: Stress-strain model proposed for monotonic loading of confined and unconfined concrete. Mander et al. (1988b)*

The proposed stress-strain model in Figure 1 is based on the following equations:

$$f_c = \frac{f'_{cc} x r}{r - 1 + x^r} \qquad \textit{Equation 2-1}$$

$$x = \frac{\varepsilon_c}{\varepsilon_{cc}} \qquad \textit{Equation 2-2}$$

$$\varepsilon_{cc} = \varepsilon_{co}\left[1 + 5\left(\frac{f'_{cc}}{f'_{co}} - 1\right)\right] \qquad \textit{Equation 2-3}$$

where $f_c$ = longitudinal compressive concrete stress, $f'_{cc}$ = compressive strength of confined concrete, and $\varepsilon_c$ = longitudinal compressive concrete strain. Applying such stress-strain models is important for designing and predicting the performance of RC structures. This is especially important for structures with corrosion where mechanical properties change. The following

sections will look at the impact corrosion has on the stress-strain relationship at the material and member level, as well as the structural level.

## 2.2 Impacts of Corrosion on Material and Member Response

### *2.2.1 Almusallam, A. A. (2001)*

The decrease in the load-carrying capacity of corroded RC columns can be attributed to a combination of reduction in the bond between the reinforcing steel and concrete and/or mechanical changes in the steel (Almusallam, 2001). The scope of Almusallam's (2001) research was to "evaluate the relationship between the degree of corrosion of the steel bars in concrete on their mechanical properties" (p. 362).

In the experimental program conducted by Almusallam (2001), reinforcing steel bars, 6 and 12 mm in diameter were embedded in concrete specimens prepared in accordance with ASTM C150. The reinforcing bars were then corroded using an accelerated process that is illustrated in Figure 2-2.

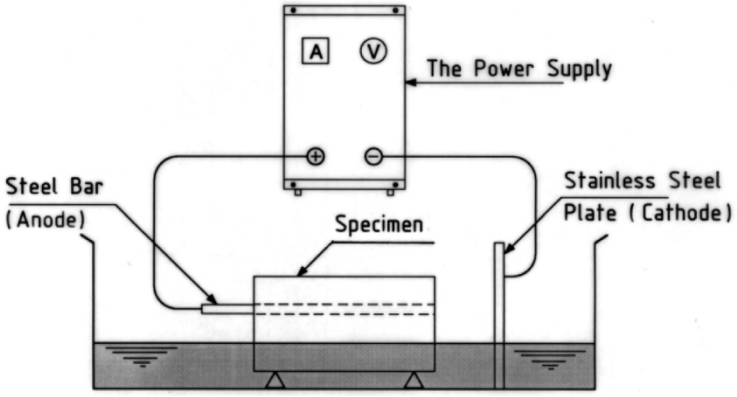



*Figure 2-2: Schematic representation of the accelerated corrosion test setup. Almusallam (2001)*

As Figure 2-2 shows, the concrete specimen was partially submerged in a 5% sodium chloride solution. The reinforcing steel embedded in the concrete was never submerged. This was done to ensure that the corrosion product formed was not washed away. A DC power supply was used, and the reinforcing steel became the anode, and a stainless-steel plate submerged in the solution became the cathode. To obtain the desired levels of corrosion, prior to beginning experimentation, a calibration curve was established that related to the duration of imposed current and the corresponding degree of reinforcement corrosion.

After reaching the desired levels of corrosion, the reinforcing bars were then removed from the concrete and cleaned following the steps provided in ASTM G1. To evaluate the mechanical

properties of the steel bars, Almusallam (2001) utilized an Instron Universal Testing Machine with a purpose-built extensometer to measure bar elongation. The bars were then loaded in tension and tested until failure. Almusallam (2001) found that as the percentage of corrosion increased, there was a reduction in strength as well as elongation. This can be seen in Figure 2-3, which shows the stress-strain relationship of the 6 mm corroded bars at varying levels of corrosion.

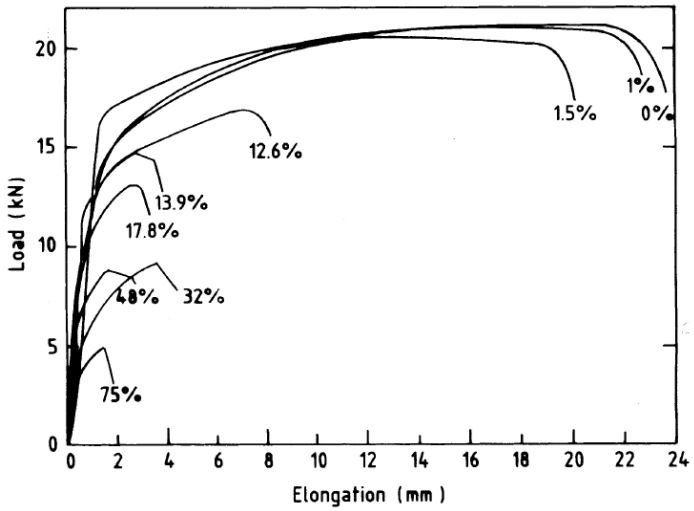



*Figure 2-3: Load-elongation curves for 6-mm diameter steel bars with varying degrees of corrosion. Almusallam (2001)*

As Figure 2-3 shows, with increasing levels of corrosion, the bars failed with a decreasing amount of yield-strain, indicating that the corrosion increased the brittleness of the bars. According to Almusallam (2001), bars with 12.6% or more corrosion, exhibited brittle failure. Furthermore, as corrosion levels surpassed 40%, small areas of the bars exhibited increased thinning, indicating a tendency for notch formation and localized corrosion (Almusallam, 2001). Examples can be seen in Figure 2-4, which shows bars with 75% corrosion. These defects typically occur at "high levels of chlorides or [in] situations where concrete is cracked or honey-combed at specific locations providing ingress to chloride ions and oxygen" (Almusallam, 2001, p. 336). Such notches and areas of localized corrosion have smaller cross-section areas, which leads to increased stress concentrations in these areas and more brittle failures.

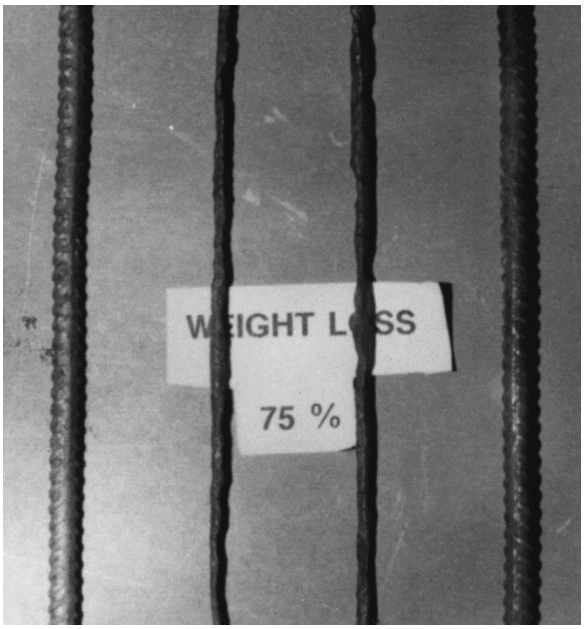



*Figure 2-4: Effect of 75% corrosion on rebar configuration. Almusallam (2001)*

### *2.2.2 Kashani et al. (2012)*

This paper investigated the nonlinear stress-strain behavior of corroded reinforcing bars. To simulate the corrosion process, Kashani et al. (2012) constructed a total of six reinforced concrete specimens. Two of the specimens contained 8 mm and 12 mm diameter reinforcing bars that would be tested in tension, while the other four specimens contained 12 mm diameter reinforcing bars that would be used in buckling tests. The specimens were then corroded using an accelerated corrosion procedure similar to that utilized by Almusallam (2001).

To estimate the duration of the corrosion process, Faraday's 2nd Law of Electrolysis was used. After reaching the desired corrosion times, the corroded reinforcing bars were carefully removed from the concrete, cleaned, and measured for mass loss. The bar specimens are summarized in Table 2-1 below.

*Table 2-1: Summary of corrosion duration of test specimens. Kashani et al. (2012)*

| Specimen no. | Corrosion current density ($mA/cm^2$) | Corrosion duration (days) | Estimated mass loss (%) | Measured mass loss (%) |
|---|---|---|---|---|
| *Tension specimens* | | | | |
| T1 | 2.4 | 5 | 15 | 6.5 |
| T2 | 2.4 | 14 | 25 | 10.5 |
| *Compression specimens* | | | | |
| C1 | 1.1 | 28 | 30 | 19.1 |
| C2 | 1.1 | 35 | 38 | 26.5 |
| C3 | 1.1 | 43 | 50 | 32.0 |
| C4 | 1.1 | 35 | 38 | 25.0 |

As is shown in Table 2-1, the estimated mass loss values that were calculated using Faraday's Law are much higher than the actual measured values. Kashani et al. (2012) attributed this difference to the higher current density levels as well as corrosion durations that were used, both of which "have an influence on the ability of Faraday's law to predict the real mass loss" (p. 419).

The 8 mm and 12 mm bars were tested in tension using a universal testing machine. The mean stress-strain responses of the bars were then plotted and compared to uncorroded bars. Figure 2-5 shows the mean-stress curves for the 8 mm bars. Mean stress (MPa) is the calculated stress that is based on the average reduced cross-sectional area, and mean strain is the average strain over the total length of the bar (Kashani et al., 2012).

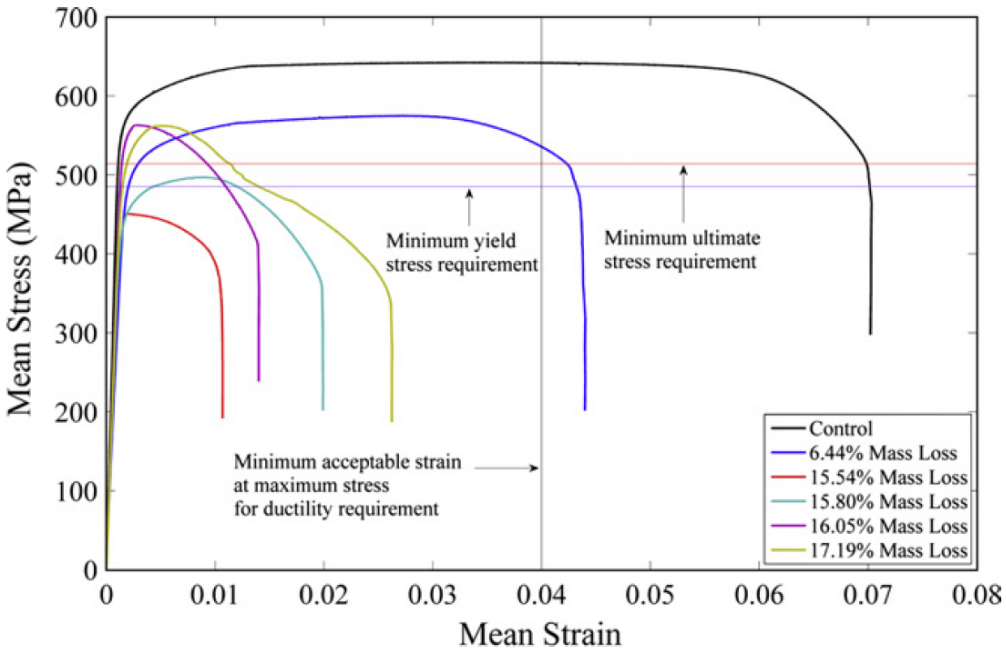



*Figure 2-5: Mean stress-strain curves of tension tests for the 8 mm diameter. Kashani et al. (2012)*

The results from Kashani et al. (2012) show that even small amounts of corrosion will greatly reduce the mean strain value at failure. For example, a bar with 6.44% mass loss will have approximately a 35% reduction in the mean strain at failure, while a bar with 15% mass loss will have a reduction of approximately 78% (Kashani et al., 2012). The authors noted the results contrasted with the results reported by several other researchers, who found that corrosion will not have such a significant effect on the stress-strain curves of bars in tension. However, Kashani et al. (2012) attributes these different findings of other researchers to the random nature of corrosion as well as different steel grades that may have been used. They concluded that uniform corrosion will not have a significant effect on the mean stress-strain response because mean stress is calculated based on the mean reduced diameter of the bar (Kashani et al., 2012). Rather, the change in mean stress-strain response is caused by the non-uniform distribution of pits and crevices along the bar, which results in non-uniform stiffness that affects the yield, ultimate strength, and ductility of the bar (Kashani et al., 2012). This can be seen in Figure 2-6 where the normalized ratios of yield stress ($f_y$) and ultimate stress ($f_u$) are plotted relative to mass loss percentage. A linear trend was fitted to the test data and compared to models proposed by Du et al. (2005).

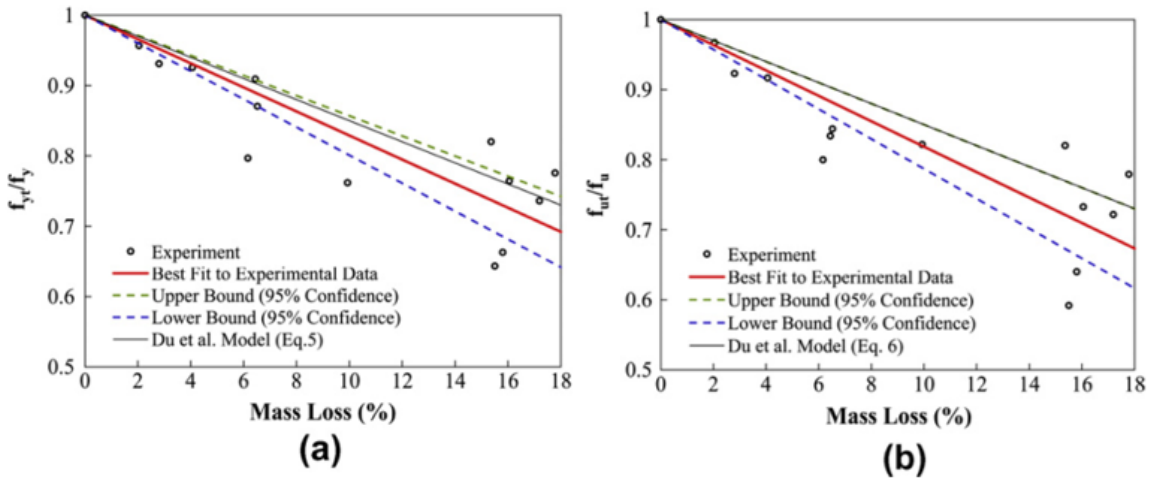



*Figure 2-6: Trend lines of test experiments of all groups of bars: (a) yield stress; (b) ultimate stress. Kashani et al. (2012)*

In addition to the tension tests, a series of compression tests were performed on corroded bars to investigate the effect that corrosion has on buckling. It was found that the inelastic buckling mechanism was affected by non-uniform pitting corrosion and that the buckling mechanism of corroded bars is a function of mass loss and distribution of pits along the bar (Kashani et al., 2012).

## 2.3 Impacts of Corrosion on the Structural Level

### *2.3.1 Meda et al. (2014)*

Meda et al. (2014) evaluated the structural behavior of corroded RC columns subjected to cyclic loads. The research was conducted in two parts. The first part was dedicated to the calibration and optimization of the corrosion process, while the second part focused on corrosion at the structural level.

To calibrate and optimize the corrosion process, a series of nine bars were subjected to various levels of corrosion and tested in tension. The bars were corroded using a similar electrolytic corrosion process utilized by Almusallam (2001) and Kashani et al. (2012), and the time to corrode was calculated using Faraday's Law. A summary of the nine tested bars with their desired and actual corrosion levels can be seen in Table 2-2 below.

*Table 2-2: Bar specimens. Meda et al. (2014)*

| **Bar name** | **NC-1** | **NC-2** | **NC-3** | **A1** | **A2** | **A3** | **C1** | **C2** | **C3** |
|---|---|---|---|---|---|---|---|---|---|
| Foreseen corrosion [%] | 0 | 0 | 0 | 10 | 10 | 10 | 20 | 20 | 20 |
| Actual corrosion [%] | – | – | – | 11.9 | 12.9 | 12.6 | 21.2 | 21.4 | 22.1 |

The corroded bars were pulled in tension until failure. The results are summarized in Figure 2-7 which shows the force-strain relationship of the bars. There is a clear reduction in the load and strain at failure for the higher levels of corrosion. The results consistently showed a reduction in both yielding and ultimate force (Meda et al. 2014). Following these nine tests, a series of embedded bars were also corroded and tested, producing similar results.

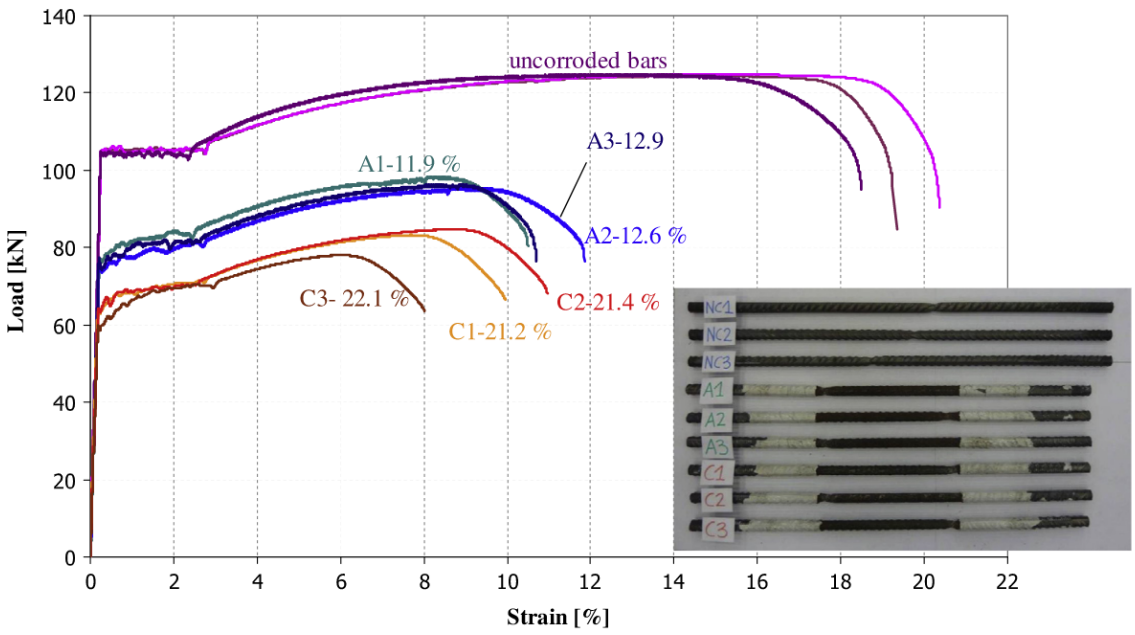



*Figure 2-7: Load-strain relationship and bars after the test. Meda et al. (2014)*

For the structural component of the research, two identical columns were constructed. One column was subjected to corrosion of the longitudinal reinforcement steel, while the other was kept uncorroded for reference. The corroded column was corroded to a theoretically calculated level of 20% mass loss, using a method similar to that of the material tests. The authors noted at the end of the corrosion process there were four distinct vertical cracks spanning the length of the column as a result of the production of rust (Meda et al., 2014).

The two columns were both subjected to identical cyclic tests and the results were compared. The uncorroded column reached a maximum positive load of 63 kN and a maximum negative load of 61 kN with drifts around ±2.0%. The test was stopped around 40 kN at 5% drift, due to cover spalling, concrete crushing in the plastic hinge, and buckling of one of the reinforcing bars. In contrast, the corroded column reached a maximum positive and negative load of 44 kN and 46 kN respectively. The corresponding drifts were 1.0% and 1.25%. The final cycle had a load of 36 kN and a drift of 2.5%.

The load-drift relationship diagrams of both columns can be seen in Figure 2-8, with significant values of load and displacement presented in Table 2-3. Compared to the uncorroded column the corroded column showed a decrease in maximum strength of about 30% and up to a 50% decrease in deformation (Meda et al., 2014). Meda et al. (2014) also noted a sharp reduction in stiffness of the corroded column during the last two cycles. Additionally, the non-dimensional

energy dissipation for each cycle was analyzed for both columns. Meda et al. (2014) found that the non-dimensional energy dissipation by the corroded column was always higher than the uncorroded column, illustrating pre-existing damage as a result of corrosion.

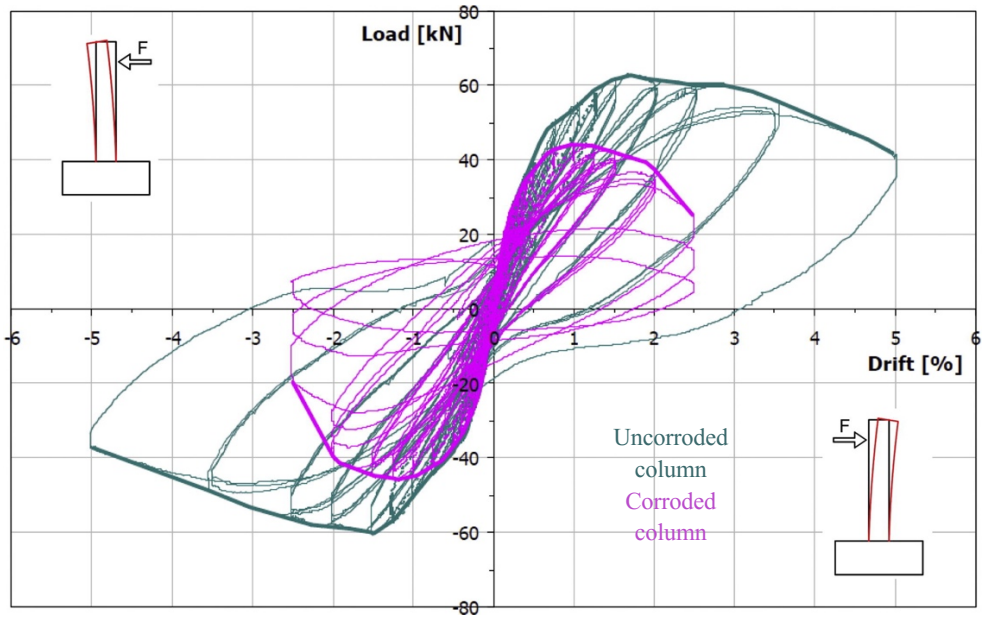



*Figure 2-8: Cyclic behaviour: horizontal load versus horizontal displacement. Meda et al. (2014)*

*Table 2-3: Cyclic test results. Meda et al. (2014)*

| Empty Cell | $F_{max}^{+}$ (kN) | $(F_{CC}/F_{UC})^{+}$ | $F_{max}^{-}$ (kN) | $(F_{CC}/F_{UC})^{-}$ | $\delta_{max}^{+}$ (%) | $\delta_{max}^{-}$ (%) | $\delta_{u}^{+}$ (%) | $\delta_{u}^{-}$(%) |
|---|---|---|---|---|---|---|---|---|
| UC | 63 | 1.00 | 60 | 1.00 | 2.00 | 1.50 | 5.00 | 5.00 |
| CC | 46 | 0.73 | 48 | 0.8 | 1.00 | 1.25 | 2.50 | 2.50 |

UC Uncorroded column.
CC Corroded column.

### *2.3.2 Andisheh et al. (2021)*

The experimental program conducted by Andisheh et al. (2021) proposes an analytical model to predict the stress-strain relationship of RC columns with reinforcement corrosion. The model uses four key parameters to predict the stress-strain graph: maximum compressive stress ($f'_{cc}$), strain at maximum compressive stress ($\varepsilon_{cc}$), modulus of elasticity of concrete ($E_c$), and the ultimate compressive strain of concrete ($\varepsilon_{cu}$). To calibrate and validate the model, a series of 12 circular RC columns were constructed and tested under quasi-static monotonic compressive loading. Ten of the columns featured different levels of corrosion, while the other two were unreinforced plain columns. The reinforced columns were identical in size and used the same longitudinal steel reinforcement and spiral confinement type. What varied between the columns was the different levels of confinement. The columns were grouped into three categories: comparatively low volumetric ratios (LCON), medium volumetric ratios (MCON), and high volumetric ratios (HCON). The columns were further categorized into four different corrosion groups: noncorroded (NC), low corrosion (LC), high corrosion (HC), and artificial mechanical pitting corrosion (Pit). A summary of the columns with the type of corrosion and corrosion level can be seen below in Table 2-4.

*Table 2-4: Experimental corrosion test results and theoretical prediction results. Andisheh et al. (2021)*

| Cross-section configuration type | Name | Corrosion rate ($\mu A/cm^2$) | Average corrosion experimentally measured (%) | Average corrosion theoretically calculated (%) | Exposure time (days) |
|---|---|---|---|---|---|
| Low confined | NC-LCON | 0 | 0 | 0 | 0 |
| | LC-LCON | 620 | 7.1 | 6.5 | 10 |
| | HC-LCON | 650 | 18.6 | 20.2 | 31 |
| | Pit-LCON | — | 4-mm pit depth | — | — |
| Medium confined | NC-MCON | 0 | 0 | 0 | 0 |
| | LC-MCON | 625 | 9.8 | 6.5 | 10 |
| | HC-MCON | 900 | 31.6 | 26.5 | 30 |
| High confined | NC-HCON | 0 | 0 | 0 | 0 |
| | LC-HCON | 580 | 11.3 | 6.3 | 10 |
| | HC-HCON | 620 | 19.3 | 20 | 30 |

The columns were tested until failure. Andisheh et al. (2021) observed two main types of failure that depended on the amount of confining reinforcement, not the degree of corrosion. For columns with low confinement, failure mainly occurred in the form of diagonal failure planes which led to the development of shear stresses (Andisheh et al., 2021). In addition, the buckling of the longitudinal bars was observed in the diagonal failure planes. For columns with high levels

of confinement, failure had two main characteristics: "(1) the location of failure was random and (2) the shape of failure was transverse expansion over a certain length, and the buckling of the longitudinal bars took place at certain heights" (Andisheh et al., 2021, p. 8).

While the failure mode was not affected by corrosion, the performance of the columns depended on the levels of corrosion. The stress-strain relationships of the columns can be seen in Figure 2-9. From the results, it can be seen that low levels of corrosion only decrease the ultimate strain of the confined concrete. The authors discussed that for low amounts of corrosion there was greater variability and relative uncertainty. This was attributed to challenges in quantifying the degree of corrosion at low levels. For columns with higher levels of corrosion, there was a clear decrease in both the ultimate compressive strength and ultimate strain of the confined concrete (Andisheh et al., 2021).

Andisheh et al. (2021) concluded that the corrosion of transverse reinforcement most significantly affects the stress-strain response of corroded RC columns and that high levels of corrosion will drop the post-peak compression strength and the slope of the stress-strain curve. For a mass loss of 19%, reduction values of 20%, 30%, and 76% were observed for ultimate compressive strength, strain at the ultimate compressive strength, and the ultimate strain of the RC column respectively (Andisheh et al., 2021).

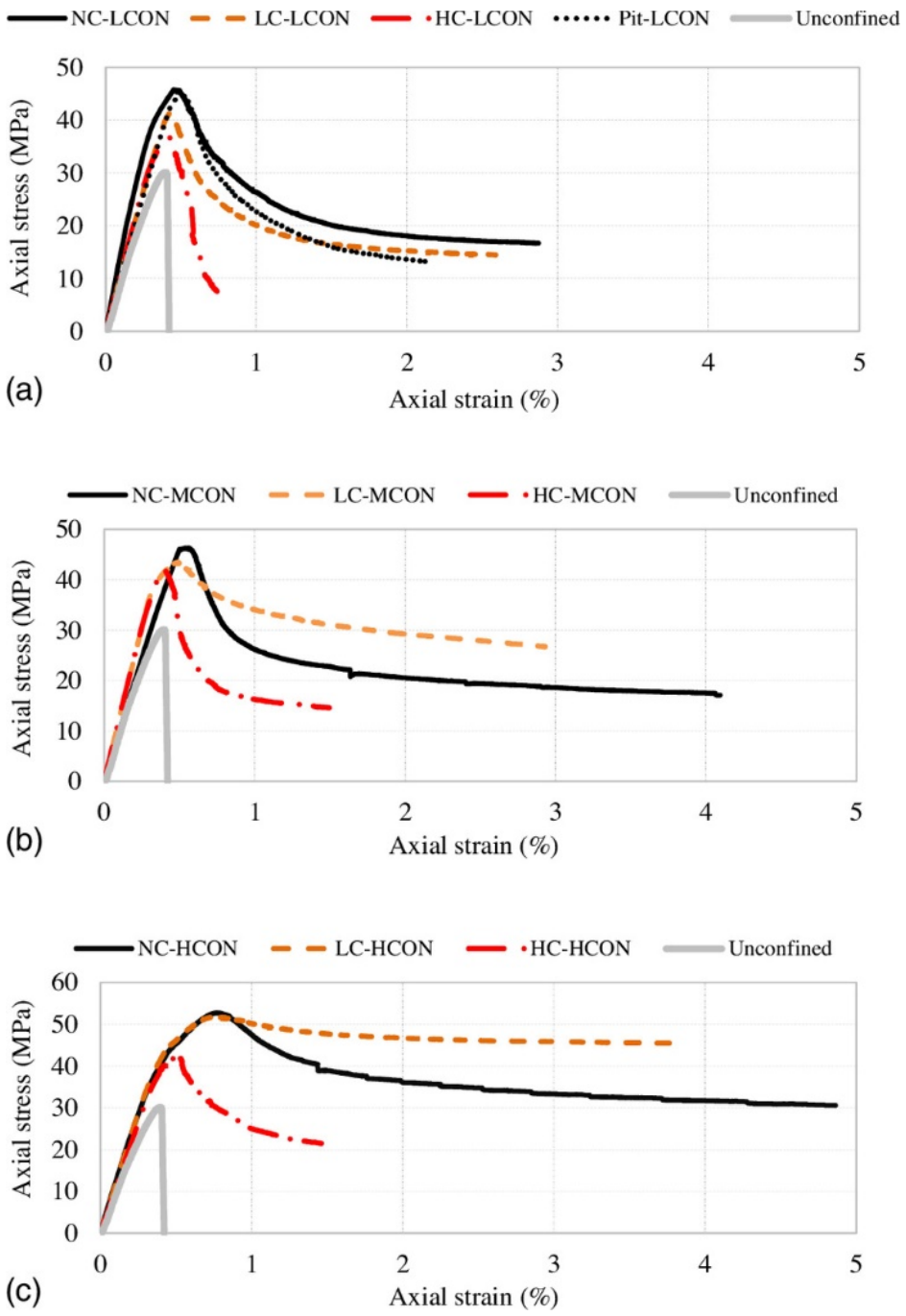



*Figure 2-9: Stress-strain relationship of concrete with varying degrees of corrosion and confinement arrangements. Andisheh et al. (2021)*

## 2.4 Discussion and Knowledge Gaps

Many studies have shown that corrosion will have an impact on the mechanical properties of steel, leading to a reduction in strength and elongation. Furthermore, the corrosion of reinforcing steel has been shown to have a significant effect on the global response of RC structures. Therefore, it is critical to develop a model that will be able to predict the future performance of corroded structures. This is especially important for corroded structures in seismic regions that are subjected to large loads and stresses during a seismic event.

It is clear that corrosion is a key issue in the reliability of RC structures. The papers reviewed in this literature review showed that the corrosion of the reinforcing steel has a significant impact on the stress-strain response of RC columns. Along with the authors presented in this literature review, other authors such as Rajput & Sharma (2018), Vu et al. (2017), (Zhang et al., 2022), and (Di Carlo et al., 2017), found very similar results. Additionally, it was shown that corrosion affects the strength, stiffness, and deformability of RC columns. The effect that corrosion has on the global response of RC columns will be further evaluated during the time of this research project. To accomplish this, a series of four large-scale RC columns with varying levels of corrosion will be tested and analyzed. The resulting data from the tests will then be compared to previous tests performed on uncorroded columns and will be used to further assess the impact that corrosion has on the performance limit states of RC columns. In addition, the behavior of corroded reinforcing steel due to buckling and subsequent fracture will be further examined. These values will be obtained using the Buckled Bar Tension (BBT) test developed by Barcley and Kowalsky (2019).

# CHAPTER 3: STRUCTURAL MEMBER CHARACTERIZATION

## 3.1 Test Specimens and Construction

### *3.1.1 Column Test Specimens*

The four columns in this experimental program were designed to represent scaled models of bridge columns. Each single degree of freedom specimen consisted of a footing, column, and cap beam. Figure 3-1 shows the dimensions of the four columns. Each column had a cantilever height of 8 feet and an 18-inch diameter, giving them a height-to-diameter ratio of 5.33. The columns were reinforced with 10 #6 longitudinal bars (ASTM A706 Grade 60 steel, ρl = 1.7%), and #3 transverse spiral (ASTM A706 Grade 60 steel, ρs = 1.3%) spaced at 2". The lower half of the columns lacked the concrete cover to allow for the instrumentation of the reinforcing steel, while the upper half had a ½" concrete cover outside the transverse steel. The footing and cap beam were designed as capacity protected members.

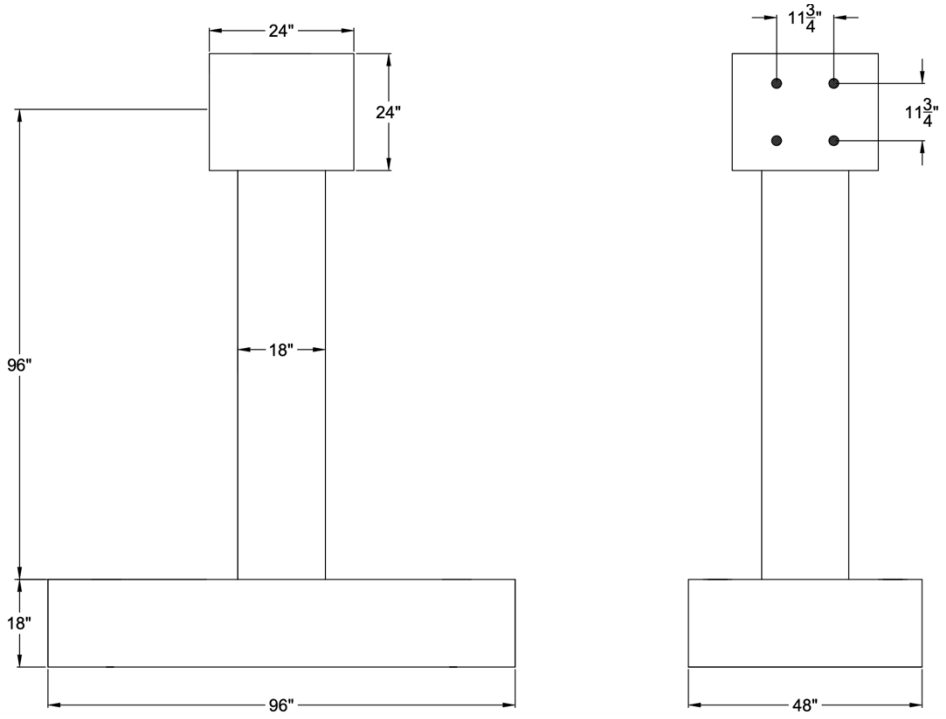



*Figure 3-1: Test specimen geometry*

The footings consisted of Grade 60 steel, and the reinforcement is shown in Figure 3-2. The reinforcement details are shown in Figure 3-3.

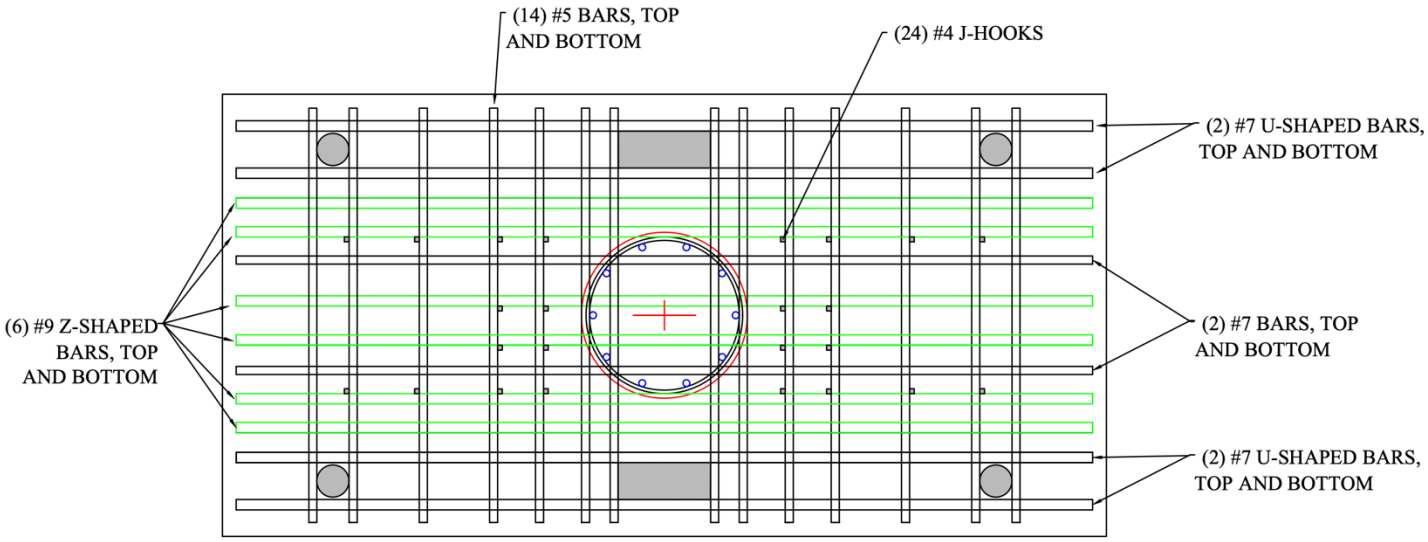



*Figure 3-2: Footing reinforcement plan*

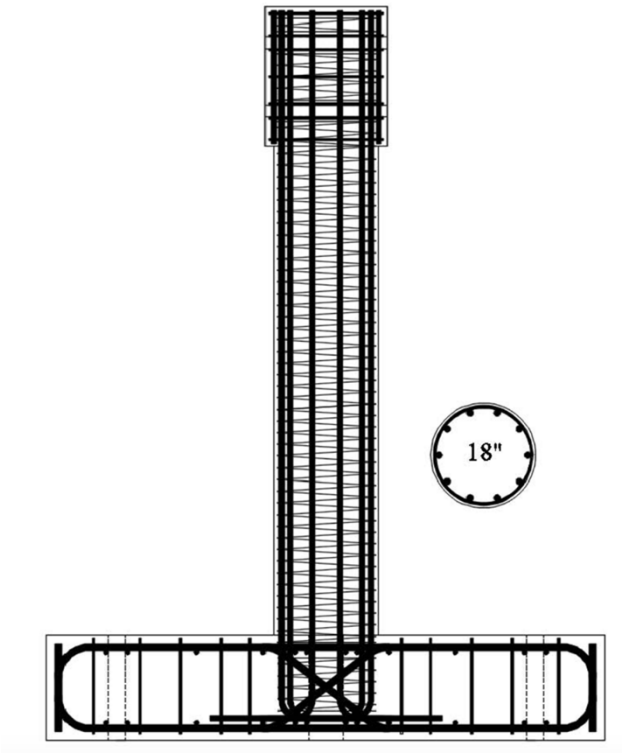



*Figure 3-3: Reinforcement details*

### *3.1.2 Accelerated Corrosion*

To replicate real-world corrosion, the reinforcing steel was corroded using an accelerated electrolytic process. In order for accelerated corrosion to occur, there are four required components: an anode, a cathode, an electrolytic connection, and an electrical path (Calderon, 2022). As depicted in Figure 3-4 below, the reinforcing steel, functioning as the anode, was immersed in a sodium chloride solution serving as the electrolytic connection. Surrounding the reinforcing steel was a stainless-steel mesh which acted as the cathode. An electrical current was applied to the system using an external power supply.

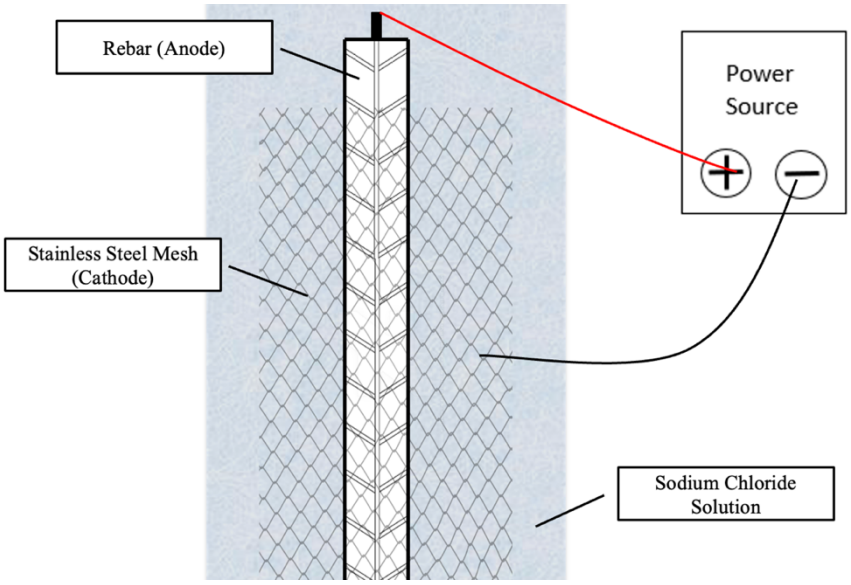



*Figure 3-4: Accelerated corrosion process*

Faraday's 2nd Law of Electrolysis was utilized to estimate the required time to reach a desired level of corrosion. This equation is shown in Equation 3-1.

$$t = \frac{m_{loss} * n * F}{I * A_m} \qquad \textit{Equation 3-1}$$

Where:

$t =$ time (seconds)

$m_{loss} =$ mass loss (grams)

$n =$ charge number

$F =$ Faraday constant $(\frac{1}{mol})$

$I = \text{Current (amp)}$

$A_m = \text{Atomic mass } (\frac{\text{grams}}{\text{mol}})$

The corrosion setups for the material tests and large-scale tests were nearly identical. Large plastic bins contained the sodium chloride solution. For the sodium chloride solution, 17.5 grams of sodium chloride were added for every liter of water. For the material tests, steel specimens were cut to the desired length, and the ends were protected before being fully submerged in the bins. It was necessary to protect the ends of the bars that would function as grips during the material tests. To protect the ends, heavy duty tape was wrapped multiple times around the specimens. For the large-scale tests, holes were cut in the bins and the portion of the longitudinal steel that would be in the plastic hinge of the column was incased within the bins. Both corrosion setups can be seen in Figure 3-5.



(a)



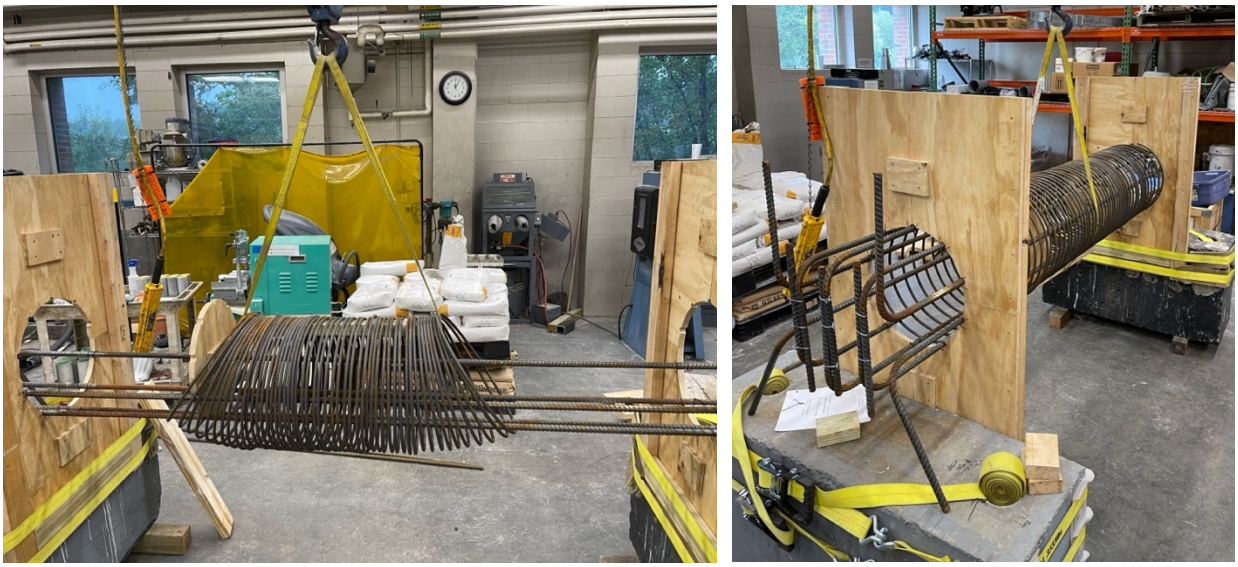
(b)

*Figure 3-5: Corrosion setup: (a) material tests; (b) large-scale tests*

After reaching the corrosion time calculated using Faraday's 2nd Law of Electrolysis, the steel specimens were removed from the setup and cleaned. The specimens were washed and cleaned with a bristle brush to remove corrosion residue. Measurements of the specimen's cross section were then taken to ensure the desired level of corrosion was reached. Throughout this report, corrosion level will be denoted as a percentage (i.e. 0% to 50% corrosion). The corrosion percentage refers to percentage of mass loss due to corrosion in the plastic hinge region of the columns.

### *3.1.2 Column Construction*

To construct the column cages, the corroded longitudinal bars were placed through a continuous spiral of transverse steel and attached in a circular configuration to two plywood forms. The transverse spirals where then tied to the longitudinal bars at a spacing of 2” center to center. To insure proper spacing, strips of wood with slots spaced at 2” center to center, were fabricated and placed on the column cage to hold the spiral during the tying process. Prior to construction, the ends of the longitudinal bars were bent to 90° hooks to allow for adequate development length. Photos of the column cage construction process can be seen in Figure 3-6.



(a) (b)

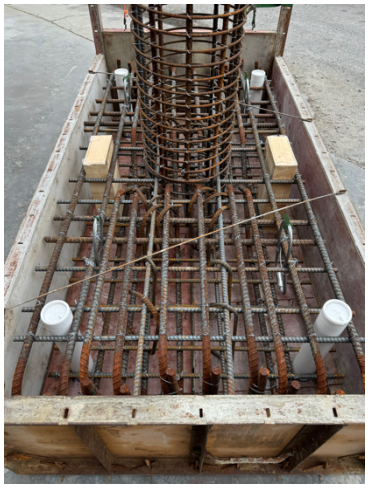
(c) (d)

*Figure 3-6: Column cage construction: (a) longitudinal bars inside of spiral; (b) longitudinal bars attached in circular configuration to plywood forms; (c) spiral tying; (d) spiral tying close-up*

For the construction of the footing, pre-engineered modular formworks were used. In the locations where the footing would be attached to the strong floor, 3” PVC pipes were added to the formwork. In addition, two wood block outs were attached to the formwork where the axial load bars would be placed. The Z-shaped and U-shaped bars were tied and placed in the footing. After half the footing steel was placed in the formwork, the completed column cage was added, and the remaining footing steel was added and tied to the column cage. Photos of the footing construction can be seen in Figure 3-7. Ratchet straps were attached to the column cage to ensure it was level and the footing was then cast on a flat casting slab. Photos of the footing casting can be seen in Figure 3-8.



(a)



(b)



(c)

*Figure 3-7: Footing construction: (a) footing formwork with block outs; (b) completed footing top view; (c) completed footing side view*



(a) (b)

*Figure 3-8: Footing casting: (a) pouring of concrete; (b) concrete setting*

To allow for the instrumentation of the reinforcing steel in the lower half of the column, foam strips wrapped in clear tape were cut and inserted between the transverse reinforcement. The purpose of the strips was to block out the concrete cover in the lower half of the column. The strips were then wrapped in duct tape to hold them in place during casting. An 18” round concrete form was then placed over the column cage. A wooden frame was then built around the column to hold the form work for the cap beam. PVP pipes were attached to the cap beam formwork where the cap beam would be attached to the actuator. To cast the column and cap beam, concrete was poured into the cap beam formwork. Photos of the construction and casting of the column and cap beam can be seen in Figure 3-9. After the concrete had cured, all the form work and block outs were removed. Excess concrete around the longitudinal and transverse steel in the lower half of the column was removed using an air needle scaler.



(a)



(b)



(c)



(d)



(e) (f)

*Figure 3-9: Column and cap beam construction and casting: (a) concrete cover block-out for test instrumentation; (b) placing form tube on column cage; (c) capbeam frame; (d) casting column and capbeam; (e) cleaning column; (f) final column*

## 3.2 Experimental Test Setup

This section outlines the experimental setup and instrumentation for the large-scale quasi-static column tests. Furthermore, the loading protocol is summarized.

### *3.2.1 Test Setup*

During the test, lateral load was applied to the column using a 220-kip hydraulic actuator connected to a strong wall. Axial load was applied to the top of the column's cap beam via two hydraulic jacks attached to a spreader beam. The two jacks were connected to a third jack in a universal testing machine, creating a closed-loop system and ensuring the axial load remained constant during the test. The footing of the column was placed on top of fiber board to level surface contact and prevent slipping. In addition, the footing was post-tensioned to the strong floor using four 1-3/8" bars stressed to approximately 100 kips per bar. To ensure the footing did not slip or rotate during the test, two string potentiometers were attached to the footing along with an inclinometer. To measure the global displacement of the column, two string potentiometers were attached to the cap beam of the column. A schematic and photo of the actual setup can be seen in Figure 3-11 and Figure 3-12, respectively. Throughout this report, the side of the column nearest to the actuator will be denoted as the South side, while the other side will be referred to as the North Side. This can be seen in Figure 3-10. All the columns were subjected to an axial load of $P$ = 144 $kips$ ($P/(f_c^{'}A_g)$ = 10%).




*Figure 3-10: Loading sign convention and extreme longitudinal bar labeling*

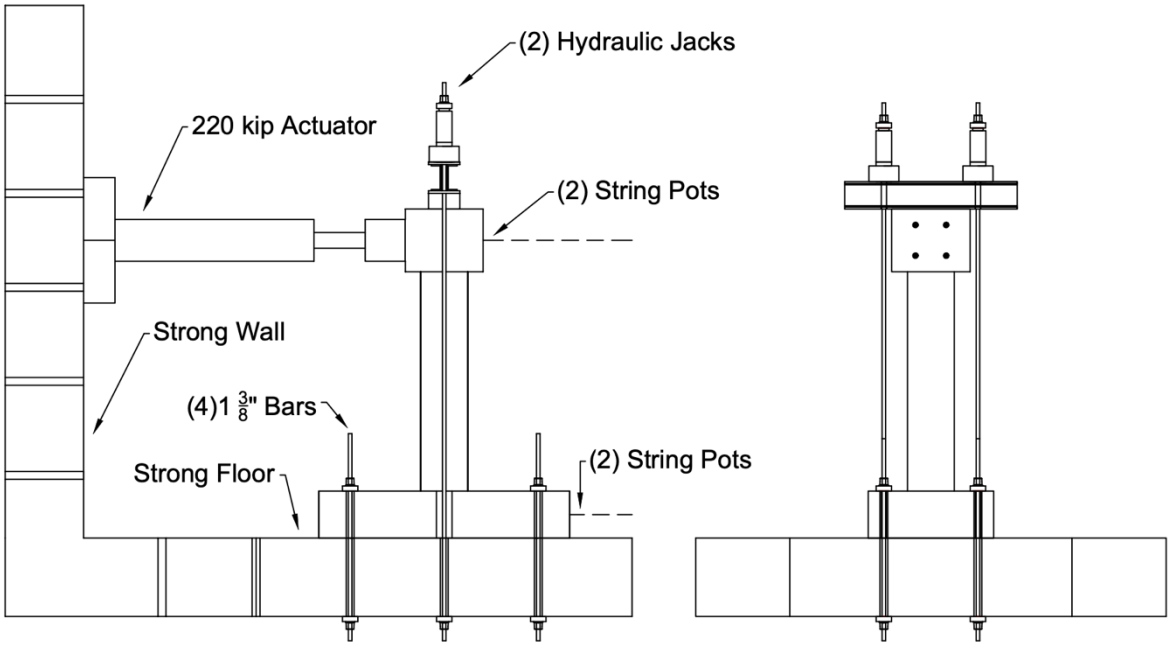



*Figure 3-11: Test setup: (a) side view; (b) front view*



*Figure 3-12: Actual test setup*

### *3.2.2 Instrumentation*

To measure axial and bending strain of the reinforcing steel, an optical 3D measurement system was utilized. The system used was Optotrak Certus HD, a camera system capable of capturing three-dimensional spatial coordinate history of LED markers. A total of 112 markers were placed on the extreme longitudinal bars as well as the first four layers of spiral in the plastic hinge zone. Figure 3-13 shows the Optotrak markers placed on the longitudinal and transverse reinforcement. During the test, the 3D position of each marker was recorded. The measurements were then used to find change in length between markers, giving strains along the longitudinal and transverse steel.



*Figure 3-13: Optotrak markers*

### *3.2.3 Load Protocol*

The column was subjected to a three cycle, unidirectional, quasi-static load. The displacements of the load history were based off a previously tested column with nominally identical detailing (Goodnight et. al 2015, Test 19). For the results from the previously tested

column, see Appendix D. The initial loading of the column consisted of single positive and negative cycles at a quarter first yield force, half first yield force, three quarters first yield force, and first yield force. The cycles following first yield, consisted of three cycles at increments of displacement ductility. The values for displacement ductility are shown in Table 3-1.

*Table 3-1: Displacement ductility*

| Ductility | Displacement (inches) |
|---|---|
| $\mu_1$ | 1.14 |
| $\mu_{1.5}$ | 1.71 |
| $\mu_2$ | 2.29 |
| $\mu_3$ | 3.43 |
| $\mu_4$ | 4.57 |
| $\mu_5$ | 5.71 |
| $\mu_6$ | 6.86 |
| $\mu_7$ | 8.00 |

# CHAPTER 4: SUMMARY OF COLUMN TESTS

## 4.1 Column Test 1 Summary

Column Test 1 was conducted at the Constructed Facilities Laboratory on January 31st, 2024. The column featured 10% corrosion (defined by mass loss) in the plastic hinge. Table 4-1 summarizes column parameters and damage observations.

*Table 4-1: Column test 1 parameters and results summary*

**Load History**: Symmetric Three Cycle Quasi Static

**Column Parameters:**

| | |
|---|---|
| Corrosion Level: | 10% |
| Concrete Compressive Strength: | $f$c' = 6662 psi |
| Corroded Longitudinal Bars Strength: | fy = 54.8 ksi |
| Axial Load: | $P$ = 144 kips ($P$/($f$c'$A$g) = 10%) |
| Column Length and Aspect Ratio: | 8ft (L/D = 5.33) |
| Equivalent Yield Displacement: | $\Delta_y$ = 1.15" |
| Maximum Lateral Force: | 28.12 kips |
| Failure Mode: | Fracture of buckled longitudinal steel |

**Damage Observations:**

| | |
|---|---|
| First Cracking North: | $F_y$' = 0.81" |
| First Cracking South: | -$F_y$' = -0.93" |
| Concrete Crushing North: | $\mu_4^{+2}$ = 4.61" |
| Concrete Crushing South: | $\mu_4^{-1}$ = 4.61" |
| Longitudinal Bar Buckling North; N3: | $\mu_6^{+3}$ = 6.91" |
| Longitudinal Bar Buckling North; N2: | $\mu_7^{1}$ = 8.05" |
| Longitudinal Bar Buckling South; S3: | $\mu_5^{-2}$ = -5.75" |
| Longitudinal Bar Buckling South; S4: | $\mu_7^{-1}$ = 8.07" |
| Longitudinal Bar Fracture North; N2, N3: | $\mu_7^{-1}$ = 8.07" |
| Longitudinal Bar Fracture South; S3, S4: | $\mu_7^{+2}$ = -8.06" |

Material tests were performed on the reinforcing steel (uncorroded and corroded) and the concrete used in the column. Figure 4-1 shows the stress-strain responses of the uncorroded and

corroded steel specimens, and Table 4-2 summarizes the results. For the corroded specimen, bar N3 was extracted from the column after the test. Because the bar was removed from the plastic hinge after testing, the bar was already yielded, hence the roundhouse behavior seen in Figure 4-1. Compression tests were performed on concrete samples on the day of the test. The results are summarized in

Table 4-3.

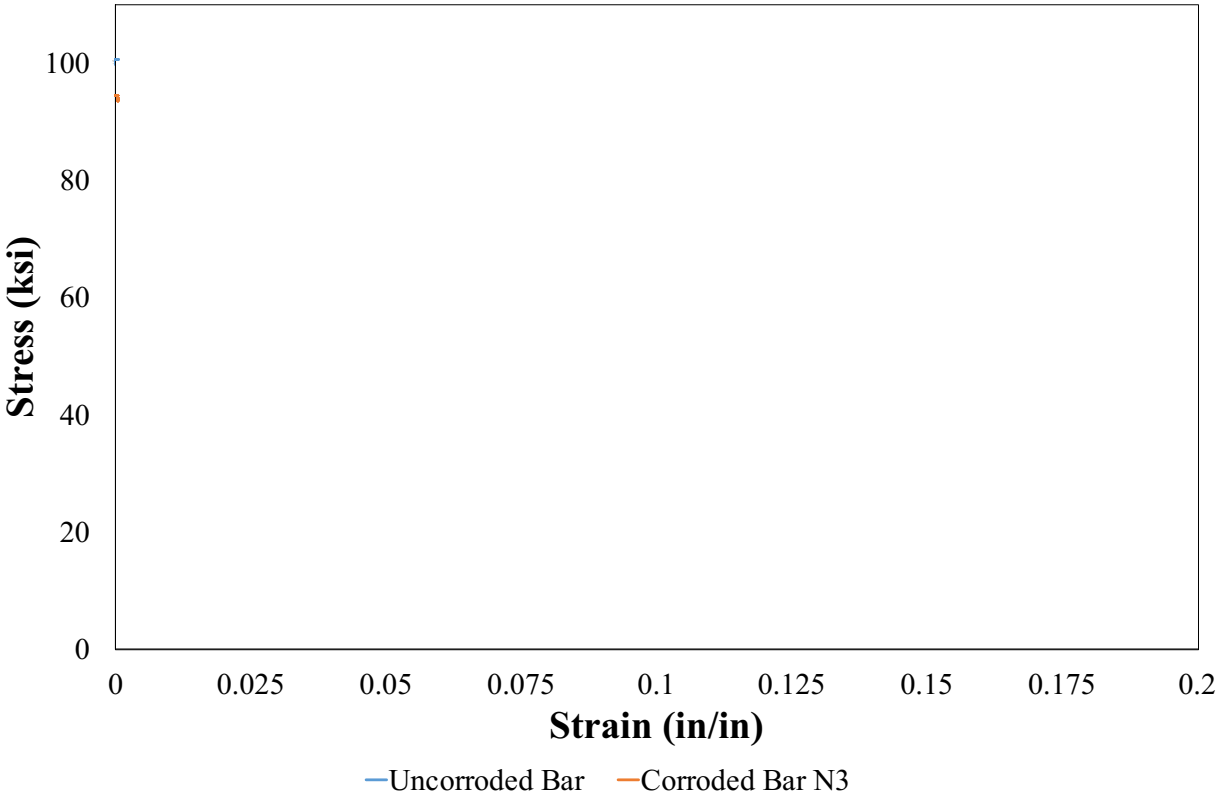



*Figure 4-1: Column test 1 stress-strain response material tests*

*Table 4-2: Column test 1 material tension test results*

| Steel | Yield Stress (ksi) | Yield Strain (%) | Maximum Stress (ksi) | Strain at Maximum Stress (%) |
|---|---|---|---|---|
| Uncorroded bar | 68.5 | 0.22 | 100.2 | 11.6 |
| Corroded bar N3 | 54.8 | 0.27 | 94.1 | 10.4 |

*Table 4-3: Column test 1 concrete compression strength results*

| Column Concrete | | Footing Concrete | |
|---|---|---|---|
| **Cylinder** | **Stress (psi)** | **Cylinder** | **Stress (psi)** |
| 1 | 6772 | 1 | 7382 |
| 2 | 6826 | 2 | 7164 |
| 3 | 6388 | 3 | 6959 |
| **Average** | 6662 | **Average** | 7168 |

During the test, between half cycles, cracks and damage states in the column were marked and recorded. Before the test, during post-tensioning, several superficial cracks were observed in the footing. These cracks were marked in blue to distinguish them from cracks developed during the test. Cracks on the South side of the column were marked in red, while cracks on the North side were marked in black. The test concluded during the second cycle of ductility seven, after four bars had fractured and the maximum force dropped over 50%. Figure 4-2 shows the force-displacement response, and Figure 4-3 shows the load history.

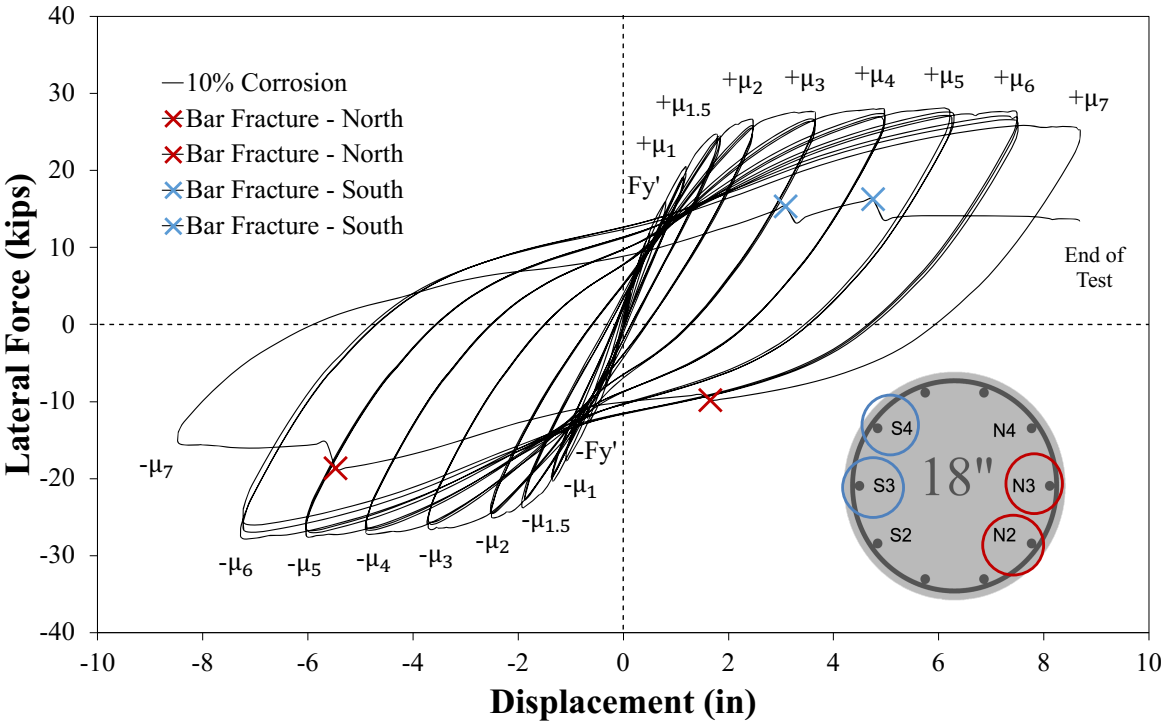



*Figure 4-2: Column test 1 force-displacement response*

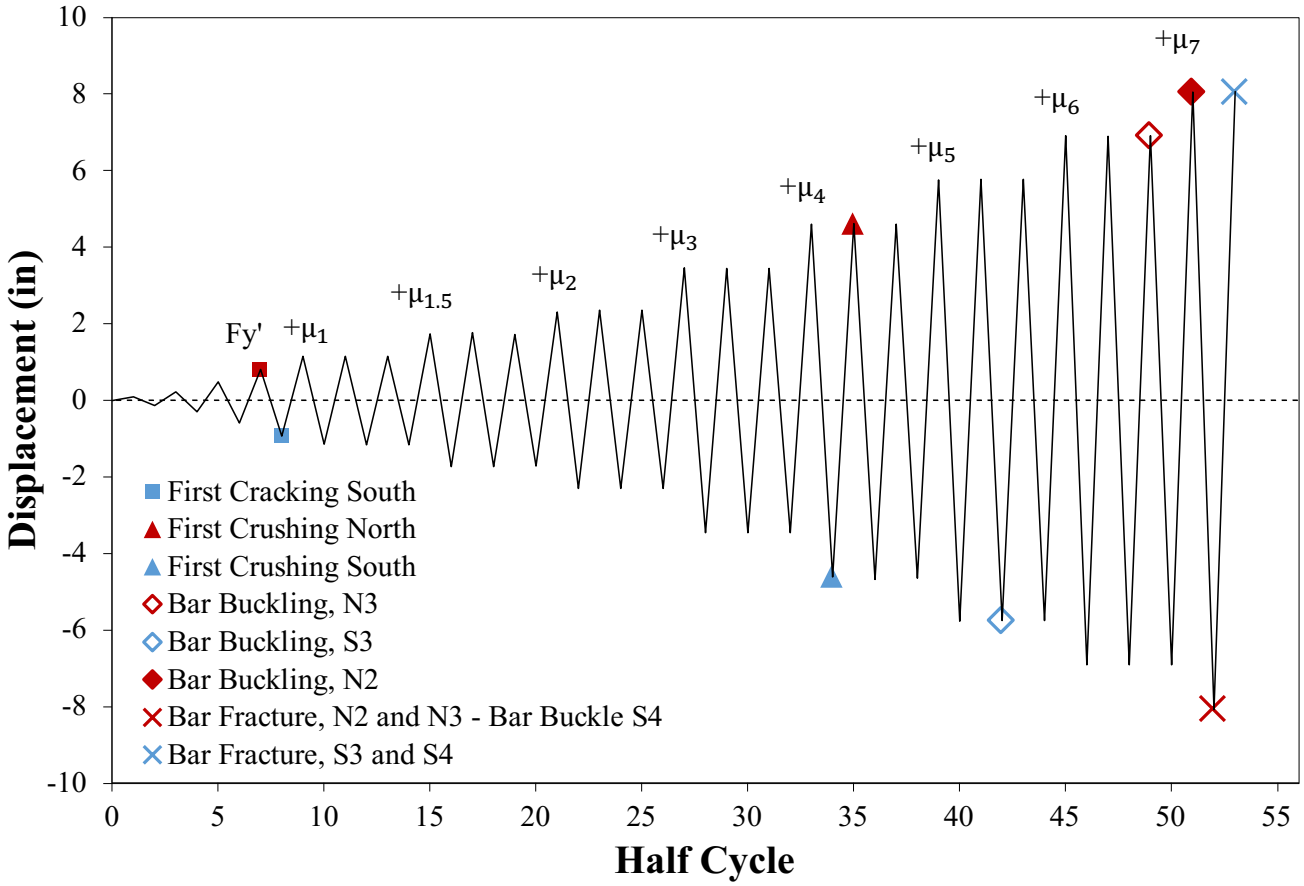



*Figure 4-3: Column test 1 load history*

### *4.1.1 Damage Progression*

Hairline cracks were observed on the South side of the column during first yield ($F_y' = 16.03\ kips$). The cracks were located near spirals approximately 12 inches above top of footing. Hairline cracks appeared on the North side during the next half cycle ($-F_y' = -17.78\ kips$). During ductility one, more hairline cracks developed in the plastic hinge as well as in the cover of the column. The crack distribution at the end of ductility one can be seen in Figure 4-4. During ductility 1.5 multiple flexural cracks were observed between S2-S4 and N2-N4. The cracks were around 6 inches above top of footing and measured approximately 0.6mm in width. Throughout ductility two, previous cracks observed during ductility 1.5 expanded up to 1mm in width. During the third cycle of ductility two, a flexural crack was observed on the top of the footing near the plastic hinge. The crack distribution at the end of ductility two can be seen in Figure 4-5. Previous cracks expanded up to 1.25mm during ductility three and concrete in the plastic hinge began to

flake. Figure 4-6 shows the crack distribution at the end of ductility three. During the second half cycle of ductility four ($\mu_4{}^{-1} = -4.61$ inches), crushing was observed between N2 and N3 approximately 5 inches above top of footing. During the next half cycle, crushing was observed between S2 and S3 near the footing. Crushing continued through the following cycles and can be seen in Figure 4-7.

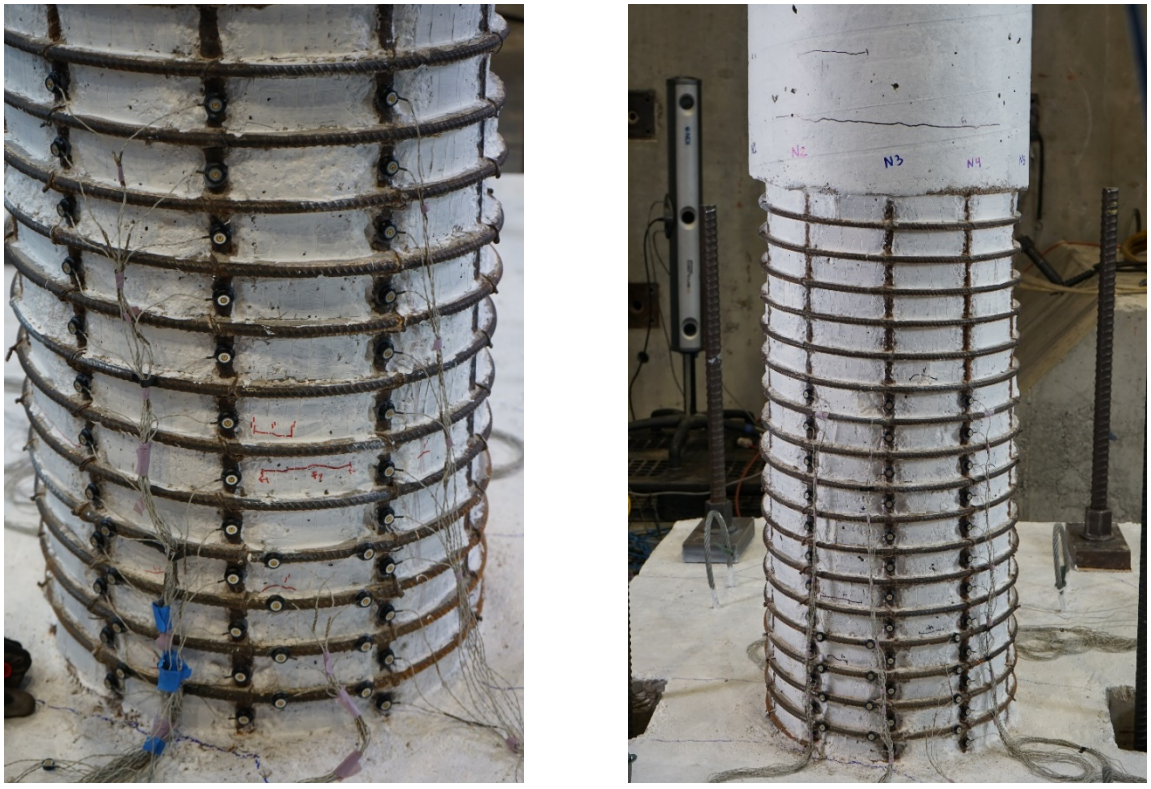



*Figure 4-4: Column test 1 crack distribution end of ductility one: (left) south side; (right) north side*



*Figure 4-5: Column test 1 crack distribution end of ductility two: (left) south side; (right) north side*



*Figure 4-6: Column test 1 crack distribution end of ductility three: (left) south side; (right) north side*



*Figure 4-7: Column test 1 crushing of concrete ductility four: (left) south side; (right) north side*

During ductility five, more crushing of the concrete core was observed. The South extreme fiber bar S3 showed early signs of buckling during the fourth half cycle of ductility five ($\mu_5{}^{-2} = -5.75$ inches), as shown in Figure 4-8. Bar S3 showed visible signs of buckling during the fourth half cycle of ductility six ($\mu_6{}^{-2} = -6.91$ inches). After the following half cycle ($\mu_6{}^{3} = 6.91$ inches), North extreme fiber bar N3 showed signs of buckling ($\mu_6{}^{3} = 6.91$ inches). The buckling of bars S3 and N3 are shown in Figure 4-9. Bar N2 showed signs of buckling after the first half cycle of ductility seven ($\mu_7{}^{1} = 8.05$ inches). During the following half cycle ($\mu_7{}^{-1} = -8.06$ inches), bar N3 fractured, followed by bar N2. It was also observed that Bar S4 was bucked. Fractured bars N2 and N3 are shown in Figure 4-10. During the next half cycle ($\mu_7{}^{2} = 8.06$ inches), bar S4 fractured, followed by S3. Fractured bars S3 and S4 are shown in Figure 4-11. The test concluded during the second cycle of ductility seven, after four bars had fractured and the maximum force dropped over 50%.



*Figure 4-8: Column test 1 early signs of buckling ductility five - bar S3*



*Figure 4-9: Column test 1 signs of buckling ductility six: (left) bar S3; (right) bar N3*



*Figure 4-10: Column test 1 fractured bars ductility seven: (left) bar N3; (right) bar N2*



*Figure 4-11: Column test 1 fractured bars ductility seven: (left) bar S4; (right) bar S3*

After the conclusion of the test, the excess crushed concrete was removed to better expose the longitudinal bars. Fractured bars N2 and N3 are shown in Figure 4-12, and fractured bars S3 and S4 are shown in Figure 4-13.



*Figure 4-12: Column test 1 fractured bars after test: (left) bar N3; (right) bar N2*



*Figure 4-13: Column test 1 fractured bars after test: (left) bar S4; (right) bar S3*

### *4.1.2 Special Note About Column Test 1*

As mentioned in Section 3.2.2, to measure axial and bending strains of the reinforcing steel, an optical 3D measurement system was utilized. The system used was the Optotrak Certus HD, a camera system capable of tracking the three-dimensional spatial coordinates of LED markers over time. A total of 112 markers were positioned on the outermost longitudinal bars and the first four layers of the spiral within the plastic hinge zone. Throughout the test, the 3D positions of the markers were recorded, and these measurements were later used to calculate the change in length between markers, which provided the strains along the longitudinal and transverse steel. Unfortunately, due to a system failure in the computer running the Optotrak software, all the data collected during the first column test was lost and could not be retrieved. As a result, unlike the other column tests, no strain data is presented for the first column test.

### *4.1.3 Hysteretic Energy Dissipation*

To determine the hysteretic damping of the columns, the area-based hysteretic damping (Jacobsen's damping), was calculated for the first cycle of each ductility. In this approach, numerical integration is utilized to calculate the area inside each hysteretic loop, denoted as "A1" in Figure 4-14. A rectangle is then formed around the loop by connecting the maximum and minimum force and displacement values for each cycle. This rectangle is identified as "A2" as shown in Figure 4-14. Hysteretic damping is then calculated using Equation 4-1.

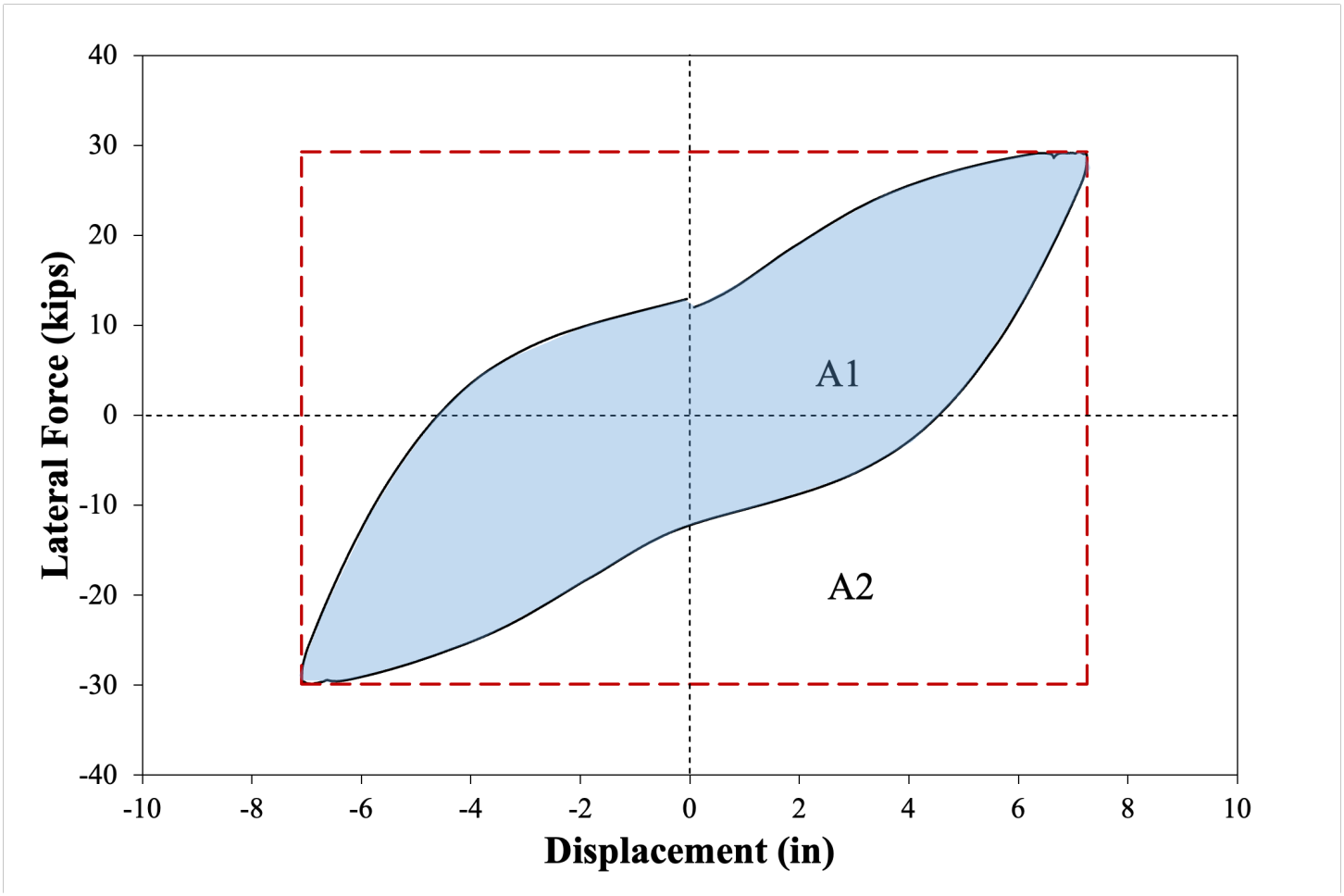



*Figure 4-14: Jacobsen's damping calculation example*

$$\xi_{hyst} = \frac{2}{\pi} \cdot \frac{A1}{A2} \qquad \textit{Equation 4-1}$$

However, based on non-linear time history analysis performed by Priestley et al. (2007), it was concluded that Jacobsen's damping tended to overestimate the damping of a system. Based on the findings of Priestley et al. (2007), Montejo et al. (2010) developed a correction factor to more accurately reflect hysteretic damping. The corrected equation for hysteretic damping can be

seen in Equation 4-2. The hysteretic damping components of Jacobsen's Damping ($\xi_{hyst}$) and the corrected hysteretic damping ($\xi_{hyst,corr}$) were plotted for each ductility and can be seen in Figure 4-15. The hysteretic damping is directly proportional to the energy dissipated by the column.

$$\xi_{hyst,corr} = \xi_{hyst}\left[(0.53\mu + 0.8)\xi_{hyst}^{-\left(\frac{\mu}{40}+0.4\right)}\right] \qquad \textit{Equation 4-2}$$

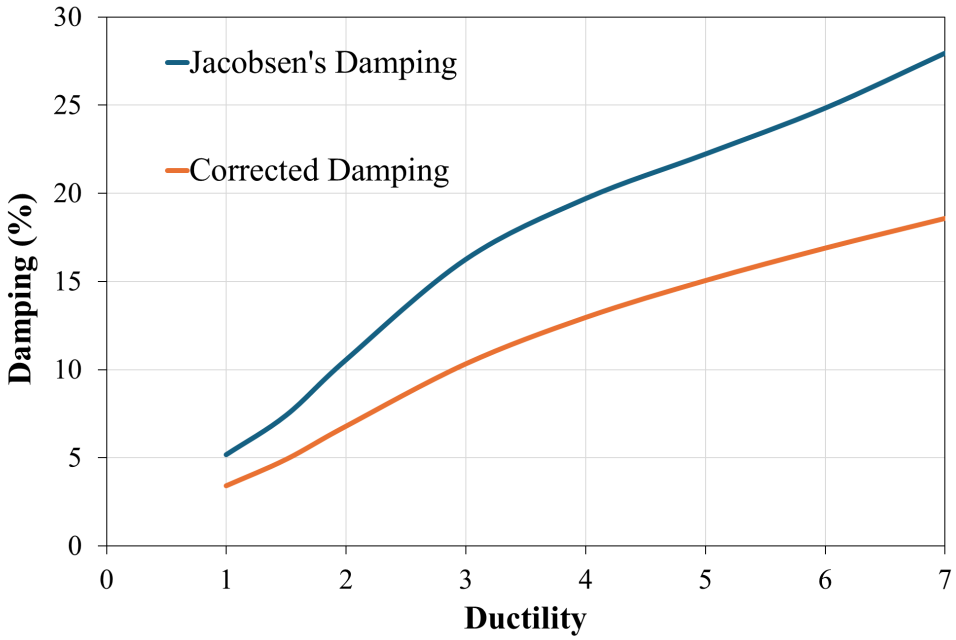



*Figure 4-15: Column test 1 hysteretic damping*

## 4.2 Column Test 2 Summary

Column Test 2 was conducted at the Constructed Facilities Laboratory on February 29th, 2024. The column featured 5% corrosion (defined by mass loss) in the plastic hinge. Table 4-4 summarizes column parameters and damage observations.

*Table 4-4: Column test 2 parameters and results summary*

**Load History**: Symmetric Three Cycle Quasi Static

**Column Parameters:**

| | |
|---|---|
| Corrosion Level: | 5% |
| Concrete Compressive Strength: | $f$c' = 6662 psi |
| Corroded Longitudinal Bars Strength: | fy = 59.8 ksi |
| Axial Load: | $P$ = 144 kips ($P$/($f$c'$A$g) = 10%) |
| Column Length and Aspect Ratio: | 8ft (L/D = 5.33) |
| Equivalent Yield Displacement: | $\Delta_y$ = 1.15" |
| Maximum Lateral Force: | 29.82 kips |
| Failure Mode: | Fracture of buckled longitudinal steel |

**Damage Observations:**

| | |
|---|---|
| First Cracking North: | -3/4 $F_y$' = -0.591" |
| First Cracking South: | 3/4 $F_y$' = 0.481" |
| Concrete Crushing North: | $\mu_4^{+1}$ = 4.61" |
| Concrete Crushing South: | $\mu_4^{-1}$ = -4.60" |
| Longitudinal Bar Buckling North; N3: | $\mu_6^{+3}$ = 6.91" |
| Longitudinal Bar Buckling South; S3: | $\mu_6^{-3}$ = -6.91" |
| Longitudinal Bar Fracture North; N3: | $\mu_7^{-2}$ = -8.08" |
| Longitudinal Bar Fracture South; S3: | $\mu_7^{+3}$ = 8.05" |

Material tests were performed on the reinforcing steel (uncorroded and corroded) and the concrete used in the column. Figure 4-16 shows the stress-strain responses of the uncorroded and corroded steel specimens, and Table 4-5 summarizes the results. For the corroded specimen, bar N3 was extracted from the column after the test. Because the bar was removed from the plastic hinge after testing, the bar was already yielded, hence the roundhouse behavior seen in Figure

4-16. Compression tests were performed on concrete samples on the day of the test. The results are summarized in Table 4-6.

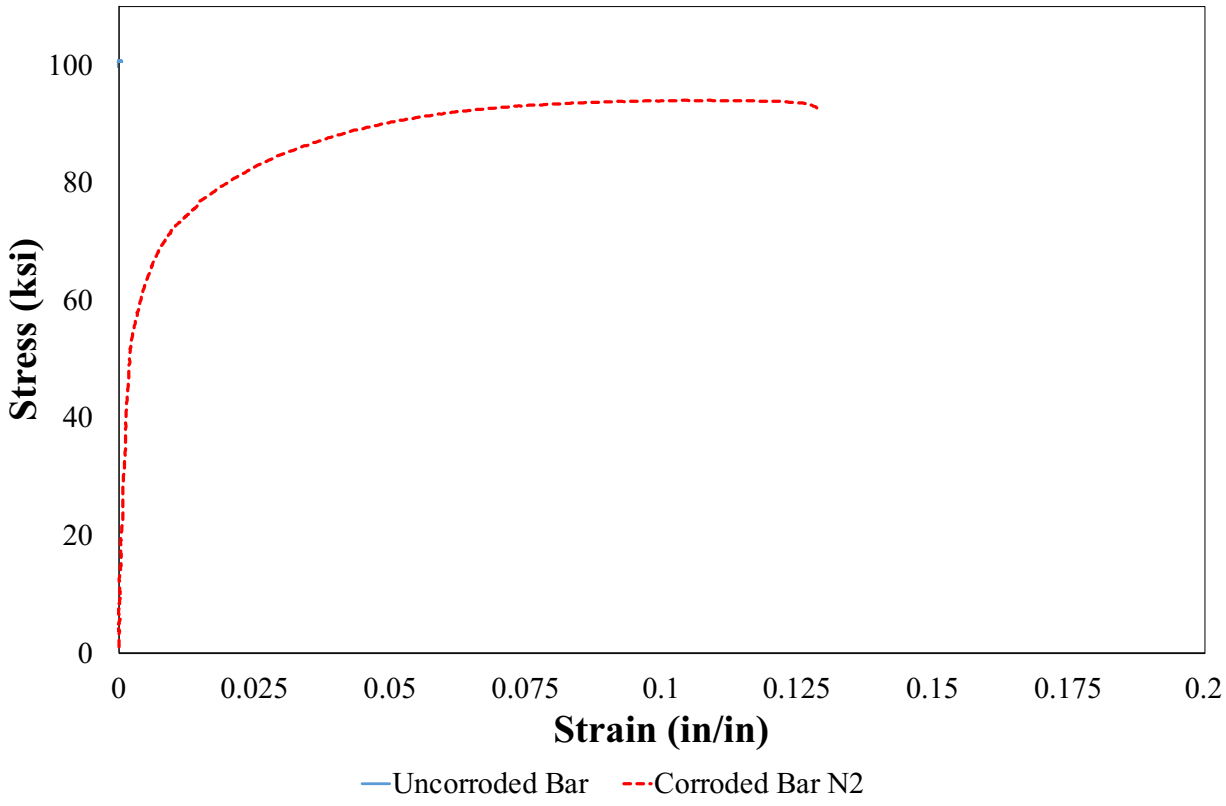



*Figure 4-16: Column test 2 stress-strain response material tests*

*Table 4-5: Column test 2 material tension test results*

| Steel | Yield Stress (ksi) | Yield Strain (%) | Maximum Stress (ksi) | Strain at Maximum Stress (%) |
|---|---|---|---|---|
| Uncorroded bar | 68.5 | 0.22 | 100.2 | 11.6 |
| Corroded bar N3 | 59.8 | 0.37 | 94.9 | 10.1 |

*Table 4-6: Column test 2 concrete compression strength results*

| Column Concrete | | Footing Concrete | |
|---|---|---|---|
| **Cylinder** | **Stress (psi)** | **Cylinder** | **Stress (psi)** |
| 1 | 7031 | 1 | 7603 |
| 2 | 7185 | 2 | 7382 |
| 3 | 6621 | 3 | 7161 |
| **Average** | 6946 | **Average** | 7382 |

During the test, cracks and damage states in the column were marked and recorded between half cycles. Prior to the test, while post-tensioning was underway, several surface cracks were observed in the footing. These cracks were distinguished by marking them in blue, differentiating them from cracks that emerged during the test. Cracks on the South side of the column were denoted with red marks, whereas those on the North side were marked with black. The test concluded during the third cycle of ductility seven, after two bars had fractured and the maximum force dropped by over 30%. Figure 4-17 shows the force-displacement response, while Figure 4-18 presents the load history.

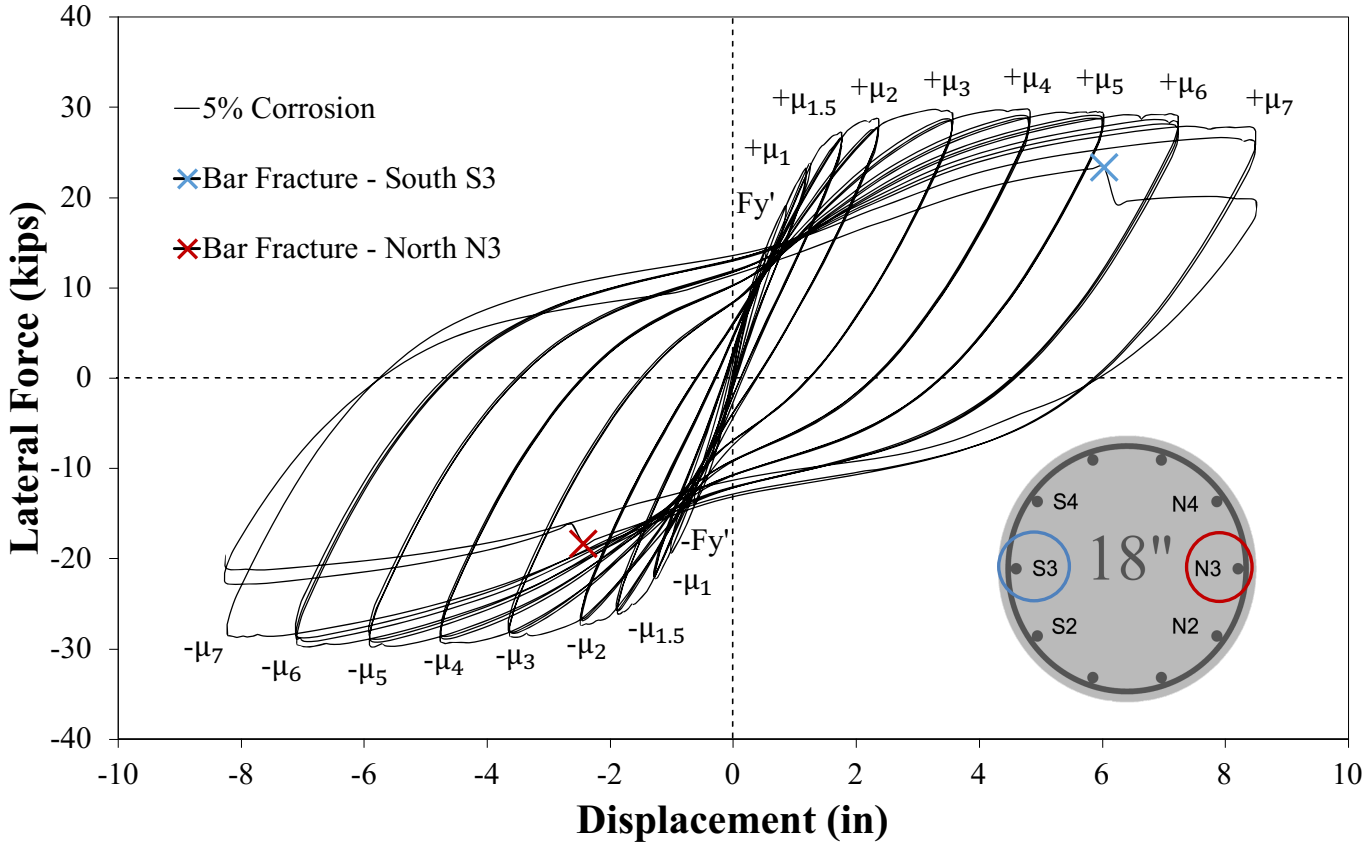



*Figure 4-17: Column test 2 force-displacement response*

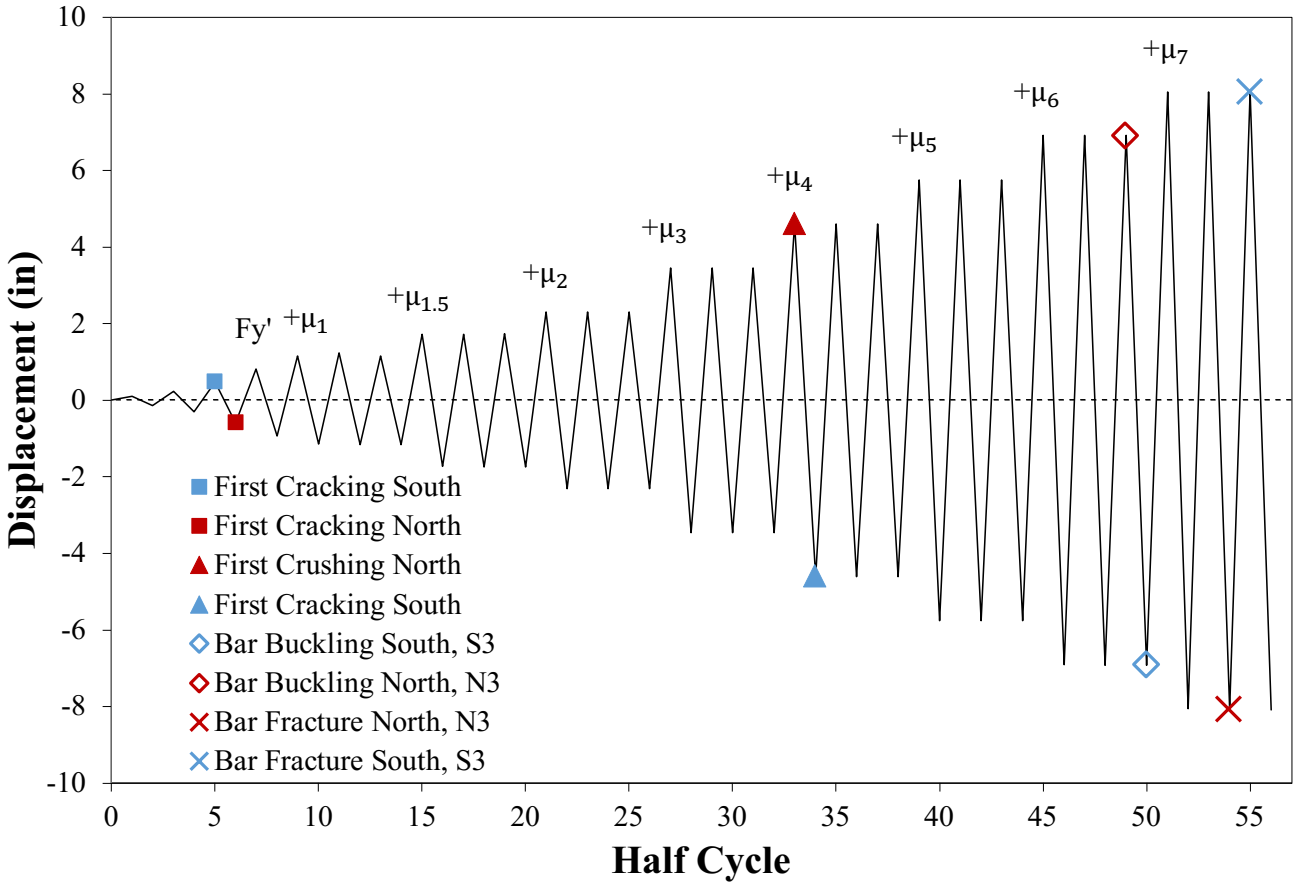



*Figure 4-18: Column test 2 load history*

### *4.2.1 Damage Progression*

Hairline cracks were observed on the South side of the column during three quarters of first yield force ($\frac{3}{4}F_y' = 14.28\ kips$). The cracks were located near spirals approximately 8 inches above top of footing. Hairline cracks appeared on the North side during the next half cycle ($-\frac{3}{4}F_y' = -14.24\ kips$). During ductility one, more hairline cracks developed in the plastic hinge approximately 6 inches above top of footing, as well as in the cover of the column. The crack distribution at the end of ductility one can be seen in Figure 4-19. During ductility 1.5, previous cracks expanded to 0.5mm and multiple flexural cracks were observed between extreme longitudinal bars. Throughout ductility two, previous cracks observed during ductility 1.5 expanded up to 0.8mm in width. The crack distribution at the end of ductility two can be seen in Figure 4-20. Previous cracks expanded up to 1mm during ductility three and concrete approximately 6 inches above top of footing began to flake. Figure 4-21 shows the crack

distribution at the end of ductility three. During the first half cycle of ductility four ($\mu_4{}^1 = 4.61$ inches), crushing was observed on the South side of the column between N2 and N3 approximately 5 inches above top of footing. During the next half cycle, crushing was observed between S2 and S3 near the footing. Crushing continued through the following cycles and can be seen in Figure 4-22.

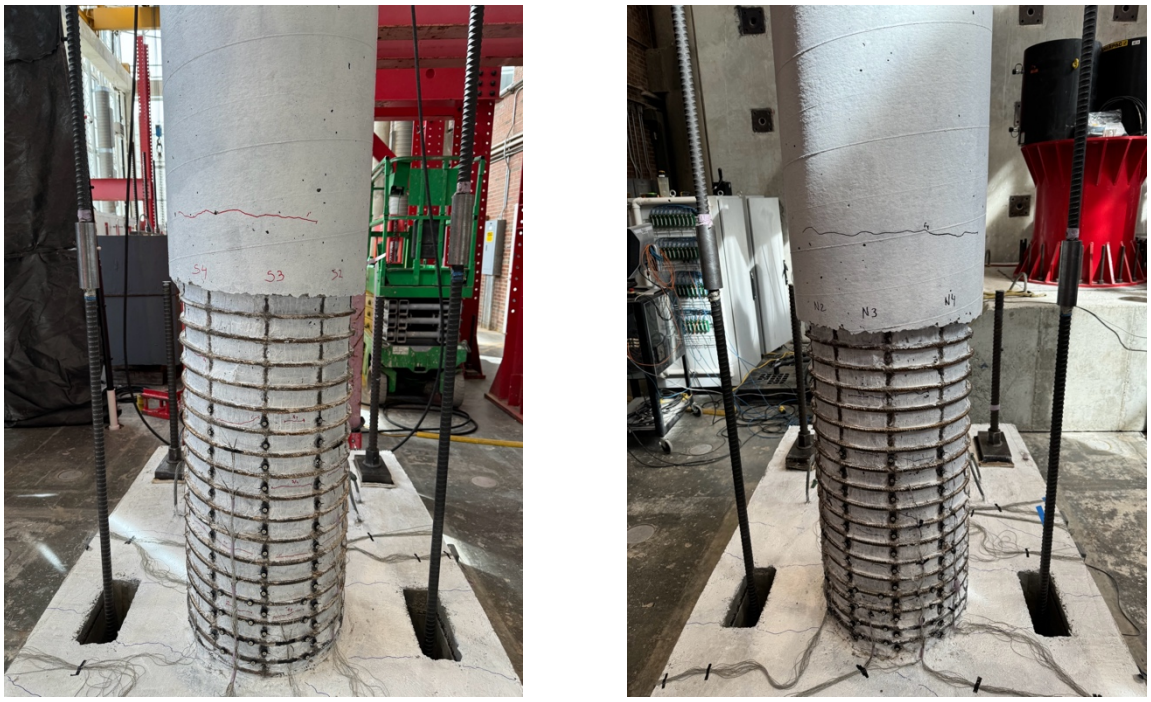



*Figure 4-19: Column test 2 crack distribution end of ductility one: (left) south side; (right) north side*

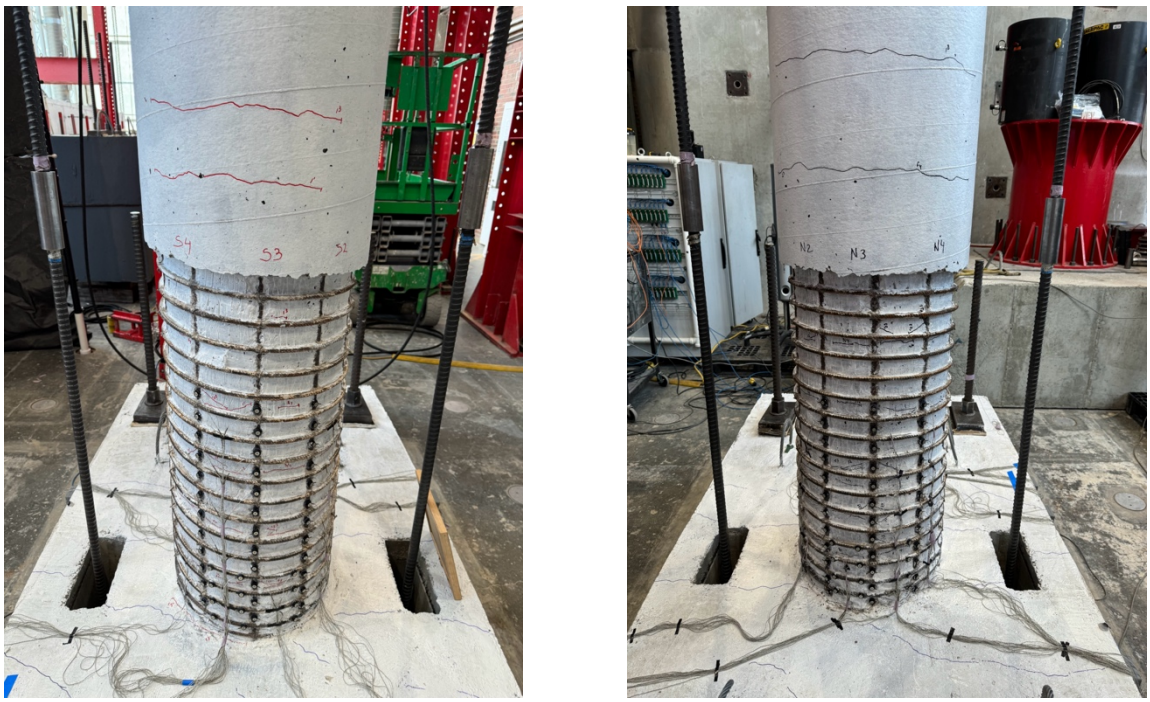



*Figure 4-20: Column test 2 crack distribution end of ductility two: (left) south side; (right) north side*

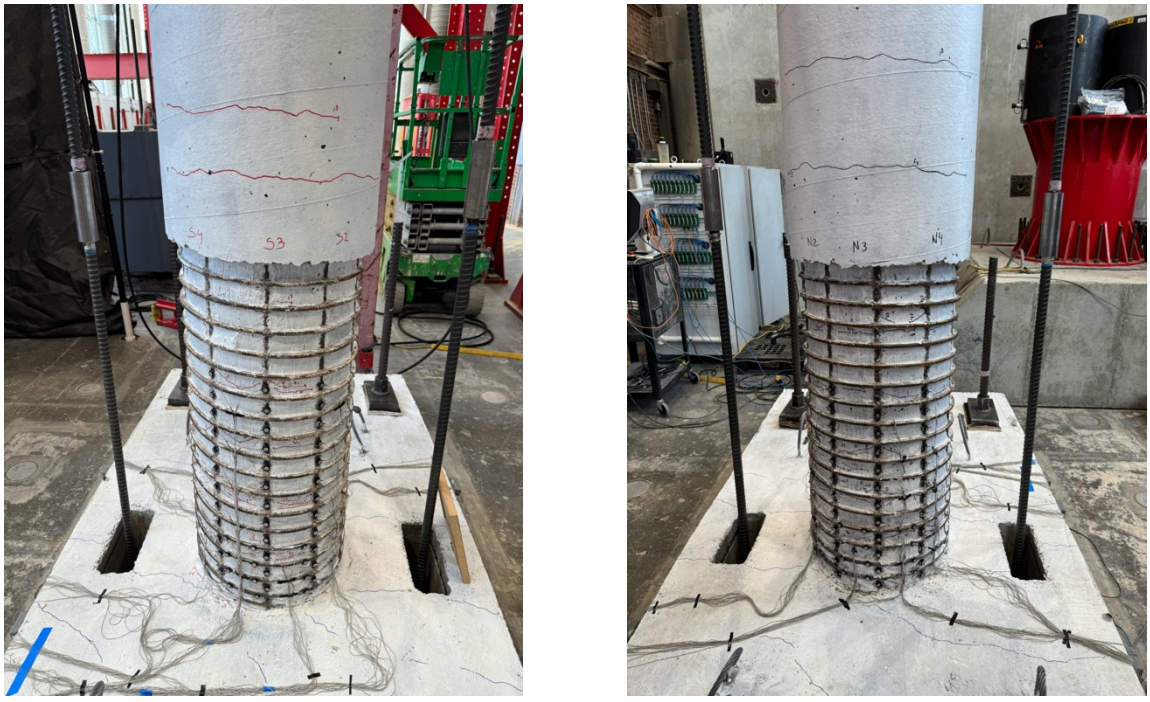



*Figure 4-21: Column test 2 crack distribution end of ductility three: (left) south side; (right) north side*

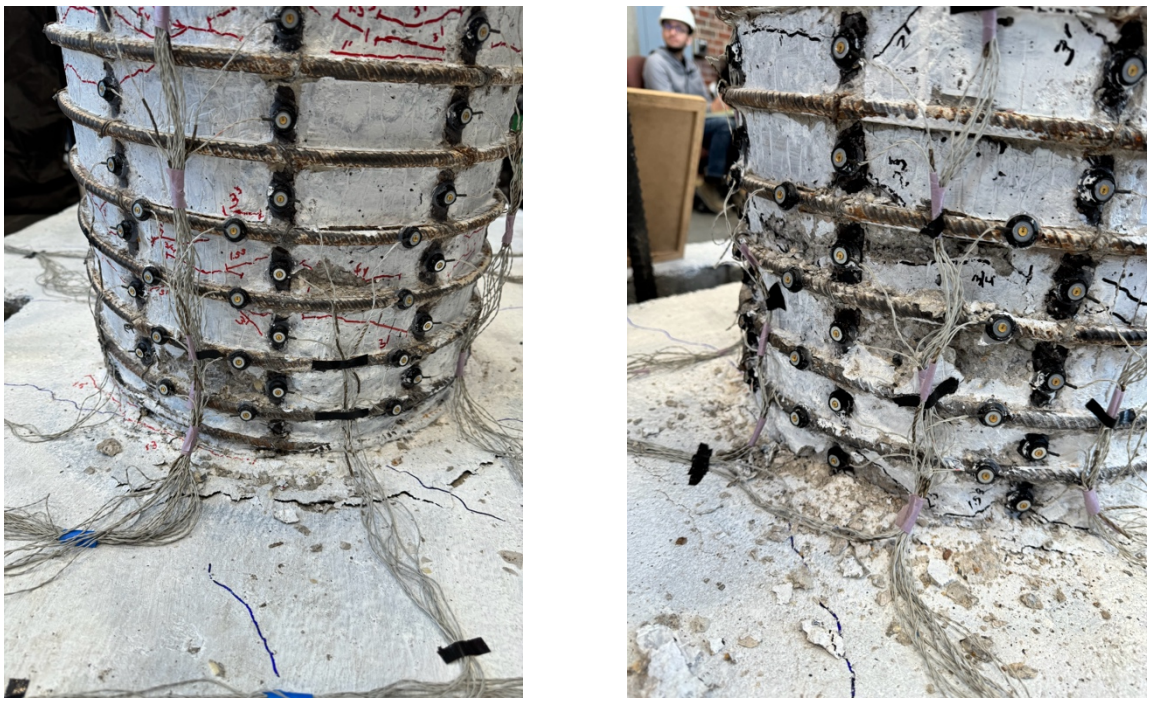


*Figure 4-22: Column test 2 crushing of concrete ductility four: (left) south side; (right) north side*

During ductility five, more crushing of the concrete core near base of column was observed. More crushing of concrete around the extreme longitudinal bars was observed throughout ductility six. The North extreme fiber bar N3 buckled during the fifth half cycle of ductility six ($\mu_6{}^3 = 6.91$ inches). Bar S3 buckled during the next half cycle ($\mu_6{}^{-3} = -6.91$ inches). The buckling of bars N3 and S3 can be seen Figure 4-23. Buckling of bars N3 and S3 continued into ductility seven. During the fourth half cycle of ductility seven ($\mu_7{}^{-2} = -8.08$ inches), bar N3 fractured. Fractured bar N3 can be seen in Figure 4-24. Bar S3 fractured the following half cycle ($\mu_7{}^3 = 8.05$ inches), as can be seen in Figure 4-25. It was also observed bar N2 was buckled. The test concluded during the last cycle of ductility seven, after two bars had fractured and the maximum force dropped over 50%.



*Figure 4-23: Column test 2 buckling during ductility six: (left) bar N3; (right) bar S3*



*Figure 4-24: Column test 2 fractured bar ductility seven – bar N3*



*Figure 4-25: Column test 2 fractured bar ductility seven – bar S3*

### *4.2.2 Strain Analysis*

To determine strains in the longitudinal and transverse steel, position data from the Optotrak LED markers was analyzed. Strains at any given time, *t*, were calculated by dividing the change in length between two LED markers by their initial gage length ($L_0$) as seen in Equation 4-3 To find the change in length, the distance between their 3D coordinates was calculated using Equation 4-4.

$$\varepsilon(t) = \frac{L(t) - L_0}{L_0} \qquad \textit{Equation 4-3}$$

$$L(t) = \sqrt{(x_2(t) - x_1(t))^2 + (y_2(t) - y_1(t))^2 + (z_2(t) - z_1(t))^2} \qquad \textit{Equation 4-4}$$

A total of 112 LED markers were instrumented to the exposed reinforcing steel in the lower half of the column. The extreme bars on the North side (N2, N3, N4) and South side (S2, S3, S4) were instrumented along with the transverse steel in the same region. Strain profiles of the extreme North and South bars, N3 and S3, for the first cycle of each ductility following yield, are shown in Figure 4-26.

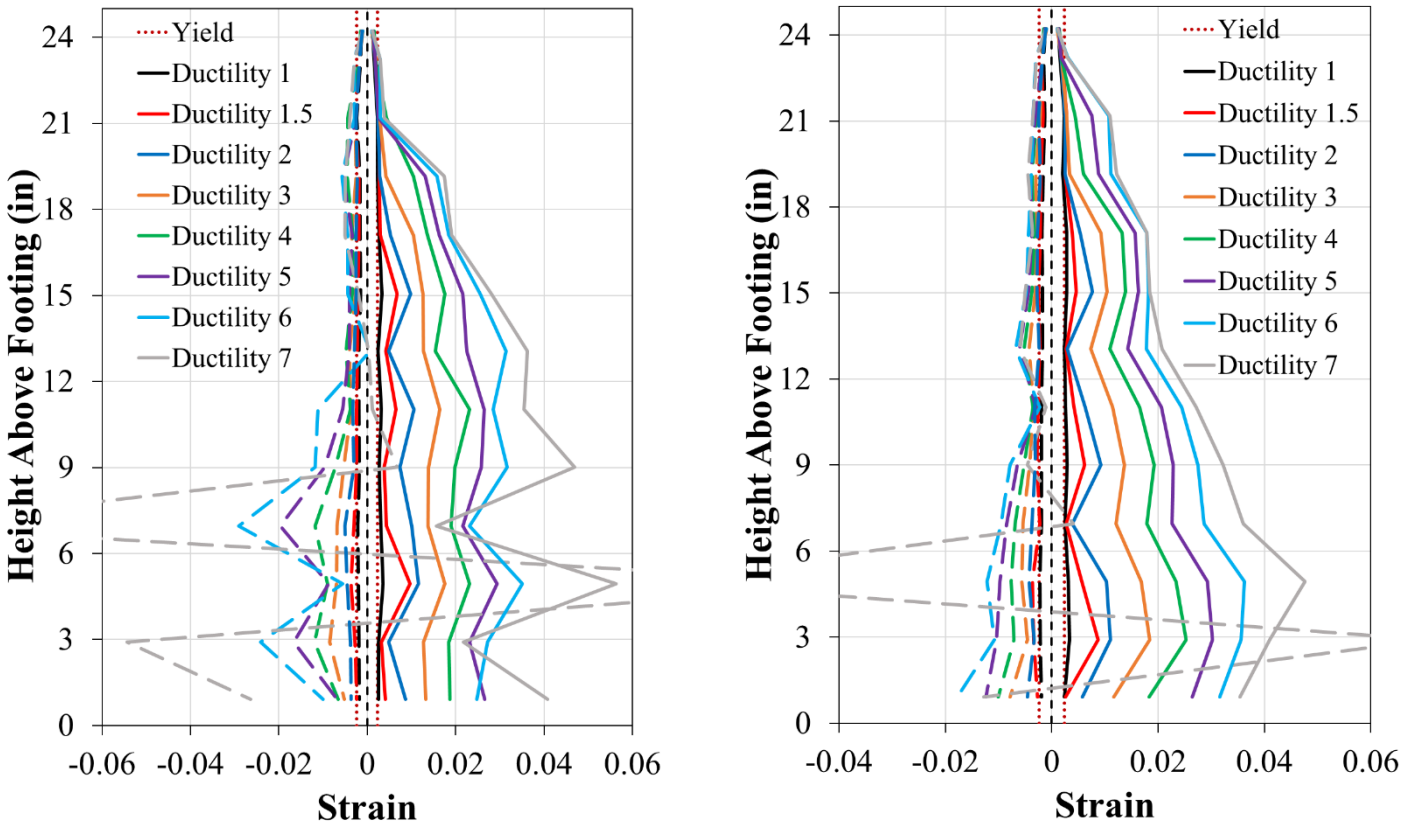



*Figure 4-26: Column test 2 strain profiles after yield: (a) bar N3; (b) bar S3*

The solid lines in Figure 4-26 depict positive tension strain, while the dashed lines represent negative compressive strains. The sporadic behavior of the dashed lines in ductility 7 represent the bar buckling. The North and South bars of the column had an approximate spread of plasticity of 21 inches and 23 inches from top of footing, respectively.

During the test, bar buckling was initially observed visually. However, bar buckling can also be observed by plotting strain versus column displacement, as seen in Figure 4-27. Bar buckling can be seen when a gauge experiences additional tension in the buckled region, and additional compression above and below the buckled region, as seen in Figure 4-28. As displacements increase and bars begin to buckle, the sign convention of strain no longer corresponds to the sign convention of column displacement. For gages in the buckled region, strain becomes positive during negative displacement, as seen in Figure 4-27 (a), as a result of LEDs moving further apart, as shown in Figure 4-28. For gages above and below the buckled region, the

LEDs move closer together as the bar buckles, as seen in Figure 4-28, leading to increased strains during negative displacement.

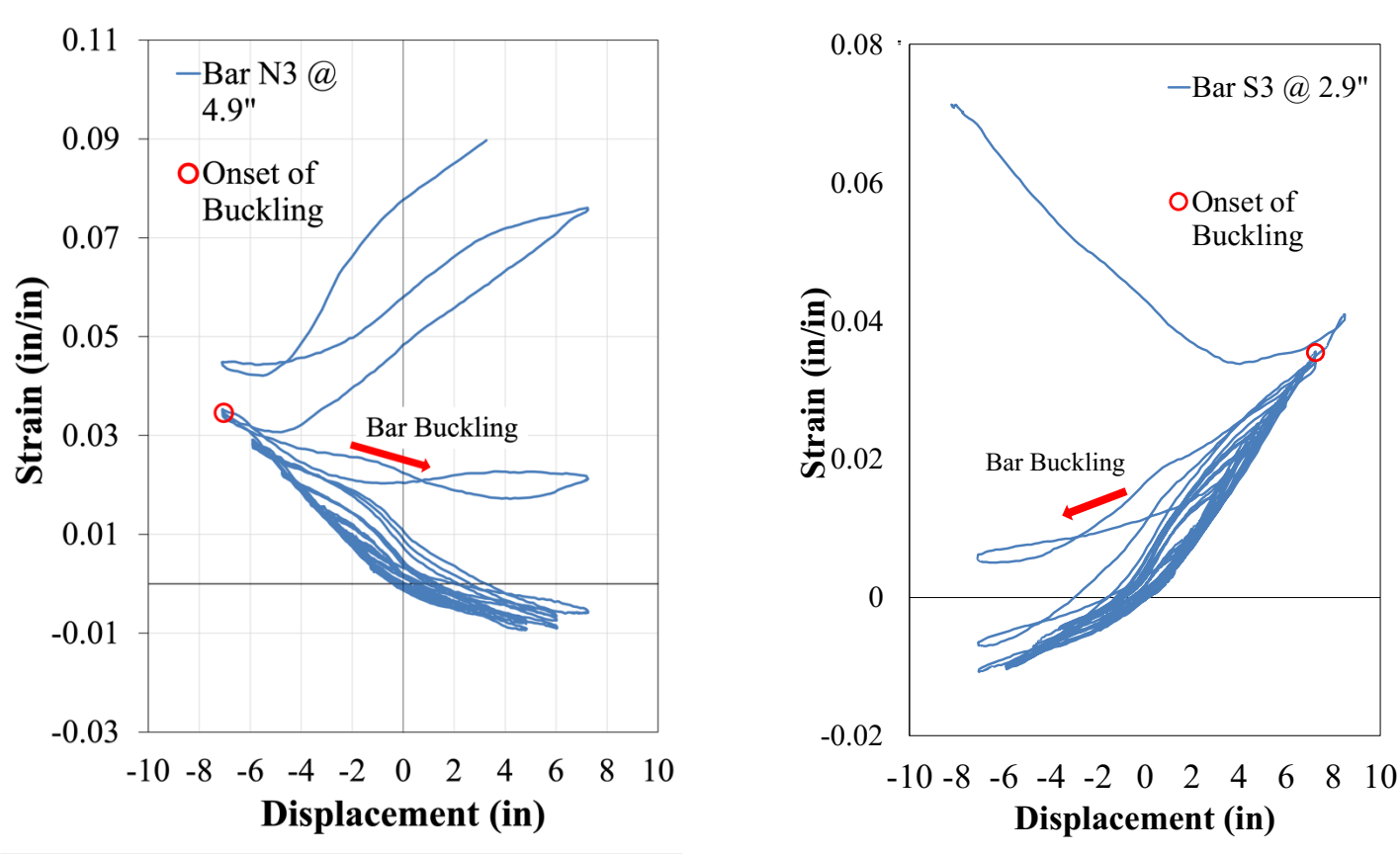



*Figure 4-27: Column test 2 strain vs. displacement: (a) bar N3; (b) bar S3*

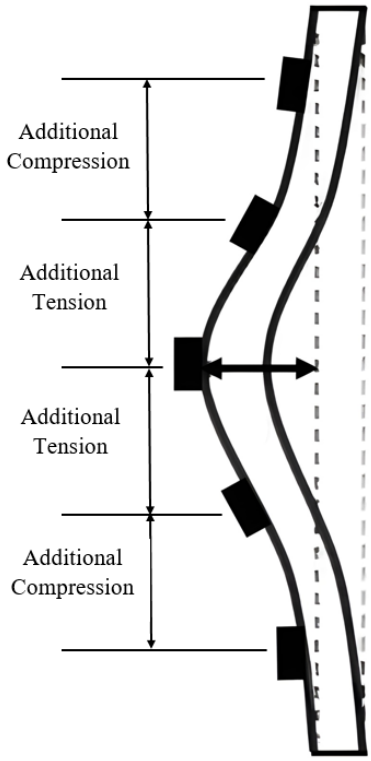
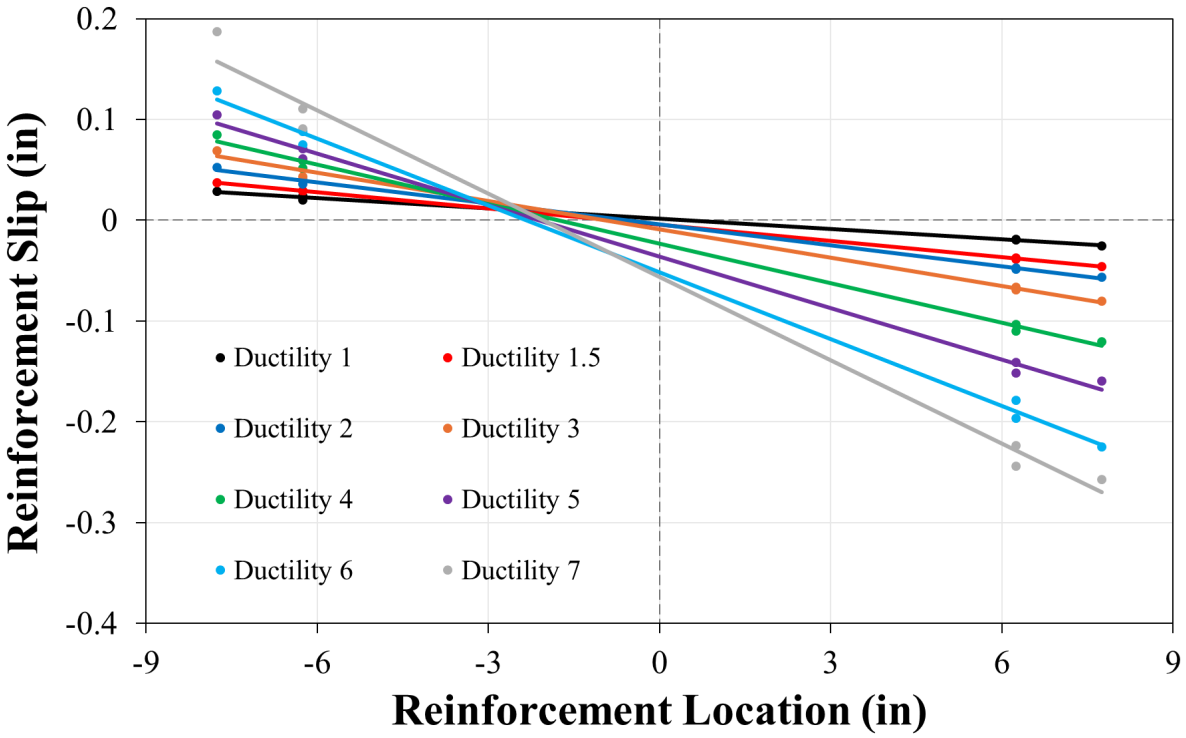


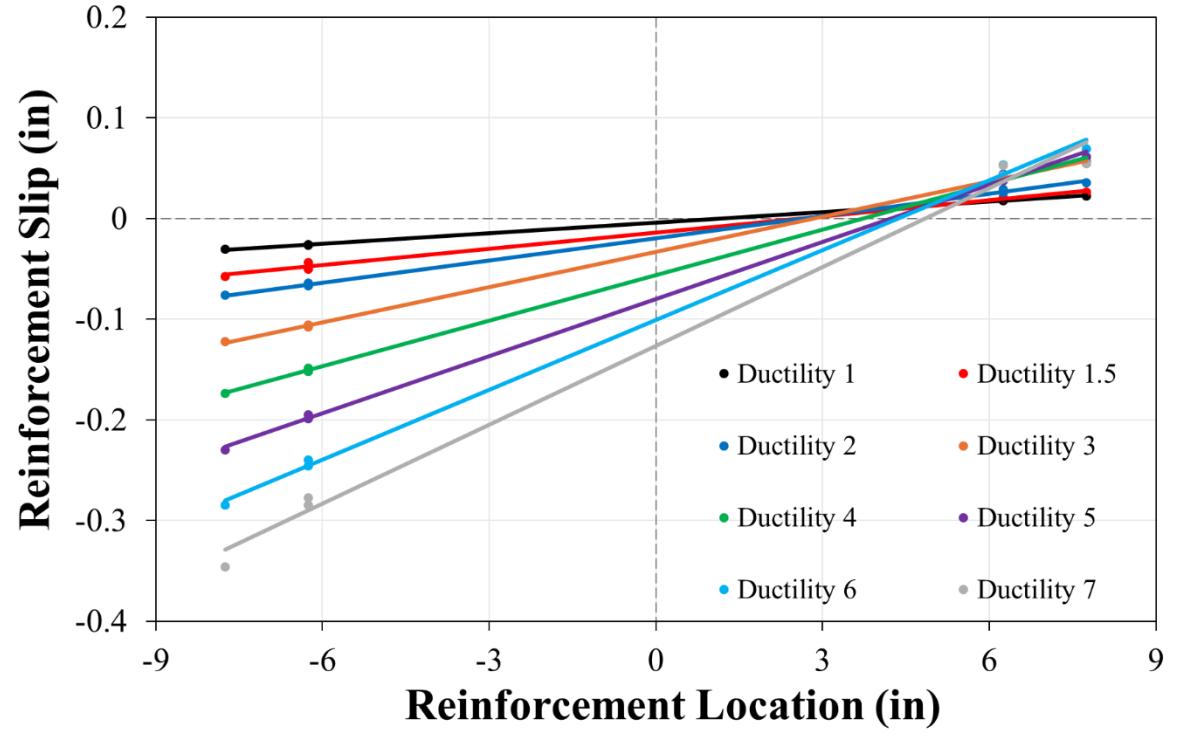

*Figure 4-28: LEDs on buckled bar*

### *4.2.3 Components of Displacement*

According to Priestley et al. (2007), flexural deformation and rotation of the column due to bond slip, or strain penetration, are the two main components of column displacement. To determine strain penetration of the column, the starting position of the bottom LEDs on the three extreme fiber bars on each side of the column served a baseline height during the test. The position of the LEDs for the first cycle of each ductility were then subtracted from the baseline height to calculate slip. A line was then fit through the data points and the slope gave the rotation angle due to strain penetration. The rotation angle due to strain penetration was then multiplied by the height of the column to give displacement due to strain penetration. Figure 4-29 shows the reinforcement slip from Column Test 2.




(a)




(b)

*Figure 4-29: Column test 2 bond slip of extreme fiber bars: (a) south side under push cycles; (b) north side under pull cycles*

As mentioned earlier, along with strain penetration, a column will also undergo flexural deformation. Flexural deformation makes up most of the lateral deformation experienced by a column and is concentrated in the column's lower region, referred to as the plastic hinge. To find flexural deformation, strain data, previously calculated in Section 4.2.2 was used. A linear curve was fit through the strain data points and the slope was calculated as the curvature. Figure 4-30 shows the curvature distribution over the instrumented height of the column from the first cycle of each ductility.

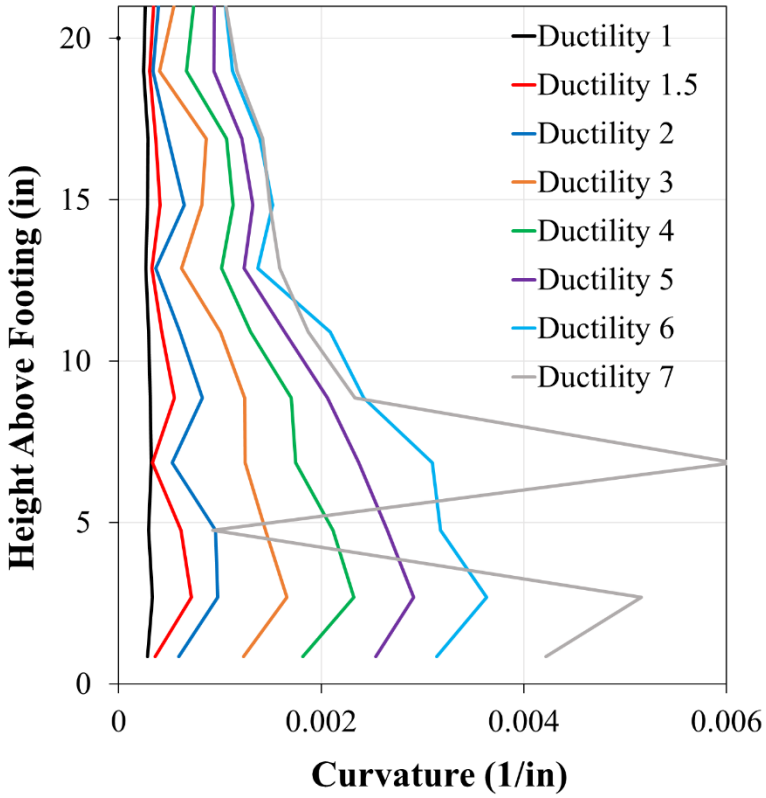



*Figure 4-30: Column test 2 curvature profile*

The individual contributions of both flexural and rotational displacements compared to measured column displacement can be seen in Figure 4-31. The differences in displacements are attributed to errors in calculation methods as well as instrumentation.

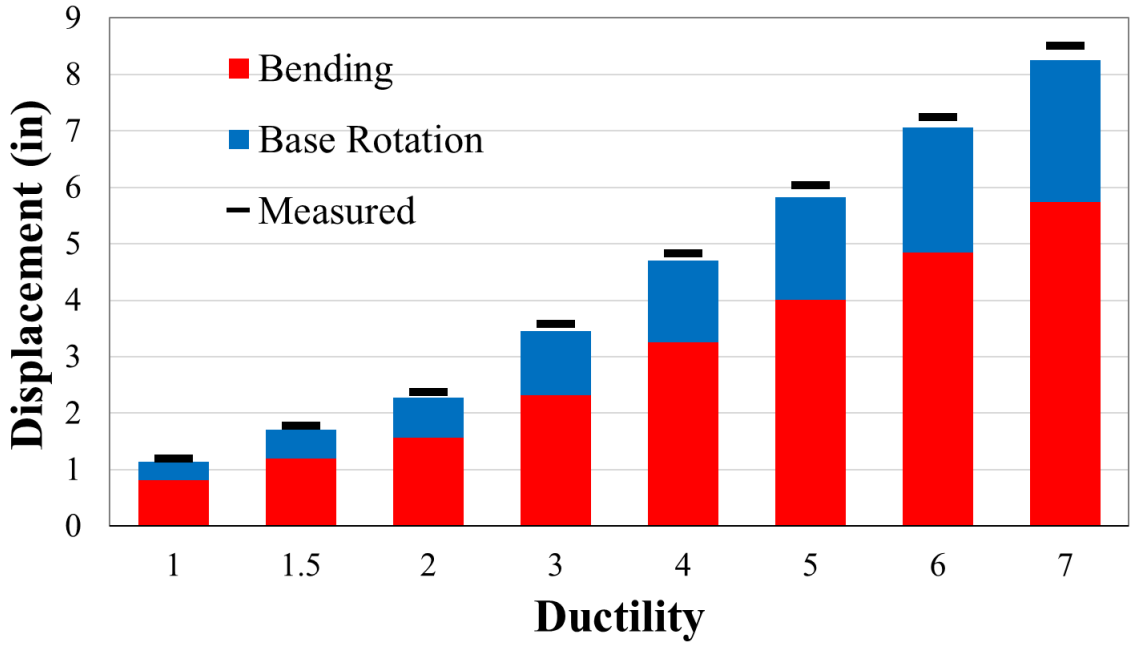



*Figure 4-31: Column test 2 components of displacement*

### *4.2.4 Hysteretic Energy Dissipation*

To determine the hysteretic damping of the columns, the area-based hysteretic damping (Jacobsen's damping), was calculated for the first cycle of each ductility. As described in Section 4.1.4, Jacobsen's hysteretic damping, Equation 4-1, was corrected using Equation 4-2. The hysteretic damping components of Jacobsen's Damping ($\xi_{hyst}$) and the corrected hysteretic damping ($\xi_{hyst,corr}$) were plotted for each ductility and can be seen in Figure 4-32. The hysteretic damping is directly proportional to the energy dissipated by the column.

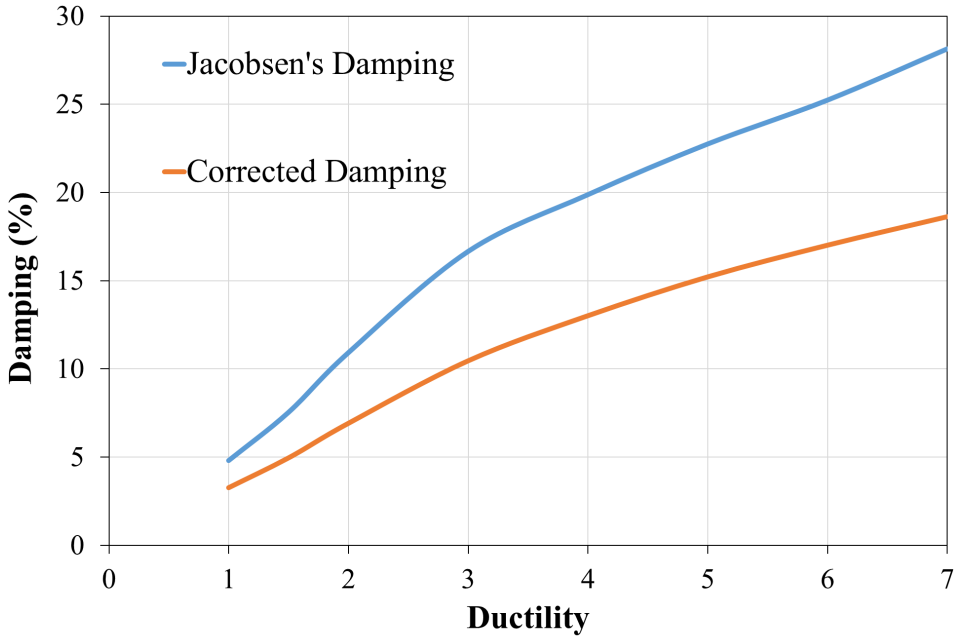



*Figure 4-32: Column test 2 hysteretic damping*

### *4.2.5 Strain Limit States*

The strain histories of the longitudinal bars are crucial for identifying important damage limit states of the column such as concrete cracking, concrete crushing, bar buckling, and bar fracture. These limit states can then be compared to serviceability and damage control limit states proposed by Kowalsky (2000), as seen in Table 4-7.

*Table 4-7: Performance limit states. Kowalsky (2000)*

| Limit State | Concrete Strain Limit | Steel Strain Limit |
|---|---|---|
| Serviceability | 0.004 (compression) | 0.015 (tension) |
| Damage Control | 0.018 (compression) | 0.060 (tension) |

As illustrated in Section 4.2.2, strains were calculated for the extreme North and South bars, N3 and S3, using Equation 4-3 and Equation 4-4. The strain at the damage limit states for Test 2 can be seen in Table 4-8. For concrete cracking and crushing, the maximum strain values were determined at the ductility level where the corresponding damage was observed. Concrete crushing was typically measured during compression cycles. For bar buckling, the strain values were determined by plotting strain versus displacement, as shown in Section 4.2.2. The reported

buckling strain was the maximum tension strain observed before the bar buckled upon reversal, as illustrated in Figure 4-27.

*Table 4-8: Column test 2 strain at damage limit states*

| Damage State | Measured Strain (in/in) | |
|---|---|---|
| | North, N3 | South, S3 |
| Concrete Cracking | 0.0005 | 0.0010 |
| Concrete Crushing | 0.0080 | 0.0068 |
| Bar Buckling | 0.0346 | 0.0355 |

## 4.3 Column Test 3 Summary

Column Test 3 was conducted at the Constructed Facilities Laboratory on June 11th, 2024. The column featured 30% corrosion (defined by mass loss) in the plastic hinge. Table 4-9 summarizes column parameters and damage observations.

*Table 4-9: Column test 3 parameters and results summary*

**Load History**: Symmetric Three Cycle Quasi Static

**Column Parameters:**

| | |
|---|---|
| Corrosion Level: | 30% |
| Concrete Compressive Strength: | $f$c' = 6560 psi |
| Corroded Longitudinal Bars Strength: | fy = 52.5 ksi |
| Axial Load: | $P$ = 144 kips ($P$/($f$c'$A$g) = 10%) |
| Column Length and Aspect Ratio: | 8ft (L/D = 5.33) |
| Equivalent Yield Displacement: | $\Delta_y$ = 1.15" |
| Maximum Lateral Force: | 23.21 kips |
| Failure Mode: | Fracture of buckled longitudinal steel |

**Damage Observations:**

| | |
|---|---|
| First Cracking North: | $F_y$' = 0.82" |
| First Cracking South: | -$F_y$' = -0.93" |
| Concrete Crushing North: | $\mu_3^{-1}$ = -3.43" |
| Concrete Crushing South: | $\mu_3^{+1}$ = 3.43" |
| Longitudinal Bar Buckling South; S3: | $\mu_6^{-1}$ = -6.86" |
| Longitudinal Bar Buckling North; N3: | $\mu_6^{+2}$ = 6.86" |
| Longitudinal Bar Fracture South; S3: | $\mu_6^{+3}$ = 6.86" |
| Longitudinal Bar Fracture North; N3: | $\mu_6^{-3}$ = -6.87" |
| Longitudinal Bar Buckling North; N2: | $\mu_7^{+1}$ = 8.00" |
| Longitudinal Bar Buckling South; S2: | $\mu_7^{-1}$ = -8.01" |
| Longitudinal Bar Fracture North; N2: | $\mu_7^{-2}$ = -8.01" |

Material tests were conducted on both the reinforcing steel (uncorroded and corroded) and the concrete utilized in the column. Figure 4-33 shows the stress-strain responses of the uncorroded and corroded steel specimens, while Table 4-10 summarizes the results. For the corroded

specimen, a rebar specimen, identical to the longitudinal bars used in the column construction, was corroded to the same level of corrosion as the column. Compression tests were performed on concrete samples on the day of the test. The results are summarized in Table 4-11.

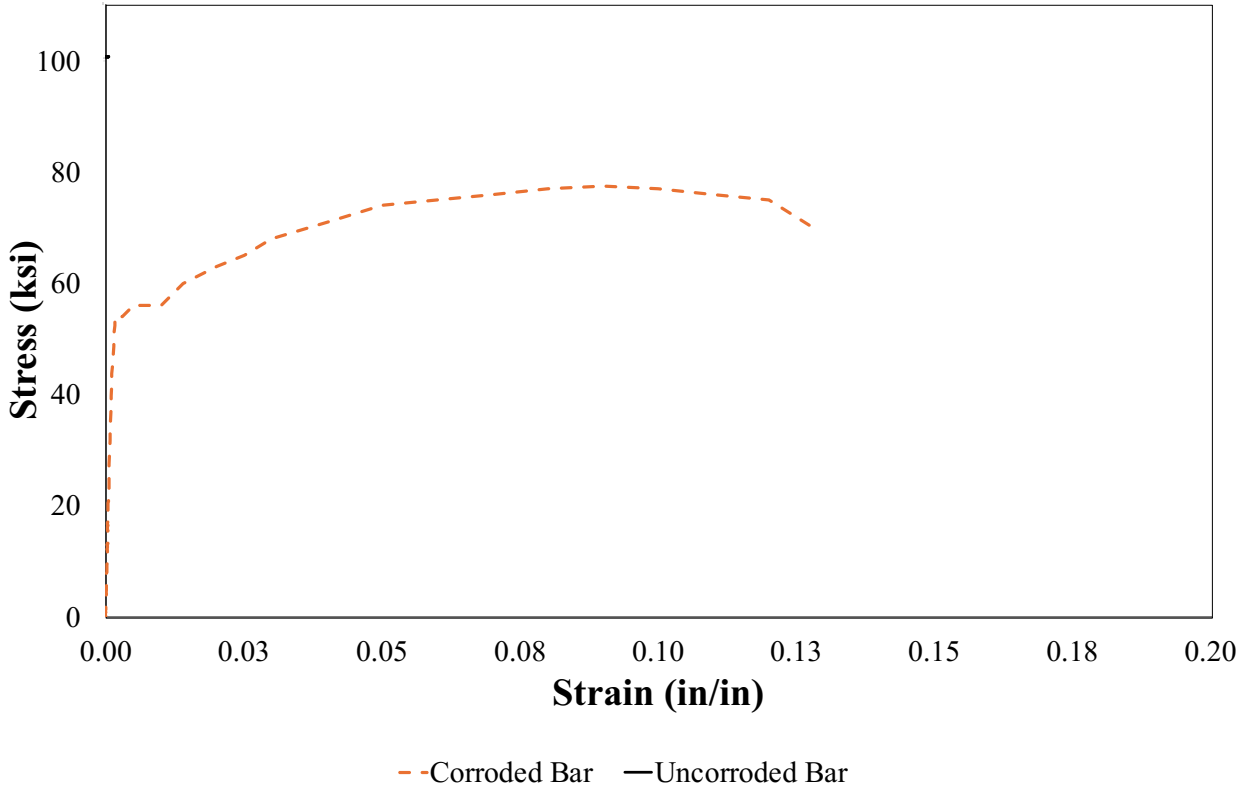



*Figure 4-33: Column test 3 stress-strain response material tests*

*Table 4-10: Column test 3 material tension test results*

| Steel | Yield Stress (ksi) | Yield Strain (%) | Maximum Stress (ksi) | Strain at Maximum Stress (%) |
|---|---|---|---|---|
| Uncorroded bar | 68.5 | 0.22 | 100.2 | 11.6 |
| Corroded bar | 52.5 | 0.15 | 77.5 | 9.5 |

*Table 4-11: Column test 3 concrete compression strength results*

| Column Concrete | | Footing Concrete | |
|---|---|---|---|
| **Cylinder** | **Stress (psi)** | **Cylinder** | **Stress (psi)** |
| 1 | 6478 | 1 | 4390 |
| 2 | 6464 | 2 | 4250 |
| 3 | 6738 | 3 | 4521 |
| **Average** | 6560 | **Average** | 4387 |

During the test, cracks and damage states in the column were marked and recorded between half cycles. Prior to the test, while post-tensioning was underway, several surface cracks were observed in the footing. These cracks were distinguished by marking them in blue, differentiating them from cracks that emerged during the test. Cracks on the South side of the column were denoted with red marks, whereas those on the North side were marked with black. The test concluded during the second cycle of ductility seven, after three bars had fractured and the maximum force dropped by over 50%. The force-displacement response is shown in Figure 4-34, while the load history is presented in Figure 4-35.

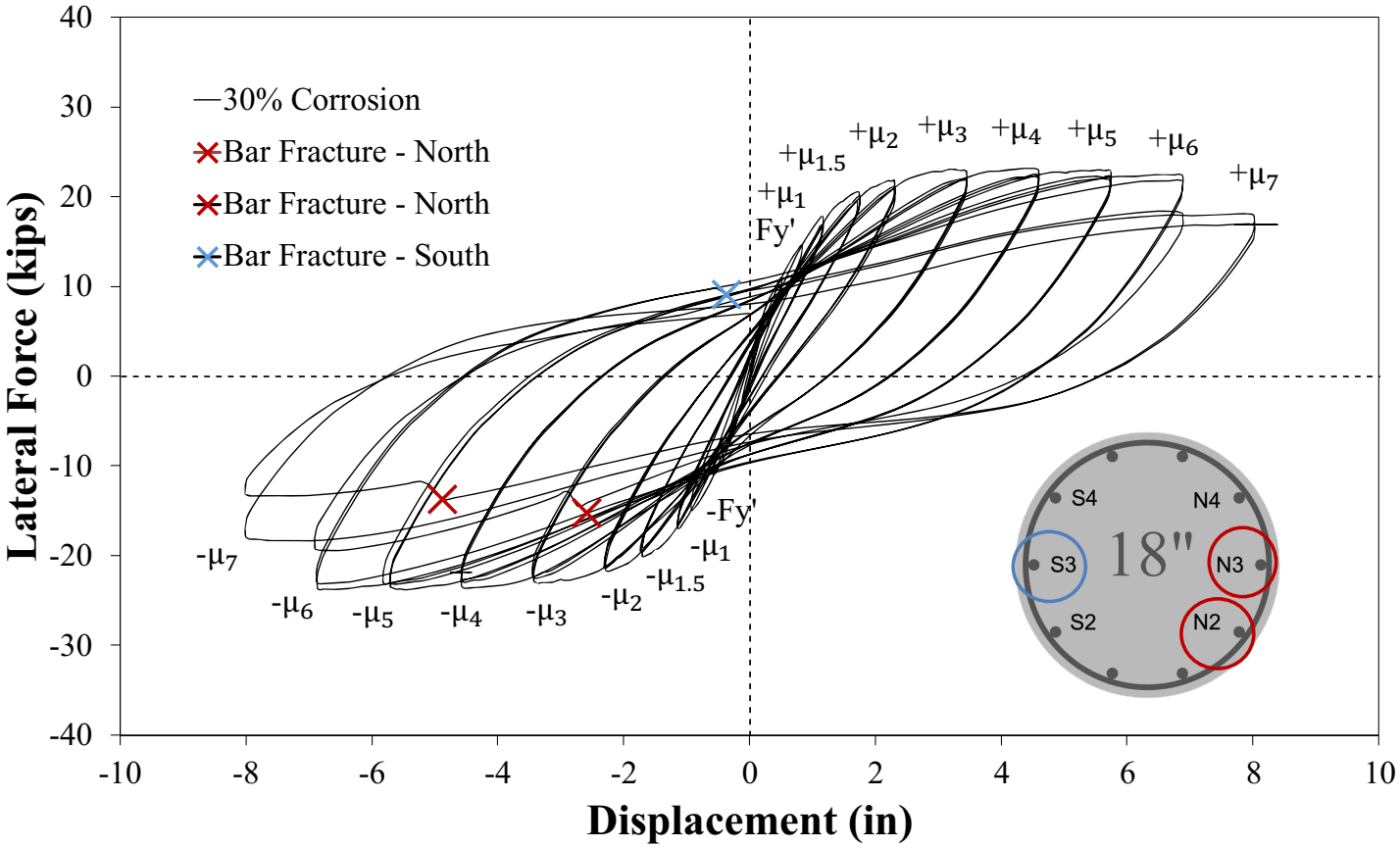



*Figure 4-34: Column test 3 force-displacement response*

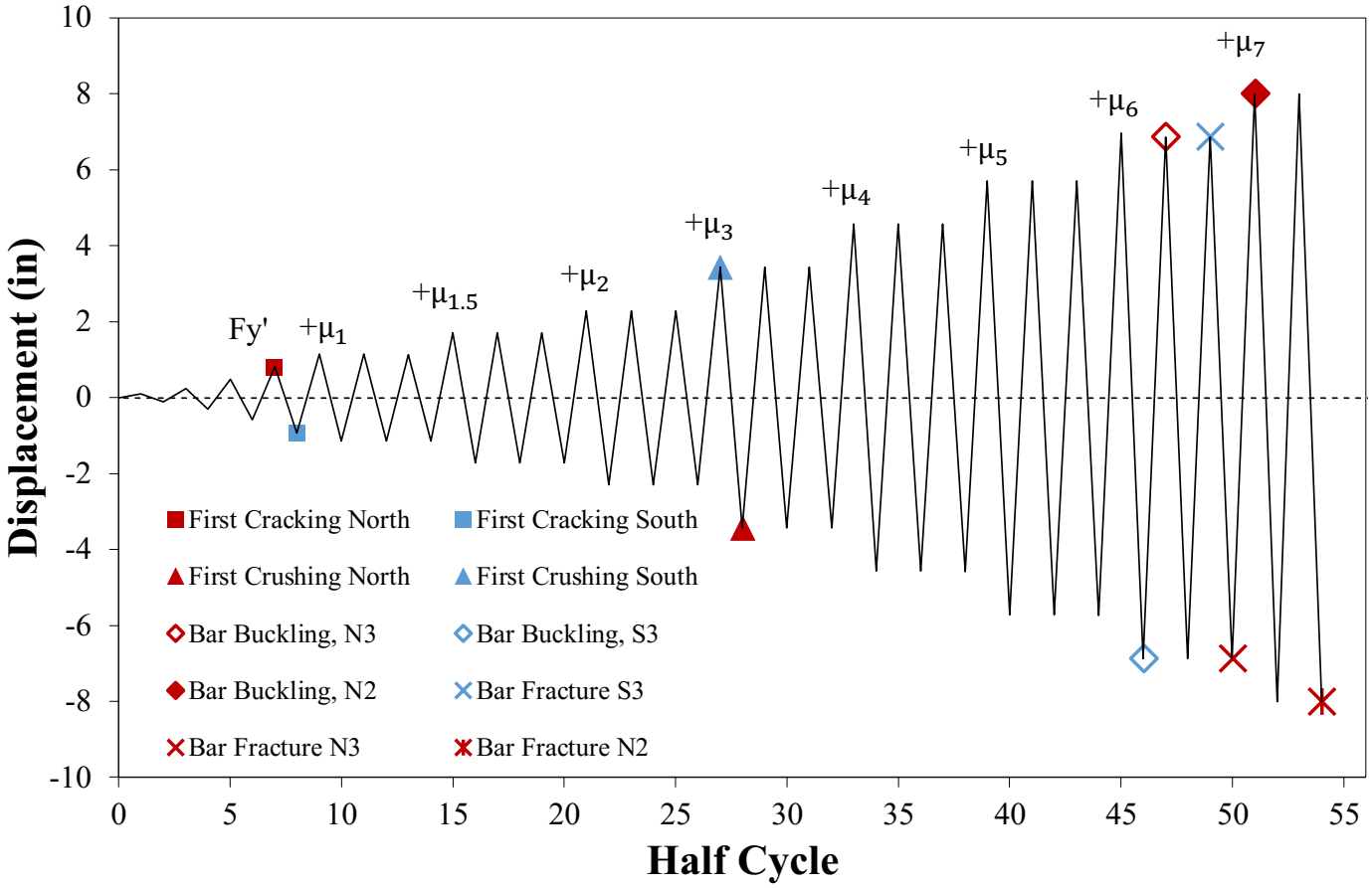



*Figure 4-35: Column test 3 load history*

### *4.4.1 Damage Progression*

Hairline cracks were observed on the North side of the column during the pull cycle of first yield force ($-F_y{}' = -15.05\ kips$). The cracks were located between N3 and N4 and near spirals approximately 10 inches above top of footing. Hairline cracks appeared on the South side during the next half cycle ($\mu_1{}^1 = 1.15$ inches). During ductility one, more hairline cracks developed in the plastic hinge approximately 8 to 10 inches above top of footing. The crack distribution at the end of ductility one can be seen in Figure 4-36. During ductility 1.5, previous cracks expanded to 1.0mm and multiple flexural cracks were observed between extreme longitudinal bars. Throughout ductility two, previous cracks observed during ductility 1.5 expanded up to 1.25mm in width and flaking was observed at the base of the column near N2. The crack distribution at the end of ductility two can be seen in Figure 4-37. During the second half cycle of ductility three ($\mu_3{}^{-1} = -3.43$ inches), cracking sounds were heard, and crushing was observed at the base of the column

near N3. During the remaining cycles of ductility three, more crushing was observed near bars N3 and S3 as seen in Figure 4-38.

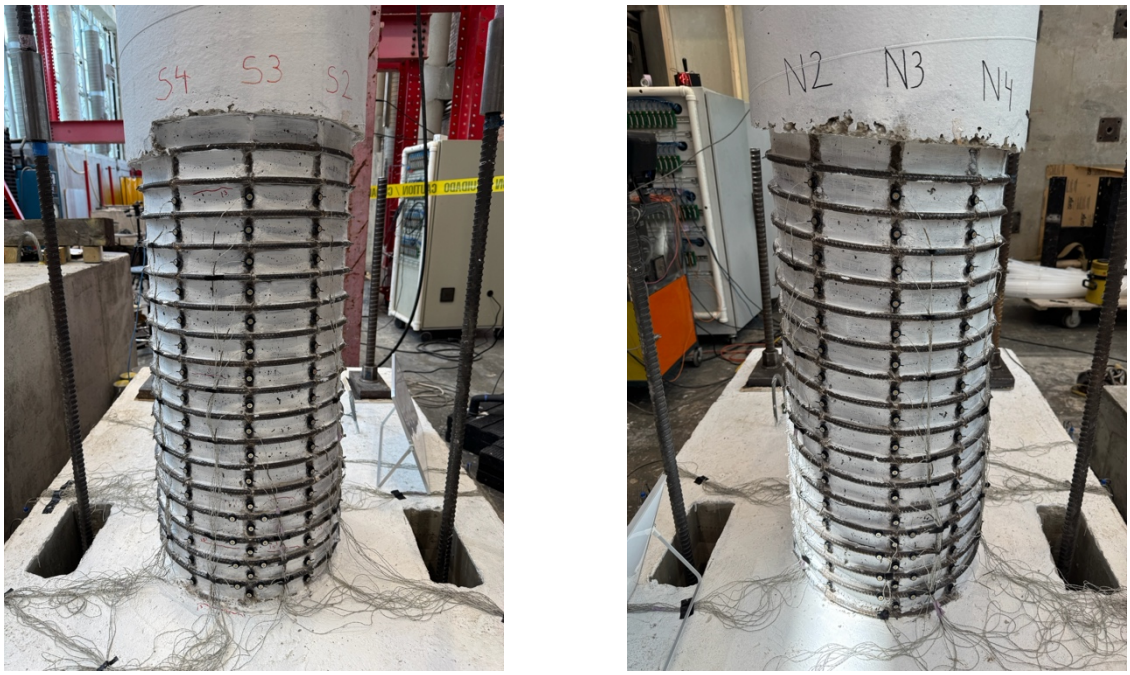



*Figure 4-36: Column test 3 crack distribution end of ductility one: (left) south side; (right) north side*

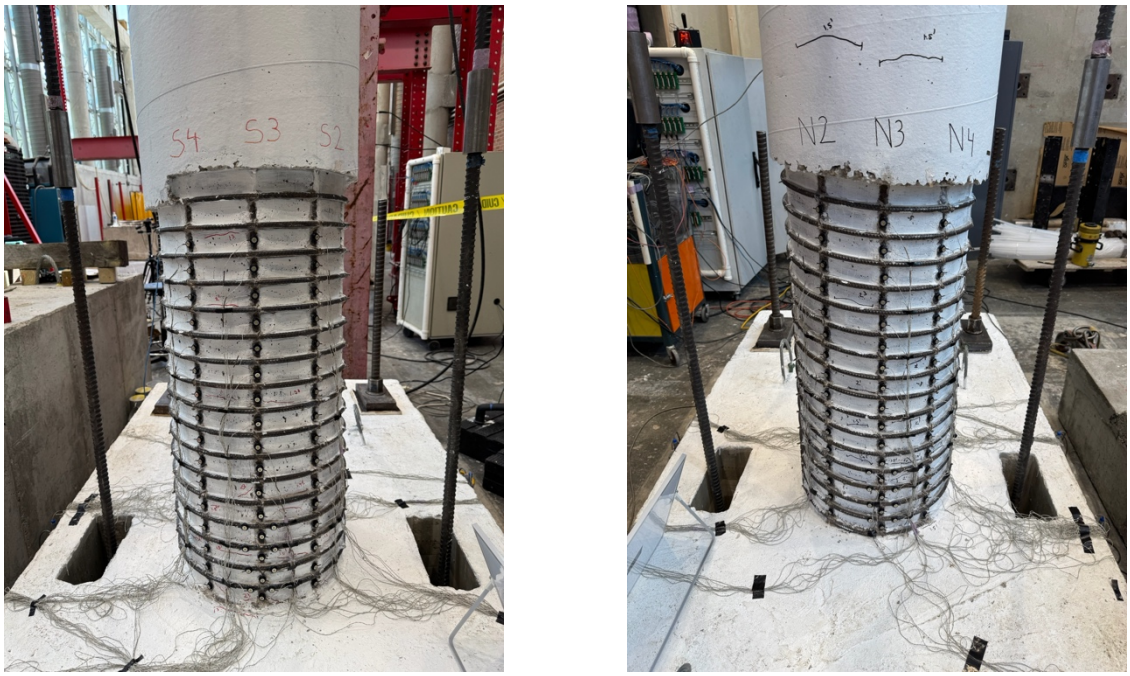



*Figure 4-37: Column test 3 crack distribution end of ductility two: (left) south side; (right) north side*



*Figure 4-38: Column test 3 crushing of concrete ductility three: (left) south side; (right) north side*

During ductility four and five, more crushing of the concrete core near the extreme longitudinal bars was observed. The South extreme fiber bar S3 buckled during the second half cycle of ductility six (${\mu_6}^{-1} = 6.91$ inches). Bar N3 buckled during the next half cycle (${\mu_6}^{+2} = 6.86$ inches). The buckling of bars S3 and N3 can be seen Figure 4-39. During the fifth half cycle of ductility six (${\mu_6}^{+3} = 6.86$ inche), bar S3 fractured. The fracture of S3 occurred approximately 11 inches above top of footing. Fractured bar S3 can be seen in Figure 4-40. Bar N3 fractured the following half cycle (${\mu_6}^{-3} = -6.87$ inches), as can be seen in Figure 4-41. During the first half cycle of ductility seven (${\mu_7}^{+1} = 8.00$ inches), bar N2 buckled near the top of footing. During the next half cycle (${\mu_7}^{-1} = -8.00$ inches), bar S2 buckled four inches above top of footing. Bar N2 fractured during the fourth half cycle of ductility seven (${\mu_7}^{-2} = -8.00$ inches), as seen in Figure 4-42. The test concluded following the fracture of N2, after three bars had fractured and the maximum force dropped over 50%.



*Figure 4-39: Column test 3 buckling during ductility six: (left) bar S3; (right) bar N3*



*Figure 4-40: Column test 3 fractured bar ductility six – bar S3*



*Figure 4-41: Column test 3 fractured bar ductility seven – bar N3*



*Figure 4-42: Column test 3 fractured bar ductility seven – bar N2*

### *4.4.2 Strain Analysis*

To determine strains in the longitudinal and transverse steel, position data from the Optotrak LED markers was analyzed. Strains were calculated using Equation 4-3 and Equation

4-4, as illustrated in Section 4.2.2. Strain profiles of the extreme North and South bars, N3 and S3, for the first cycle of each ductility following yield, are shown in Figure 4-43. Due to multiple LEDs falling off the reinforcing steel during ductility seven, the results for ductility seven are not included.

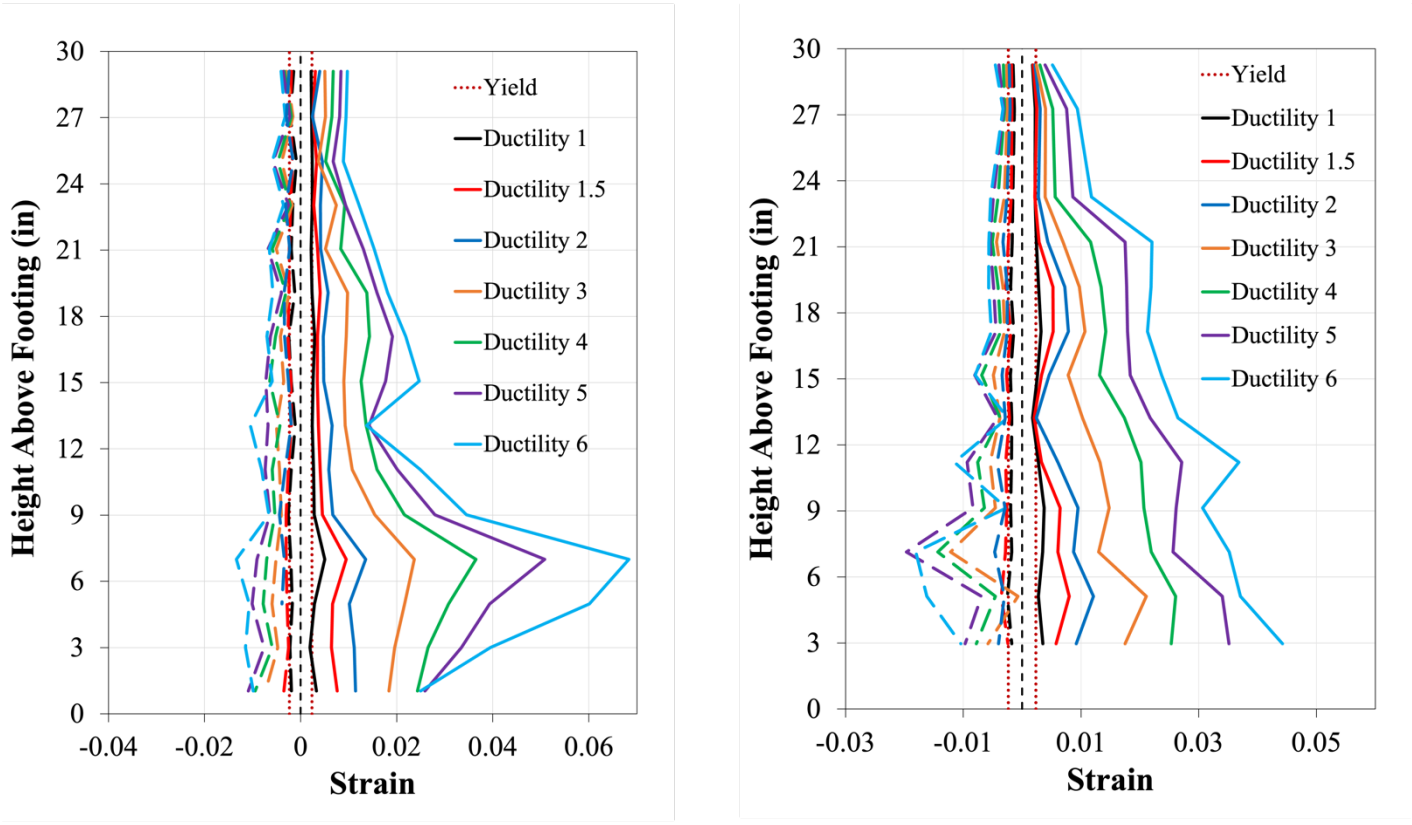
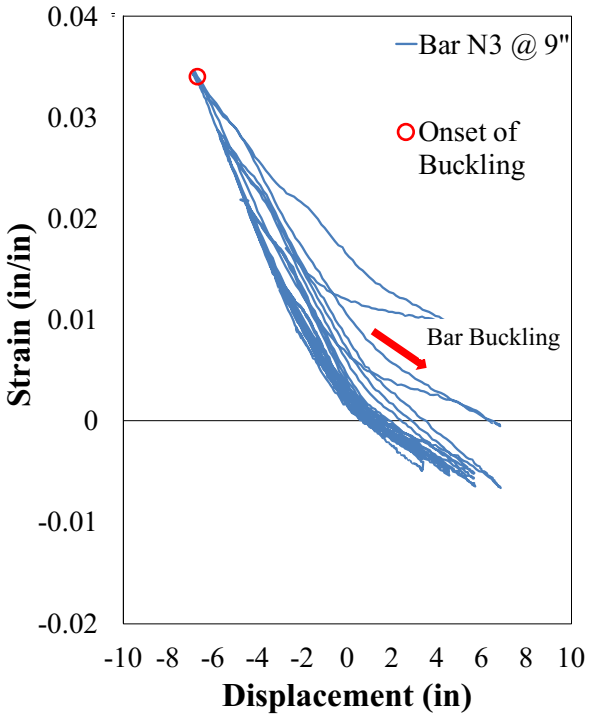


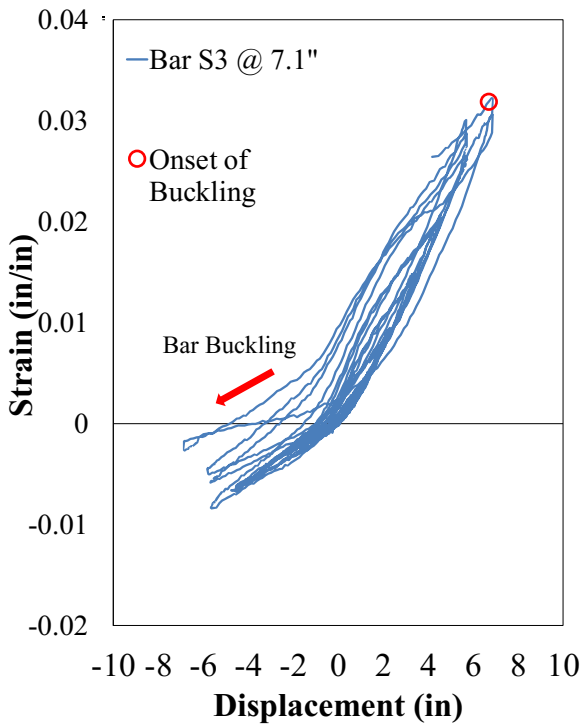

*Figure 4-43: Column test 3 strain profiles after yield: (a) bar N3; (b) bar S3*

The solid lines in Figure 4-43 represent positive tension strain, while the dashed lines depict negative compression strains. The North and South bars of the column had an approximate spread of plasticity of 24 and 23 inches from the top of footing, respectively.

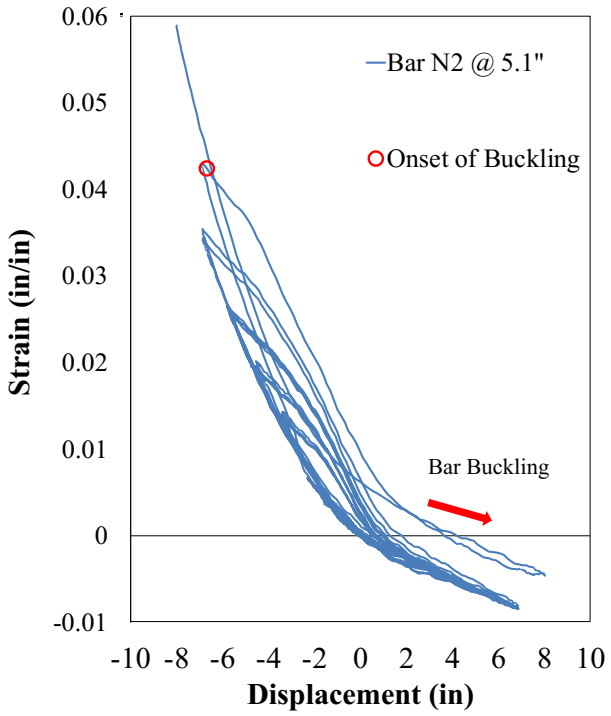
As discussed in Section 4.2.2, bar buckling can be observed by plotting strain versus column displacement, as seen in Figure 4-44.




(a)




(b)

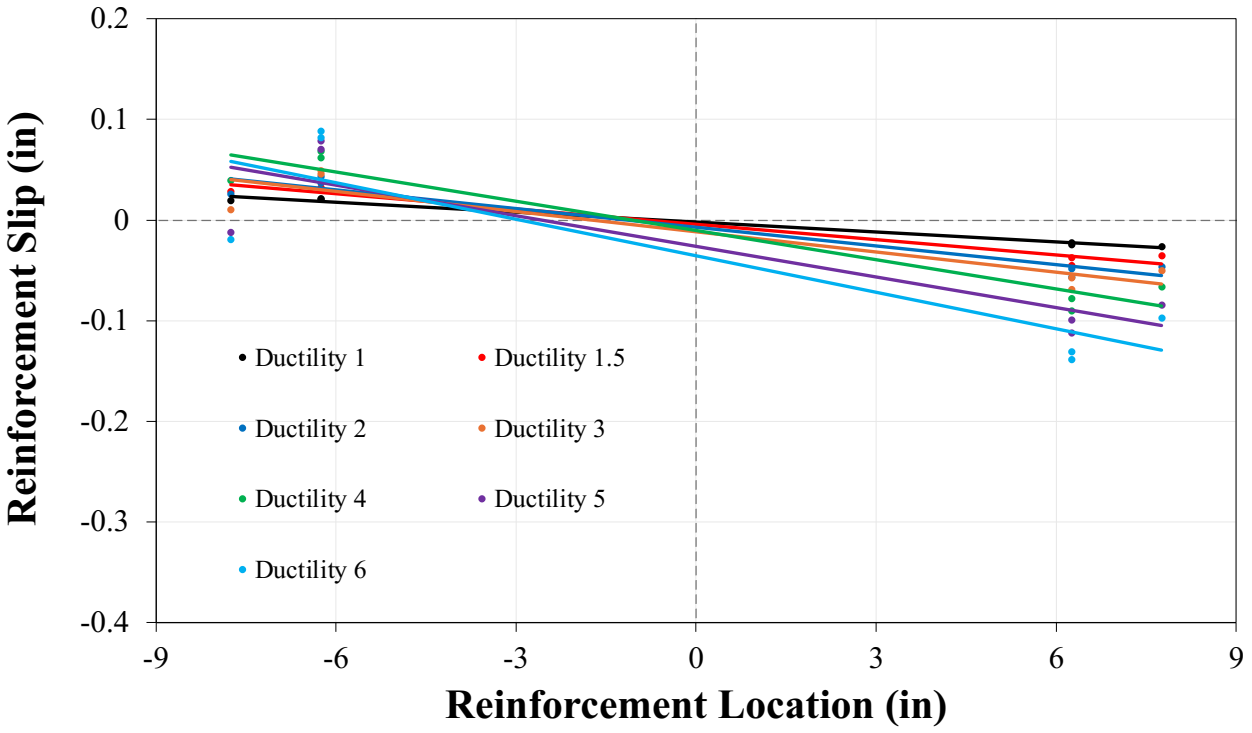



(c)

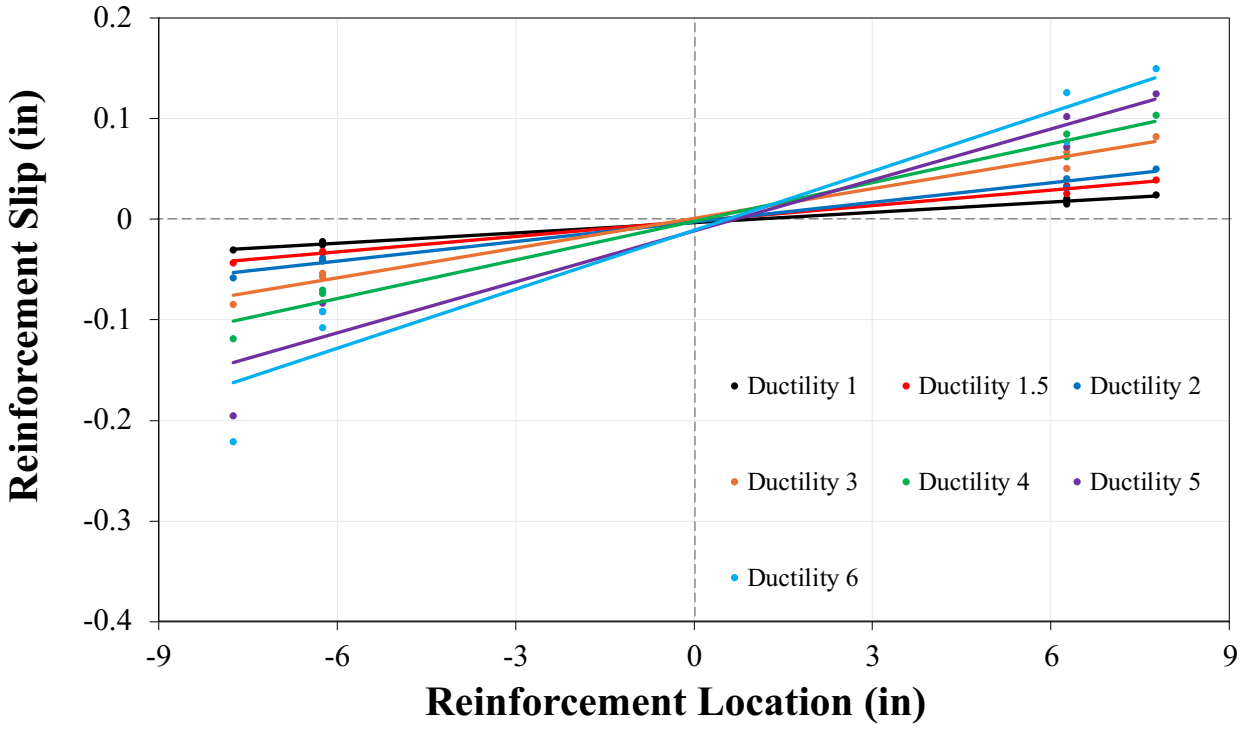
*Figure 4-44: Column test 3 strain vs. displacement: (a) bar N3; (b) bar S3; (c) bar N2*

### *4.4.3 Components of Displacement*

As discussed in Section 4.2.3, the two main components of column displacement are flexural deformation and rotation of the column due to bond slip, or strain penetration. Using the methods outlined in Section 4.2.3, flexural deformation and rotation of the column were calculated. Figure 4-45 shows the reinforcement slip of the column, and Figure 4-46 shows the curvature distribution over the instrumented height of the column from the first cycle of each ductility. The individual contributions of both flexural and rotational displacements compared to measured column displacement can be seen in Figure 4-47. As mentioned earlier, due to multiple LEDs falling off the reinforcing steel during ductility seven, the results for ductility test seven are not included.




(a)




(b)

*Figure 4-45: Column test 3 bond slip of extreme fiber bars: (a) south side under push cycles; (b) north side under pull cycles*

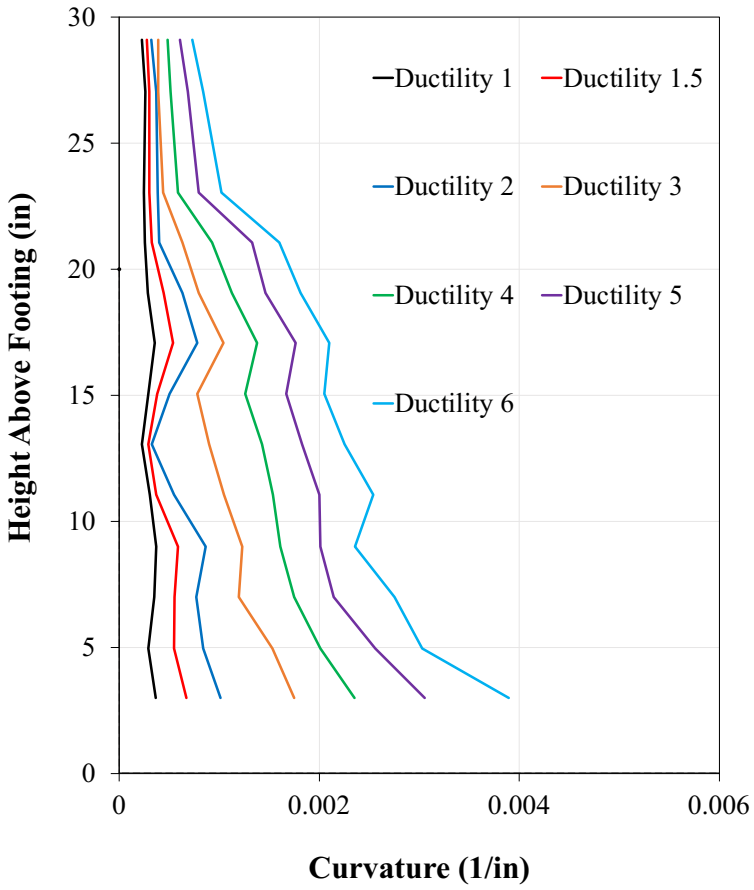



*Figure 4-46: Column test 3 curvature profile*

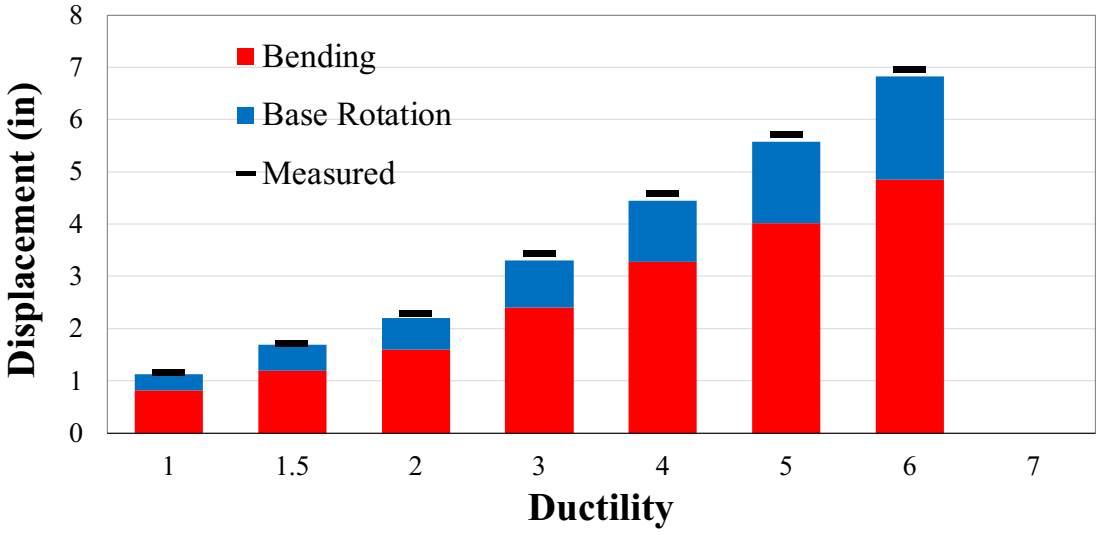



*Figure 4-47: Column test 3 components of displacement*

### *4.4.4 Hysteretic Energy Dissipation*

To determine the hysteretic damping of the columns, the area-based hysteretic damping (Jacobsen's damping), was calculated for the first cycle of each ductility. As described in Section 4.1.4, Jacobsen's hysteretic damping, Equation 4-1, was corrected using Equation 4-2. The hysteretic damping components of Jacobsen's Damping ($\xi_{hyst}$) and the corrected hysteretic damping ($\xi_{hyst,corr}$) were plotted for each ductility and can be seen in Figure 4-48. The hysteretic damping is directly proportional to the energy dissipated by the column.

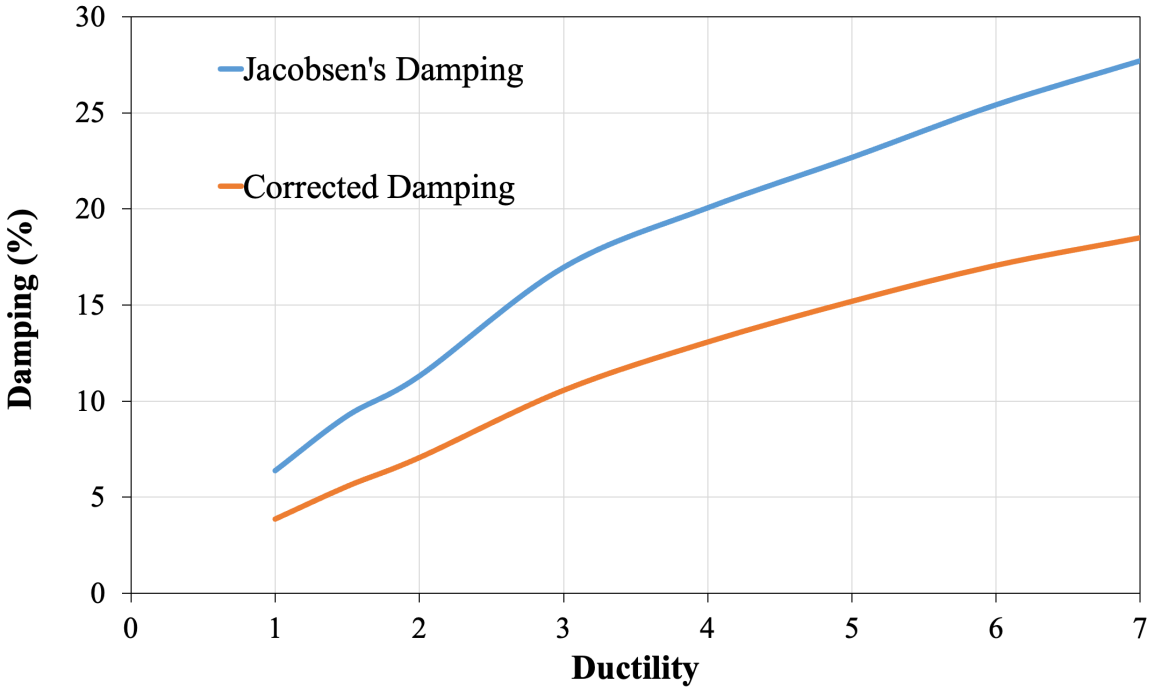



*Figure 4-48: Column test 3 hysteretic damping*

### *4.4.5 Strain Limit States*

As discussed in Section 4.2.5, strain histories of the longitudinal bars are crucial for identifying important damage limit states of the column such as concrete cracking, concrete crushing, bar buckling, and bar fracture. The strain at the damage limit states for Test 3 can be seen in Table 4-12. For concrete cracking and crushing, the maximum strain values were determined at the ductility level where the corresponding damage was observed. Concrete crushing was typically measured during compression cycles. For bar buckling, the strain values were found by plotting strain versus displacement as shown in Section 4.2.2. For bar buckling, the strain values

were determined by plotting strain versus displacement, as shown in Section 4.2.2. The reported buckling strain was the maximum tension strain observed before the bar buckled upon reversal, as illustrated in Figure 4-44.

*Table 4-12: Column test 3 strain at damage limit states*

| Damage State | Measured Strain (in/in) | |
|---|---|---|
| | North, N3 | South, S3 |
| Concrete Cracking | 0.0012 | 0.0010 |
| Concrete Crushing | 0.0075 | 0.0068 |
| Bar Buckling | 0.0340 | 0.0319 |

## 4.4 Column Test 4 Summary

Column Test 4 was conducted at the Constructed Facilities Laboratory on June 19th, 2024. The column featured 50% corrosion (defined by mass loss) in the plastic hinge. Table 4-13 summarizes column parameters and damage observations.

*Table 4-13: Column test 4 parameters and results summary*

**Load History**: Symmetric Three Cycle Quasi Static

**Column Parameters:**

| | |
|---|---|
| Corrosion Level: | 50% |
| Concrete Compressive Strength: | $f$c' = 6572 psi |
| Corroded Longitudinal Bars Strength: | fy = 42.4 ksi |
| Axial Load: | $P$ = 144 kips ($P$/($f$c'$A$g) = 10%) |
| Column Length and Aspect Ratio: | 8ft (L/D = 5.33) |
| Equivalent Yield Displacement: | $\Delta_y$ = 1.15" |
| Maximum Lateral Force: | 27.75 kips |
| Failure Mode: | Fracture of buckled longitudinal steel |

**Damage Observations:**

| | |
|---|---|
| First Cracking North: | -0.75$F_y$' = -0.58" |
| First Cracking South: | $F_y$'= 0.81" |
| Concrete Crushing North: | $\mu_3^{-3}$ = -3.43" |
| Concrete Crushing South: | $\mu_2^{+1}$ = 2.29" |
| Longitudinal Bar Fracture South; S3: | $\mu_3^{+3}$ = 3.43" |
| Longitudinal Bar Buckling North; N3: | $\mu_5^{+3}$ = 5.72" |
| Longitudinal Bar Fracture North; N3: | $\mu_5^{-3}$ = -5.72" |
| Longitudinal Bar Fracture South; S2: | $\mu_6^{+1}$ = 6.87" |
| Longitudinal Bar Buckling North; N2: | $\mu_6^{+2}$ = 6.96" |
| Longitudinal Bar Fracture North; N2: | $\mu_6^{-2}$ = -6.86" |

Material tests were performed on the reinforcing steel (uncorroded and corroded) and the concrete used in the column. Figure 4-49 shows the stress-strain responses of the uncorroded and corroded steel specimens, and Table 4-14 summarizes the results. For the corroded specimen, a rebar specimen identical to the longitudinal bars used in the column construction was corroded to

the same level of corrosion as the column. Compression tests were performed on concrete samples on the day of the test. The results are summarized in Table 4-15.

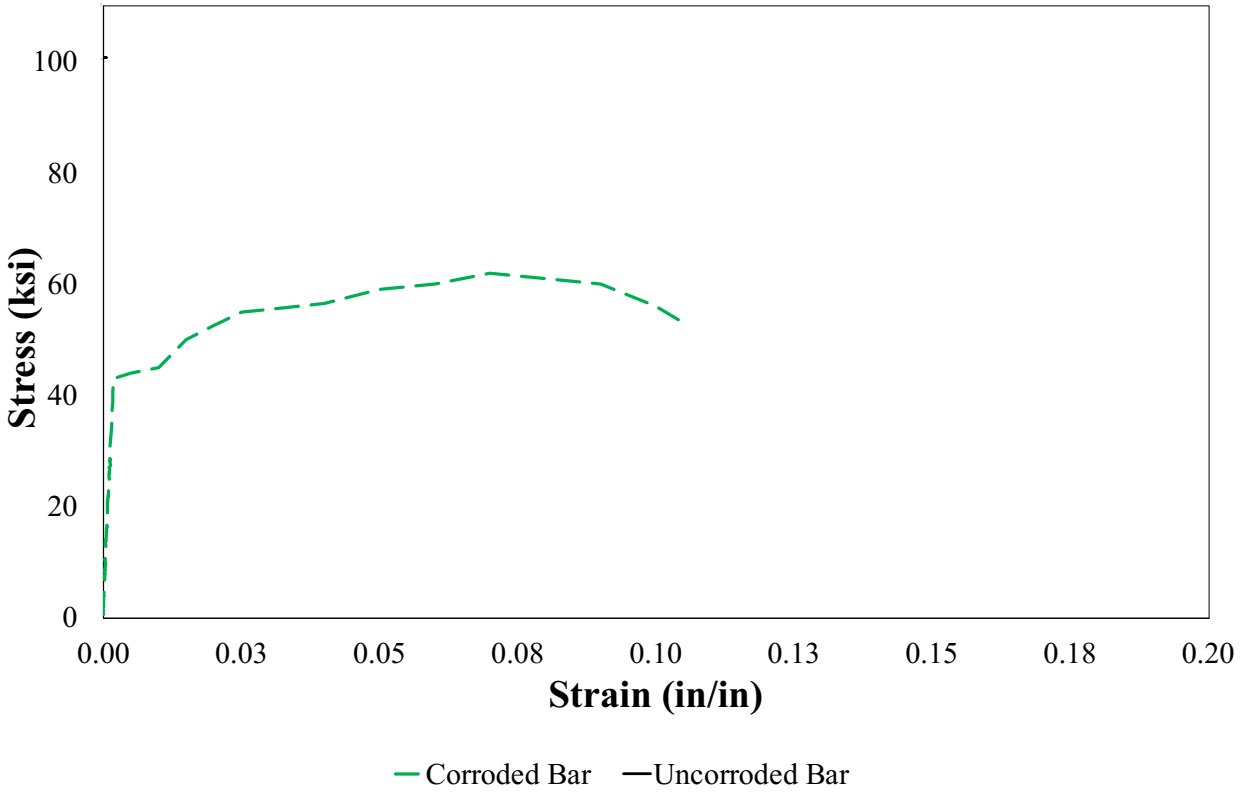



*Figure 4-49: Column test 4 stress-strain response material tests*

*Table 4-14: Column test 4 material tension test results*

| Steel | Yield Stress (ksi) | Yield Strain (%) | Maximum Stress (ksi) | Strain at Maximum Stress (%) |
|---|---|---|---|---|
| Uncorroded bar | 68.5 | 0.22 | 100.2 | 11.6 |
| Corroded bar N3 | 42.4 | 0.11 | 62.4 | 7.3 |

*Table 4-15: Column test 4 concrete compression strength results*

| Column Concrete | | Footing Concrete | |
|---|---|---|---|
| **Cylinder** | **Stress (psi)** | **Cylinder** | **Stress (psi)** |
| 1 | 6493 | 1 | 4395 |
| 2 | 6471 | 2 | 4257 |
| 3 | 6753 | 3 | 4530 |
| **Average** | 6572 | **Average** | 4394 |

During the test, cracks and damage states in the column were marked and recorded between half cycles. Cracks on the South side of the column were denoted with red marks, whereas those on the North side were marked with black. The test concluded during the second cycle of ductility six, after four bars had fractured and the maximum force dropped by over 50%. The force-displacement response is shown in Figure 4-50, while the load history is presented in Figure 4-51.

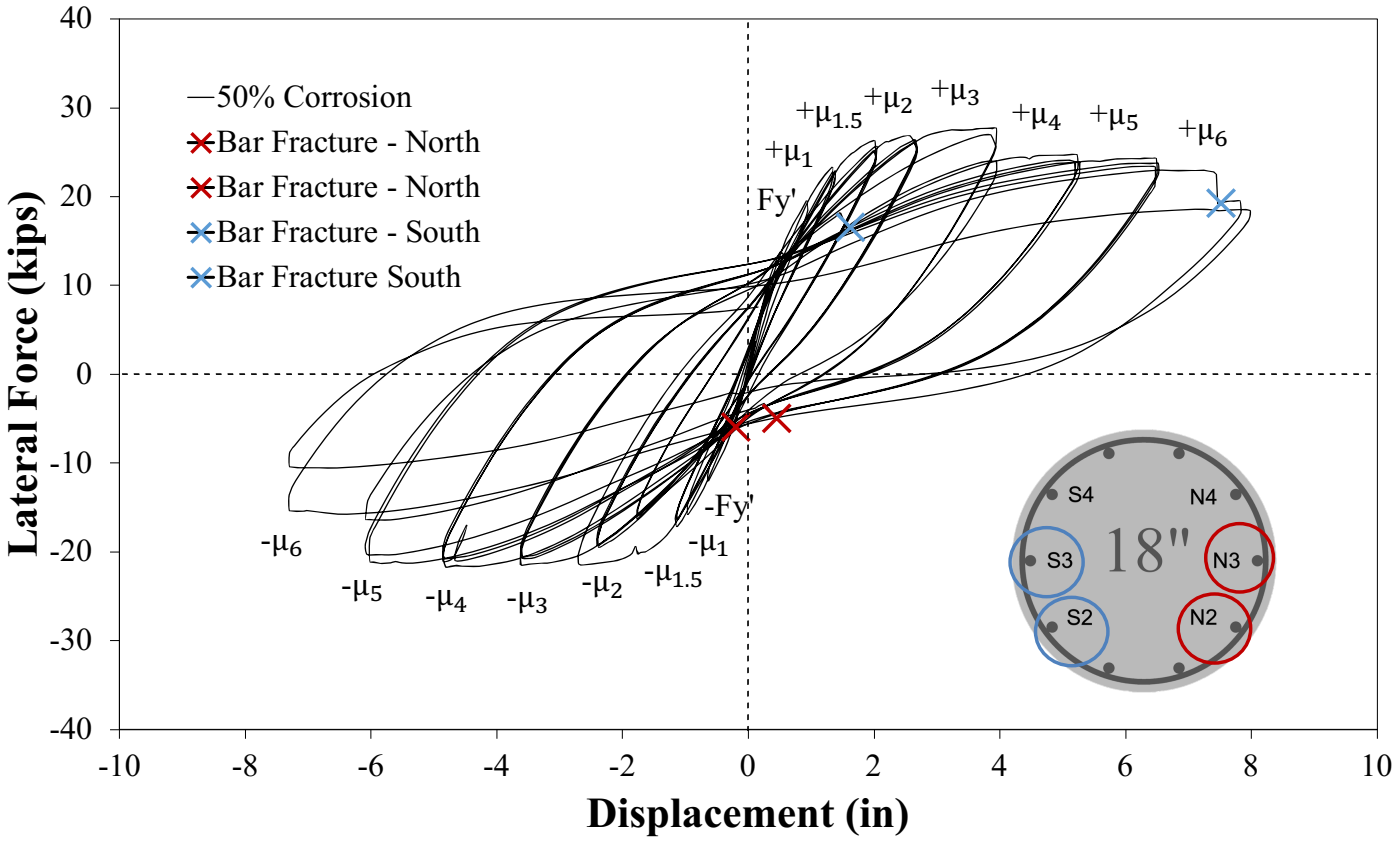



*Figure 4-50: Column test 4 force-displacement response*

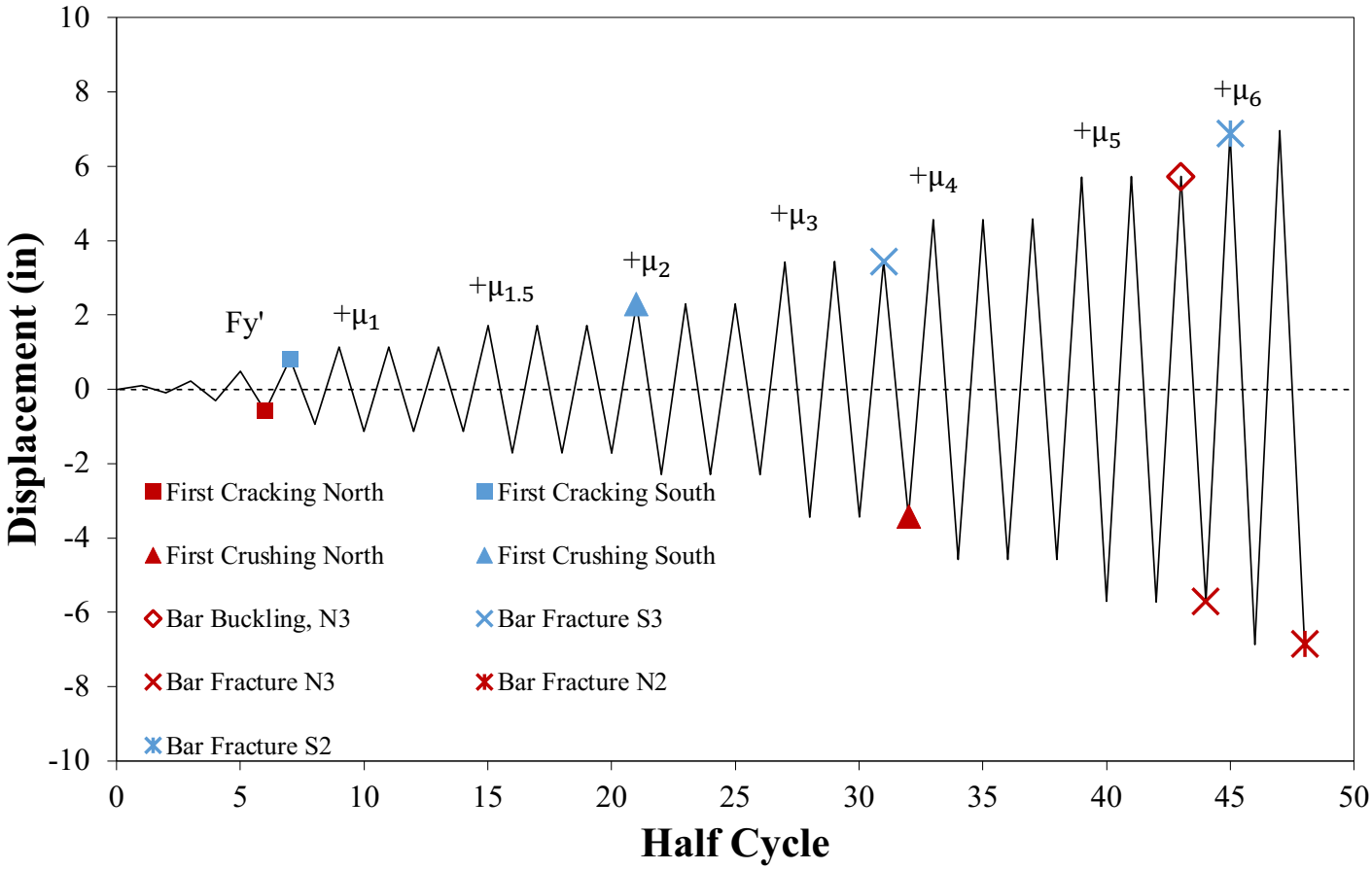



*Figure 4-51: Column test 4 load history*

### *4.3.1 Damage Progression*

Hairline cracks were observed on the North side of the column during the pull cycle of three quarters of first yield force ($-\frac{3}{4}F_y{}' = -11.91\ kips$). The cracks were located between N3 and N4 and near spirals approximately 15 inches above top of footing. During the push cycle of first yield force ($F_y{}' = 19.77\ kips$), cracks were observed on the South side between S2 and S3 approximately 8 inches above top of footing. During ductility one, more hairline cracks developed close to the extreme longitudinal bars and near the base of the column. The crack distribution at the end of ductility one can be seen in Figure 4-52. During ductility 1.5 multiple flexural cracks were observed between extreme longitudinal bars. The cracks measured approximately 0.25mm in width. Throughout ductility two, previous cracks observed during ductility 1.5 expanded up to 1.5mm in width and flacking was observed at the base of the column near N2 and N3. The crack distribution at the end of ductility two can be seen in Figure 4-53. During the first half cycle of

ductility three ($\mu_3{}^{+1} = 3.43$ inches), concrete crushing was observed between S2 and S3 approximately 6 inches above top of footing as seen in Figure 4-54. During the fifth half cycle of ductility three ($\mu_3{}^{+3} = 3.43$ inches), bar S3 fractured unexpectedly. The fracture occurred approximately 5.5 inches above top of footing and behind the transverse steel as seen in Figure 4-55.

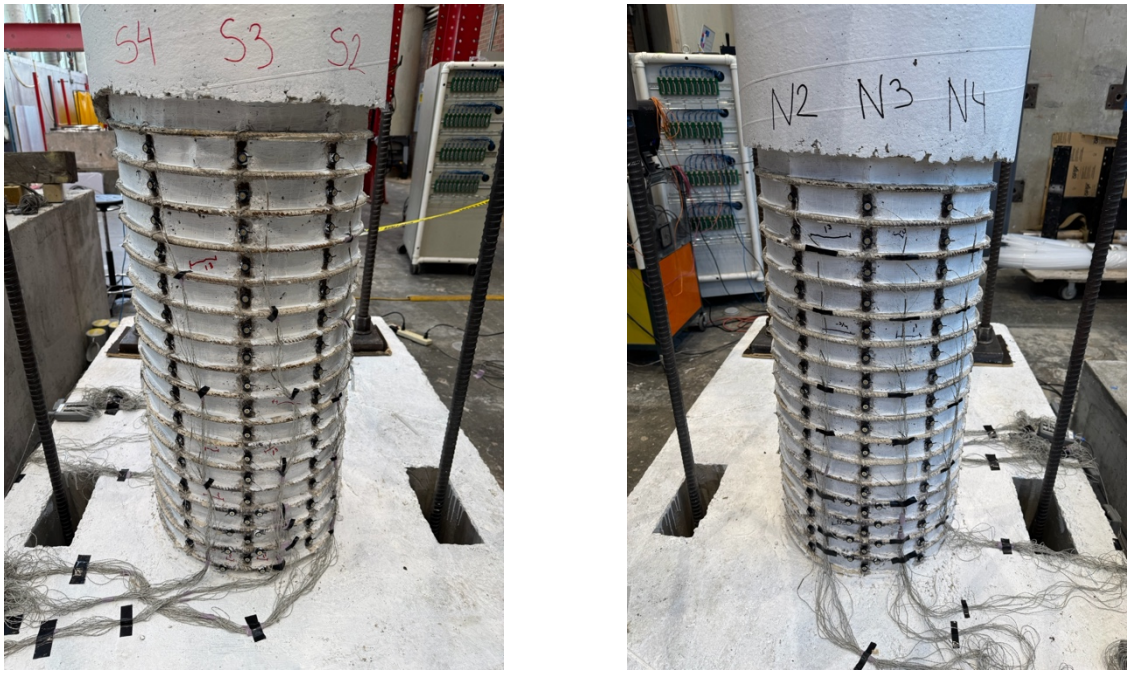



*Figure 4-52: Column test 4 crack distribution end of ductility one: (left) south side; (right) north side*




*Figure 4-53: Column test 4 crack distribution end of ductility two: (left) south side; (right) north side*



*Figure 4-54: Column test 4 crushing of concrete ductility three - south side*



*Figure 4-55: Column test 4 fractured bar during ductility three – bar S3*

During ductility four more crushing of the concrete core near the extreme longitudinal bars was observed, particularly around fracture bar S3. The North extreme fiber bar N3 buckled near the base of the column during the fifth half cycle of ductility five ($\mu_5{}^{+3} = 5.71"$ inches), as seen in Figure 4-56. During the next half cycle ($\mu_5{}^{-3} = -5.72$ inches), bar N3 fractured as seen in Figure 4-57. During the first half cycle of ductility six ($\mu_6{}^{+1} = 6.86$ inches), bar S2 fractured unexpectedly at the interface between the column and footing seen in Figure 4-58. During the fourth half cycle of ductility six ($\mu_6{}^{-2} = -6.86$ inches), bar N2 fractured unexpectedly around 6 inches above top of footing as seen in Figure 4-59. The test concluded following the fracture of N2, after three bars had fractured and the maximum force dropped over 50%.



*Figure 4-56: Column test 4 buckling during ductility five – bar N3*



*Figure 4-57: Column test 4 fractured bar ductility six – bar N3*



*Figure 4-58: Column test 4 fractured bar ductility six – bar S2*



*Figure 4-59: Column test 4 fractured bar ductility six – bar N2*

### *4.3.2 Strain Analysis*

As illustrated in Section 4.2.2, to determine strains in the longitudinal and transverse steel, position data from the Optotrak LED markers was analyzed and strains were calculated using Equation 4-3 and Equation 4-4. Strain profiles of the extreme North and South bars, N3 and S3, for the first cycle of each ductility following yield, are shown in Figure 4-60. As a result of multiple LEDs falling off the reinforcing steel during ductility five and six due to bar fracture, the results following ductility five for the North side, and the results following ductility four for the South side, are not included.

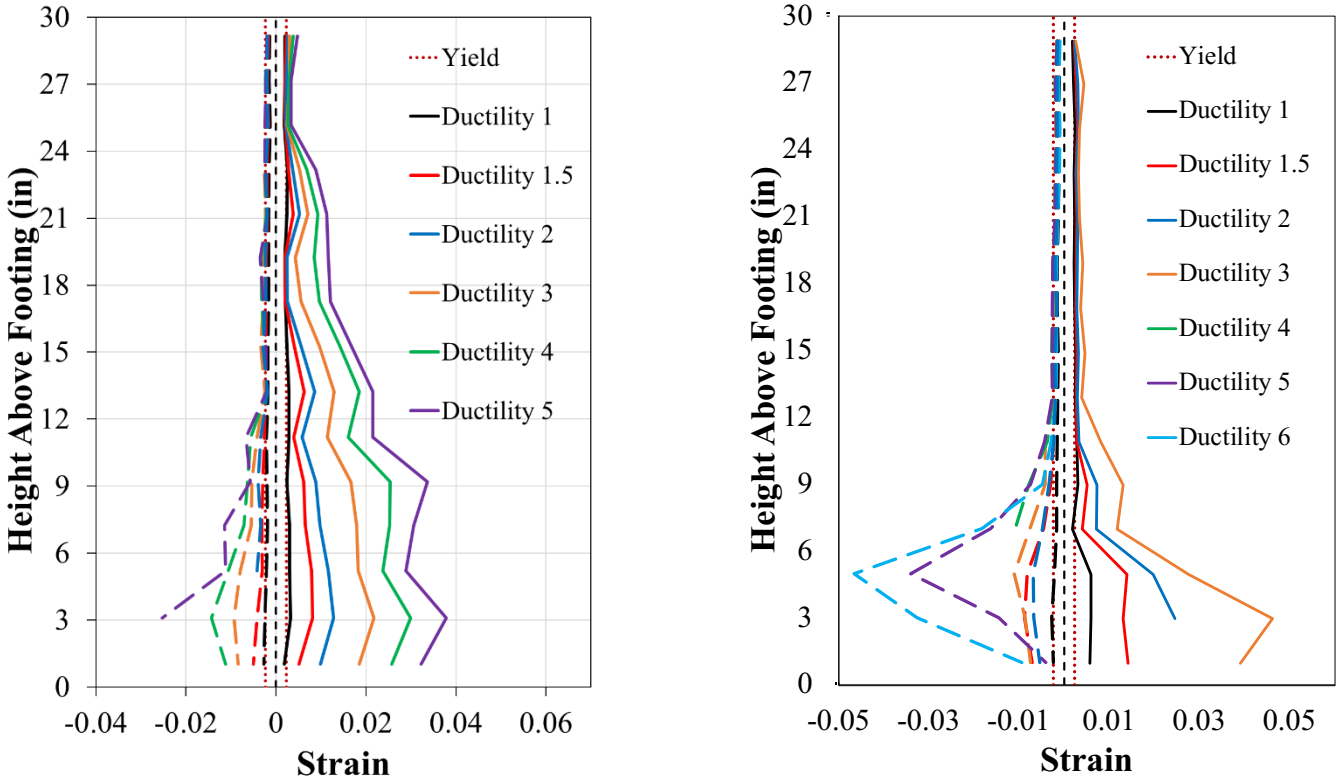



*Figure 4-60: Column test 4 strain profiles after yield: (a) bar N3; (b) bar S3*

The solid lines in Figure 4-60 represent positive tension strain, while the dashed lines depict negative compression strains. The North and South bars of the column had an approximate spread of plasticity of 25 and 13 inches from the top of footing, respectively.

As discussed in Section 4.2.2, bar buckling can be observed by plotting strain versus column displacement, as seen in Figure 4-61.

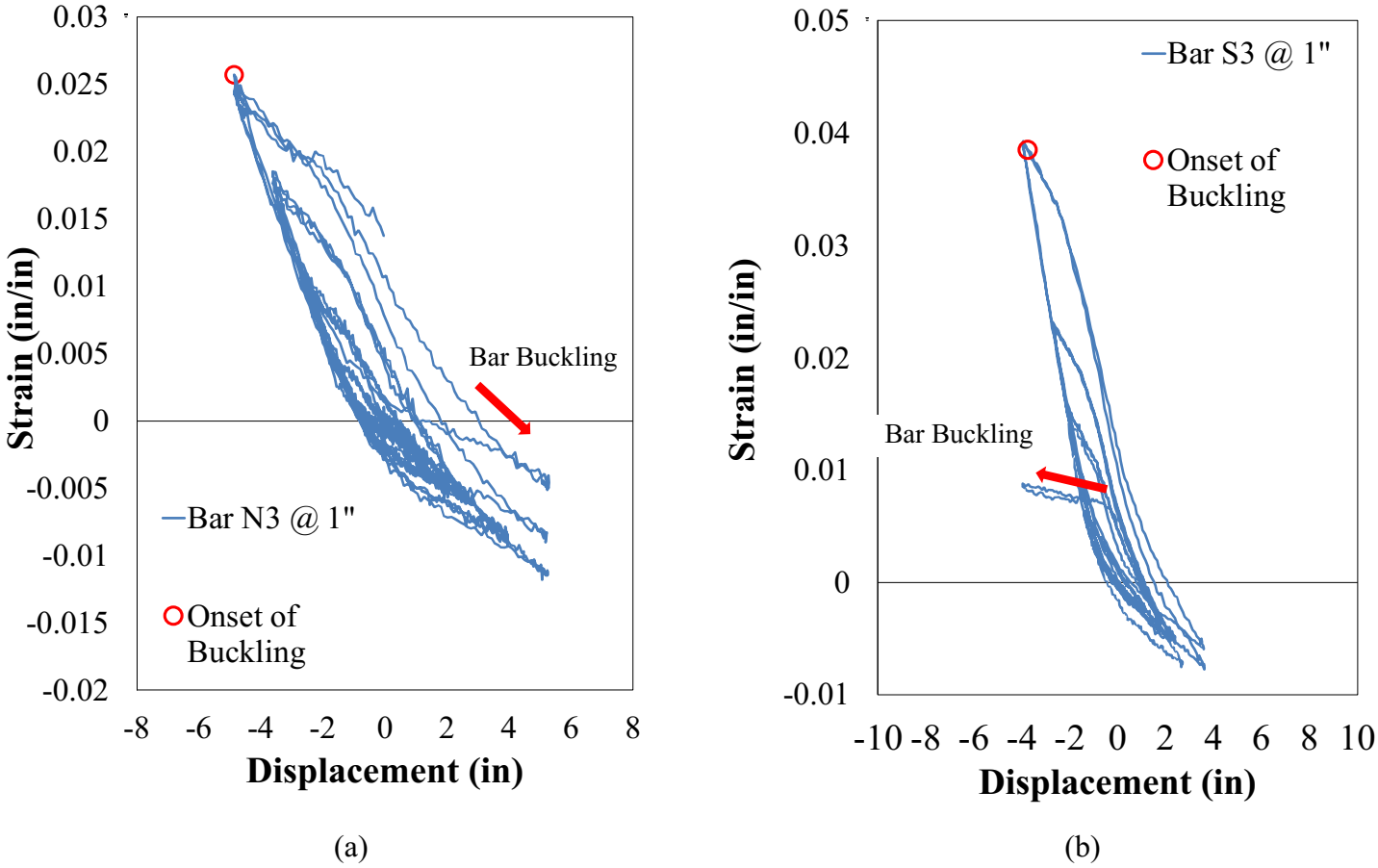
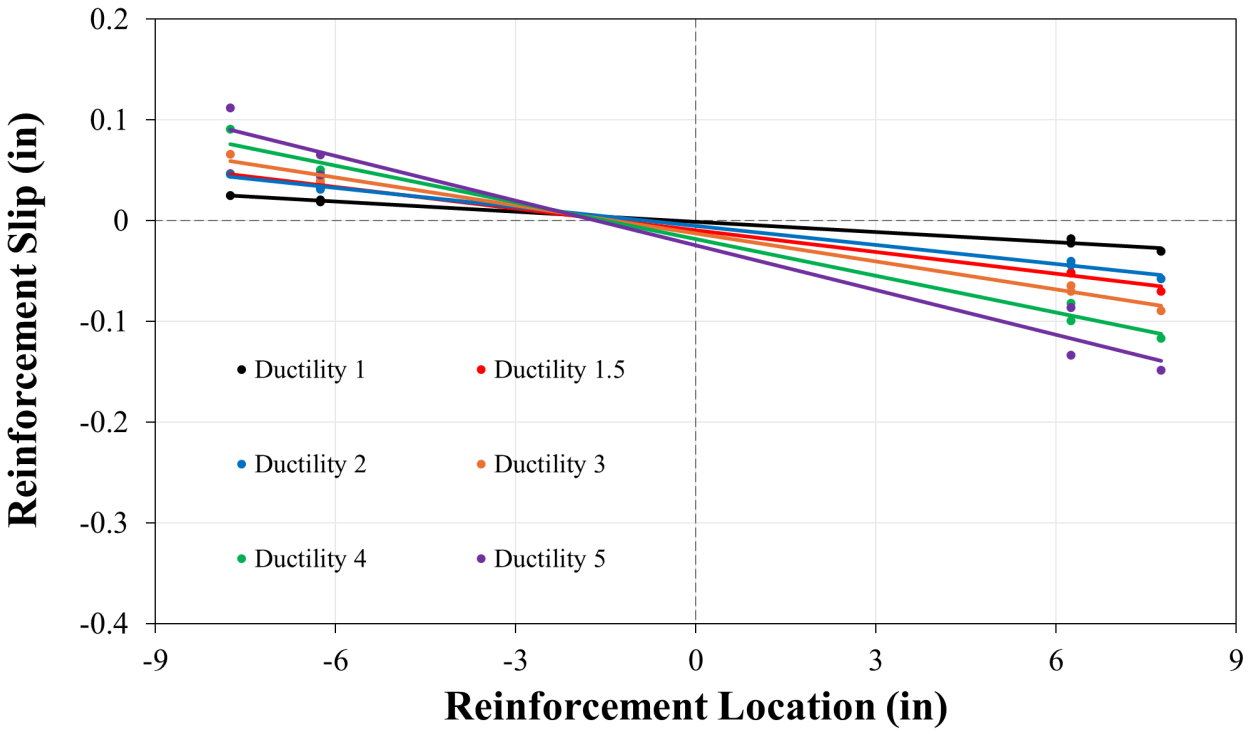


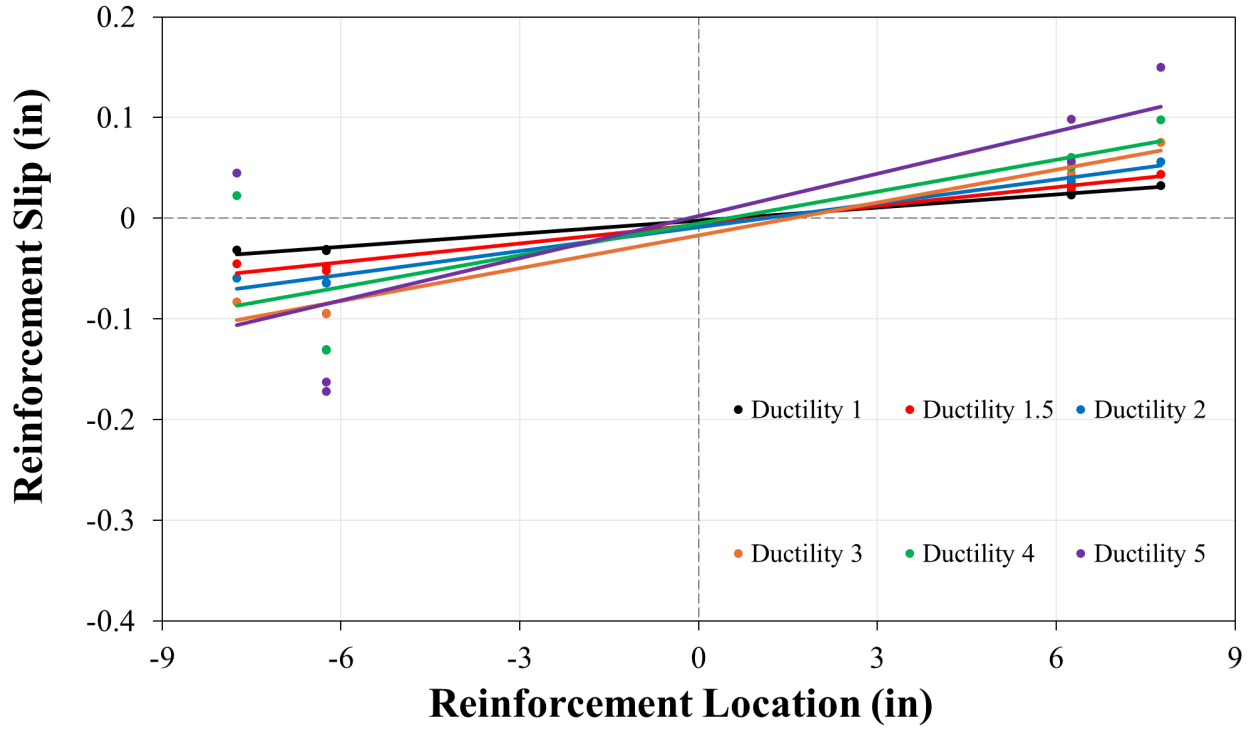

*Figure 4-61: Column test 4 strain vs. displacement: (a) bar N3; (b) bar S3*

### *4.3.3 Components of Displacement*

As summarized in Section 4.2.3, the two main components of column displacement are flexural deformation and rotation of the column due to bond slip, or strain penetration. Using the methods outlined in Section 4.2.3, flexural deformation and rotation of the column were calculated. Figure 4-62 shows the reinforcement slip of the column, and Figure 4-63 shows the curvature distribution over the instrumented height of the column from the first cycle of each ductility. The individual contributions of both flexural and rotational displacements compared to measured column displacement can be seen in Figure 4-64. As mentioned earlier, due to multiple LEDs falling off the reinforcing steel during ductility six, the results following ductility five are not included.




(a)




(b)

*Figure 4-62: Column test 4 bond slip of extreme fiber bars: (a) south side under push cycles; (b) north side under pull cycles*

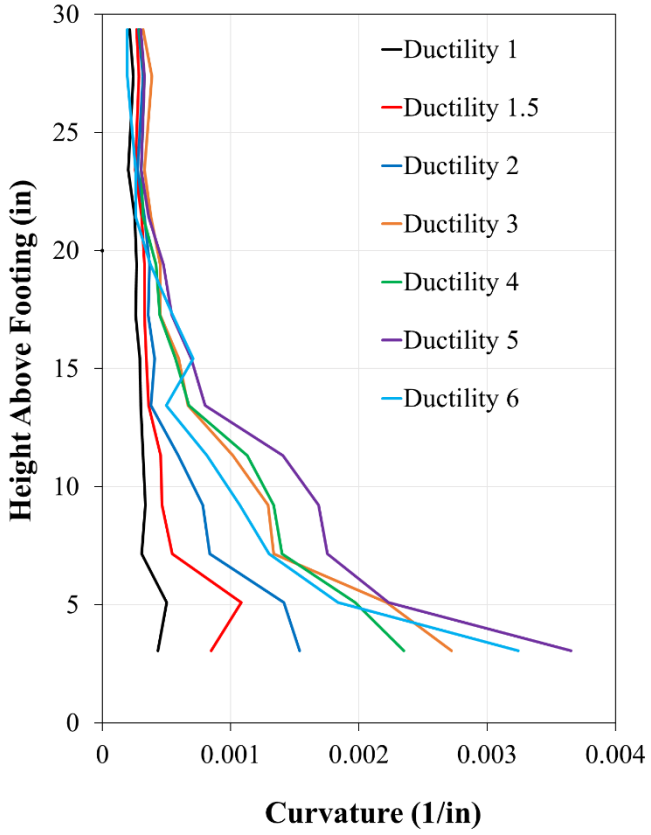



*Figure 4-63: Column test 4 curvature profile*

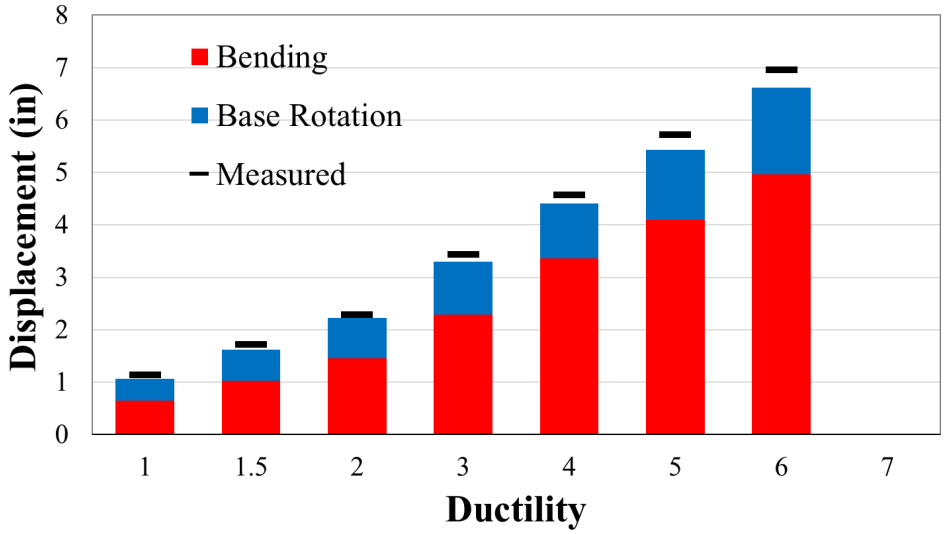



*Figure 4-64: Column test 4 components of displacement*

### *4.3.4 Hysteretic Energy Dissipation*

To determine the hysteretic damping of the columns, the area-based hysteretic damping (Jacobsen's damping), was calculated for the first cycle of each ductility. As described in Section 4.1.4, Jacobsen's hysteretic damping, Equation 4-1, was corrected using Equation 4-2. The hysteretic damping components of Jacobsen's Damping ($\xi_{hyst}$) and the corrected hysteretic damping ($\xi_{hyst,corr}$) were plotted for each ductility and can be seen in Figure 4-65. The hysteretic damping is directly proportional to the energy dissipated by the column.

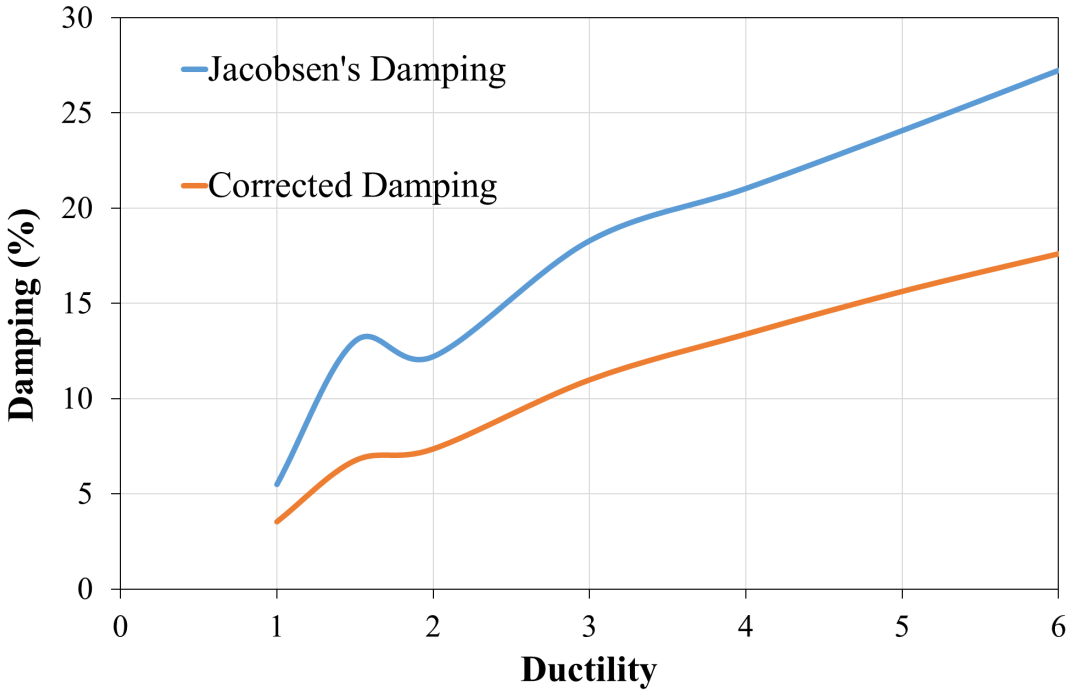



*Figure 4-65: Column test 4 hysteretic damping*

### *4.3.5 Strain Limit States*

As illustrated in Section 4.2.5, strain histories of the longitudinal bars are crucial for identifying important damage limit states of the column such as concrete cracking, concrete crushing, bar buckling, and bar fracture. The strain at the damage limit states for Test 4 can be seen in Table 4-16. For bar buckling, the strain values were determined by plotting strain versus displacement, as shown in Section 4.2.2. The reported buckling strain was the maximum tension strain observed before the bar buckled upon reversal, as illustrated in Figure 4-61.

For concrete cracking and crushing, the maximum strain values were determined at the ductility level where the corresponding damage was observed. Concrete crushing was typically

measured during compression cycles. For bar buckling, the strain values were determined by plotting strain versus displacement, as shown in Section 4.2.2. The reported buckling strain was the maximum tension strain observed before the bar buckled upon reversal, as illustrated in Figure 4-61.

*Table 4-16: Column test 4 strain at damage limit states*

| Damage State | Measured Strain (in/in) | |
|---|---|---|
| | North, N3 | South, S3 |
| Concrete Cracking | 0.00063 | 0.0021 |
| Concrete Crushing | 0.01 | 0.0068 |
| Bar Buckling | 0.0257 | 0.0385 |

# CHAPTER 5: MATERIAL LEVEL CHARACTERIZATION

## 5.1 Tension Tests

### *5.1.1 Tension Test Procedure*

Tension tests were performed on rebar specimens with corrosion levels ranging from 0-50%. The corrosion levels matched those used in the large-scale tests. To perform the tension tests, rebar specimens were loaded into a universal testing machine (UTM) and pulled in tension until fracture. The rebar specimens were instrumented with LED markers that were tracked with a 3D measurement system. The position data allowed for the calculation of strains in the specimen as discussed in Section 3.2.2. The UTM provided force data.

### *5.1.2 Tension Test Results*

A total of six additional tension tests were performed with corrosion levels ranging from 0% to 50%.

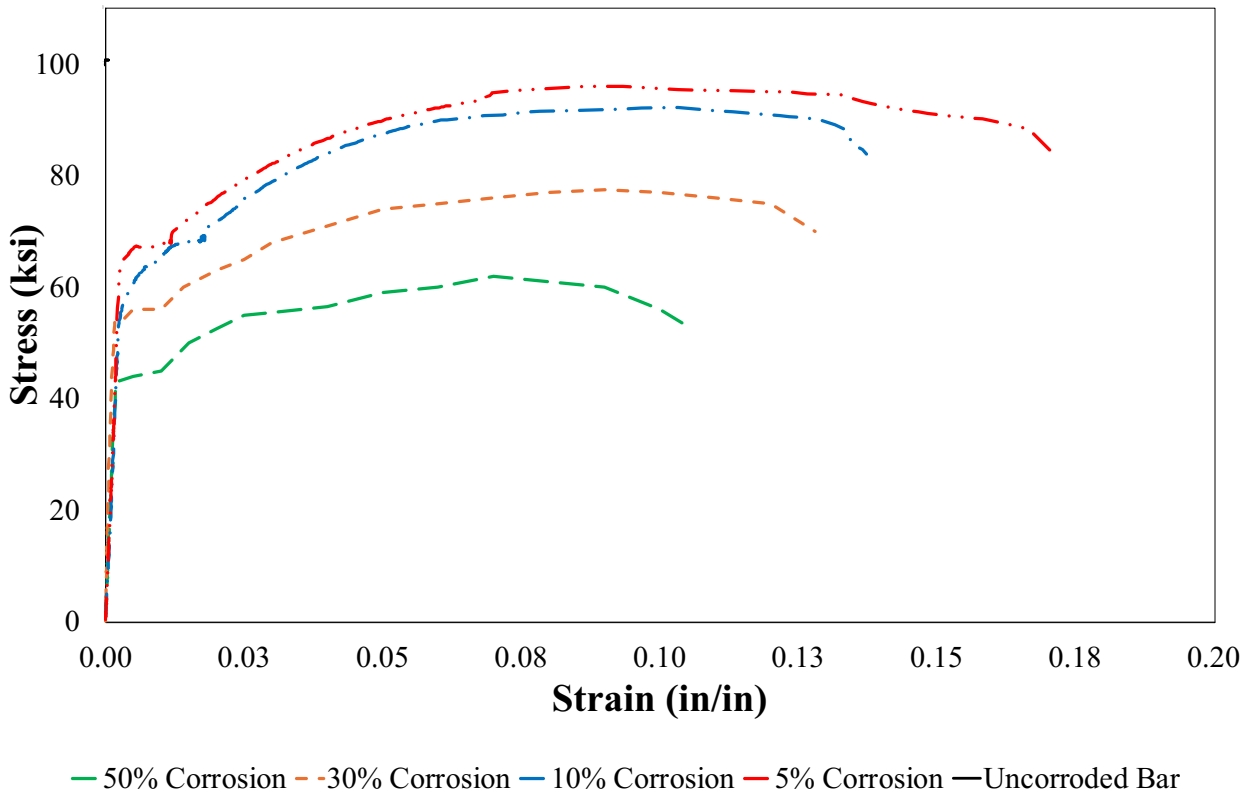



*Figure 5-1: Tension test results – stress vs. strain at different corrosion levels*

## 5.2 Buckled Bar Tension Tests

### *5.2.1 Buckled Bar Tension Test Procedure*

The Buckled Bar Tension (BBT) test is a material test that was developed at North Carolina State University by Barcley and Kowalsky (2019). The aim of the BBT test is to investigate the post-buckling behavior of reinforcing steel by replicating the tension and compression loads that the steel experiences in a column during cyclic loading.

During a BBT test, a rebar specimen is instrumented with LED markers that are tracked with a 3D measurement system, as discussed in Section 3.2.2. The specimen is placed into a universal testing machine (UTM) and loaded in compression to a specific buckled curvature, then pulled in tension until fracture. The loading sequence of a BBT test can be seen in Figure 5-2.

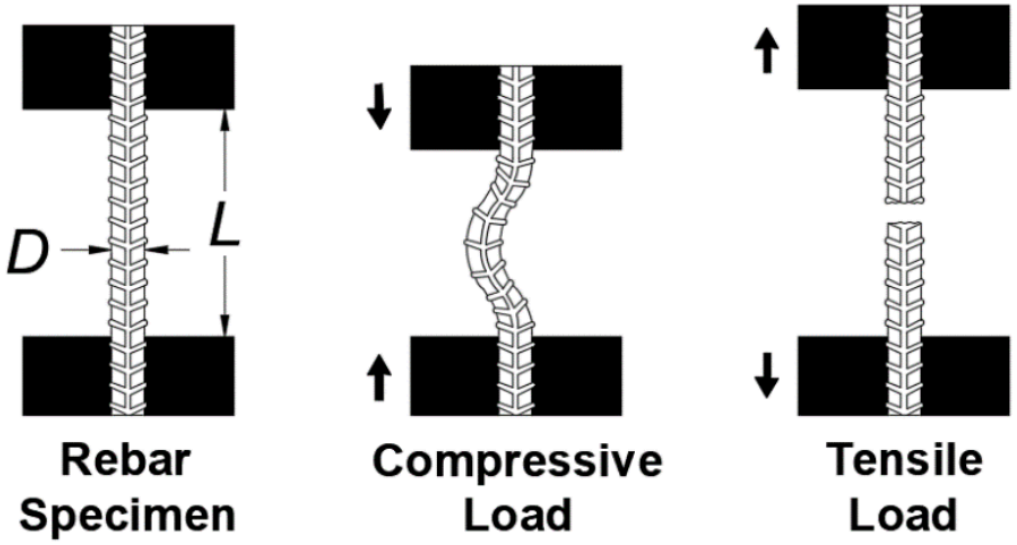
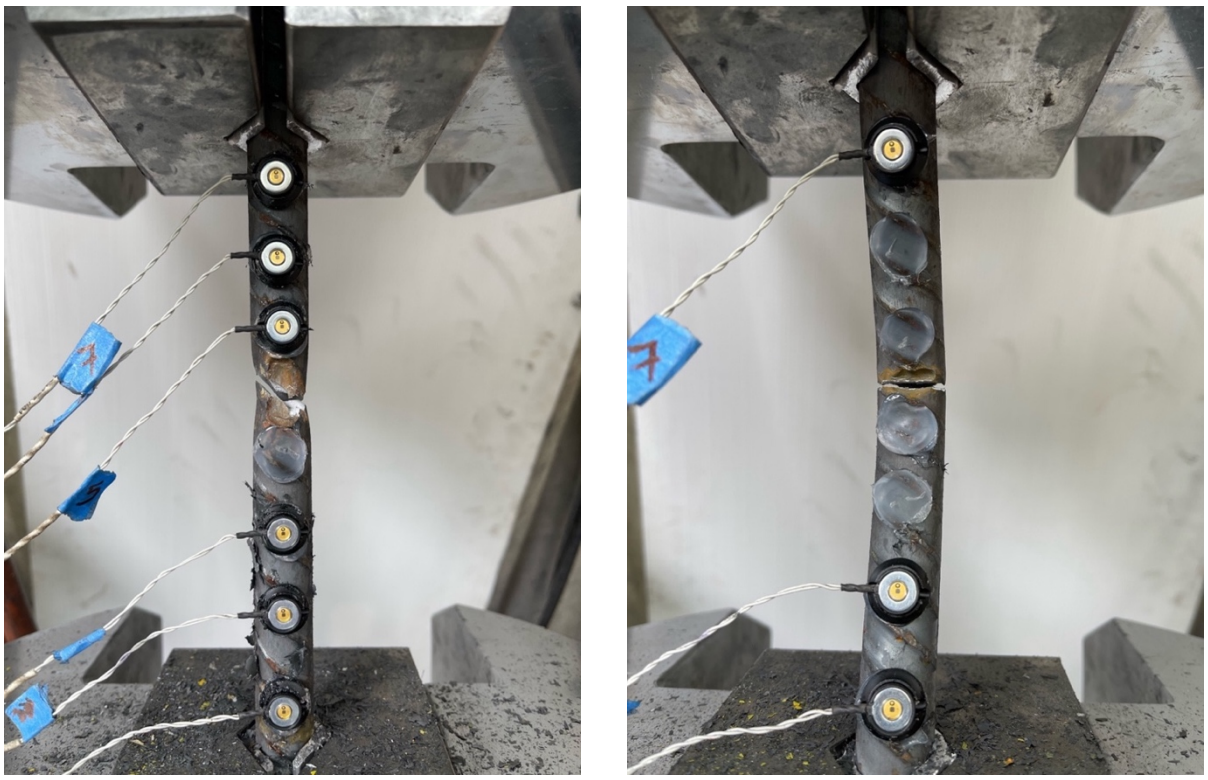



*Figure 5-2: BBT test sequence. Barcley and Kowalsky (2019)*

Depending on the level of curvature, the rebar specimen will experience either a ductile or brittle failure. During a ductile failure, necking and elongation is observed in the specimen during the tension phase of the test, while brittle failures experience little to no elongation and often sudden and unexpected failure. Examples of ductile and brittle failures can be seen in Figure 5-3. The test determines the critical bending strain of buckled reinforcing steel. The critical bending strain is the point where the uniform elongation decreases, leading to a brittle fracture.



(a) (b)

*Figure 5-3: BBT failure types: (a) ductile failure; (b) brittle failure*

As mentioned earlier, LED markers were attached to the rebar specimens to track their position throughout the BBT test. Using a fourth order polynomial, the displaced shape of the bar could be approximated. Because the LEDs were attached to the surface of the specimen, the displaced shape was then corrected to specimen's neutral axis (NA). To calculate the specimen's curvature, φ, Euler-Bernoulli beam theory was utilized. The curvature was calculated as the second derivative of the displaced shape, *w*, as show in Equation 5-1. Because at maximum curvature the displacements are at a minimum, the curvature can be approximated as the second derivative of position, as shown in Equation 5-2. Maximum bending strain, $e_b$, would then be calculated by multiplying curvature by half the rebar specimen diameter as seen in Equation 5-3. In addition, the buckled reinforcing steel reaches a critical bending strain, $e_{cr}$ , at the transition between ductile and brittle failure. A previous study done by Barcley and Kowalsky (2019), found that there is a strong correlation between the critical bending strain, $e_{cr}$, found in the BBT tests and large-scale tests.

$$\varphi = \frac{\frac{d^2w}{dx^2}}{\left[1 + \left(\frac{dw}{dx}\right)^2\right]^{3/2}}$$ *Equation 5-1*

$$\varphi \approx \frac{d^2w(x)}{dx^2}$$ *Equation 5-2*

$$e_b = \varphi \frac{d_b}{2}$$ *Equation 5-3*

### *5.2.2 BBT Test Results*

A total of 25 BBT tests were performed with corrosion levels ranging from 0% to 50%. For each corrosion level a total of 6 BBT tests were performed. The testing matrix can be seen in Table 5-1. The rebar specimens were identified using the format outline below:

BBT - CL (corrosion level) – (ID number)

*Table 5-1: BBT test matrix*

| Target Corrosion Level | Specimen Label |
|---|---|
| 5% | BBT-CL5-1 |
| | BBT-CL5-2 |
| | BBT-CL5-3 |
| | BBT-CL5-4 |
| | BBT-CL5-5 |
| | BBT-CL5-6 |
| 10% | BBT-CL10-1 |
| | BBT-CL10-2 |
| | BBT-CL10-3 |
| | BBT-CL10-4 |
| | BBT-CL10-5 |
| | BBT-CL10-6 |
| 30% | BBT-CL30-1 |
| | BBT-CL30-2 |
| | BBT-CL30-3 |
| | BBT-CL30-4 |
| | BBT-CL30-5 |
| | BBT-CL30-6 |

| | |
|---|---|
| 50% | BBT-CL50-1 |
| | BBT-CL50-2 |
| | BBT-CL50-3 |
| | BBT-CL50-4 |
| | BBT-CL50-5 |
| | BBT-CL50-6 |

The results from the BBT tests can be seen in Figure 5-4. For each test, bending strain was plotted versus uniform axial elongation, along with the critical bending strain at each corrosion level. The data for the uncorroded steel (corrosion level 0%) was taken from previous research conducted at NC State by Barcley and Kowalsky (2019). For the complete results, see Appendix D.

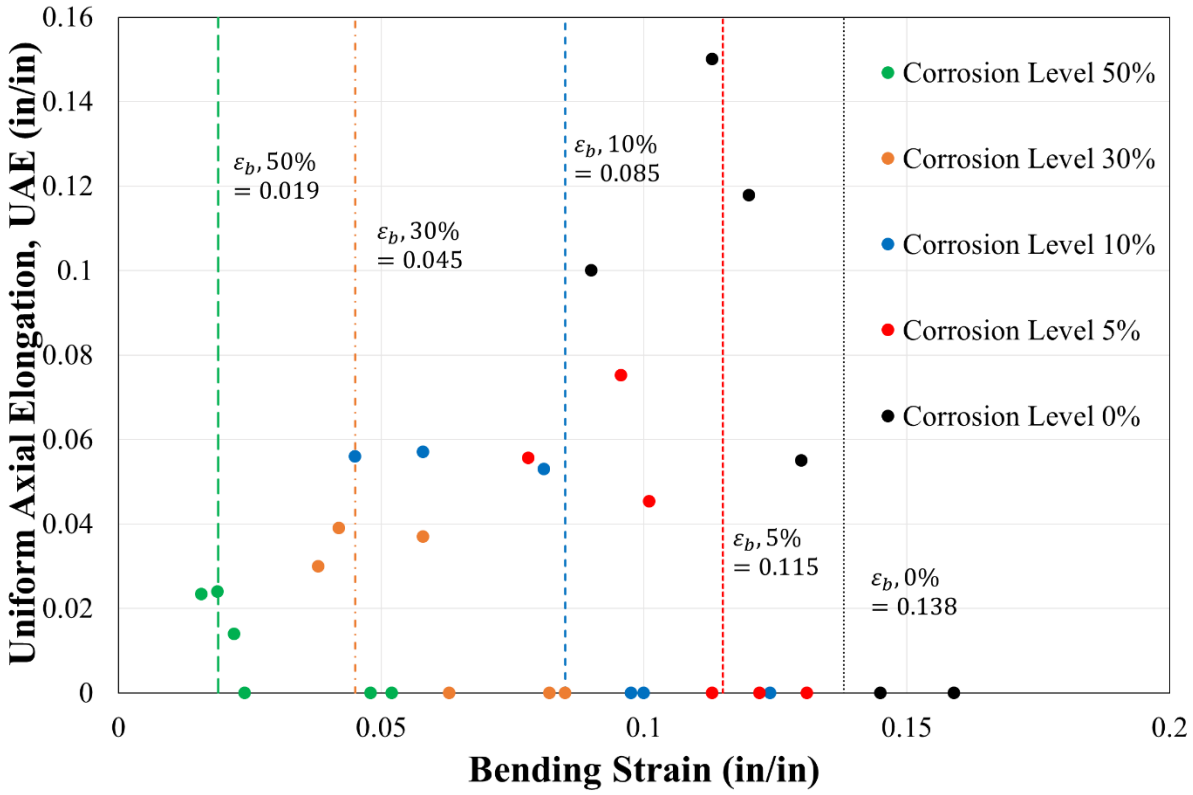



*Figure 5-4: BBT results – bending strain at different corrosion levels*

As Figure 5-4 shows, with increasing levels of corrosion, the critical bending strain reduces. This implies that corroded rebar will fracture at lower levels of bending strain, which is likely to reduce deformation capacity on the structural level.

## 5.3 Three-Dimensional Scanning of Corroded Bars

To analyze and mathematically quantify the surface of the corroded longitudinal bars and the material test specimens, a portable 3D scanner, the CR-Scan Ferret, was utilized. The 3D scanner, shown in Figure 5-5, captured the corroded surfaces with an accuracy of up to 0.1mm. The 3D scans were into mathematical mesh surfaces, where empirical data such as mass loss, corrosion pit depth and dimeter could be measured.

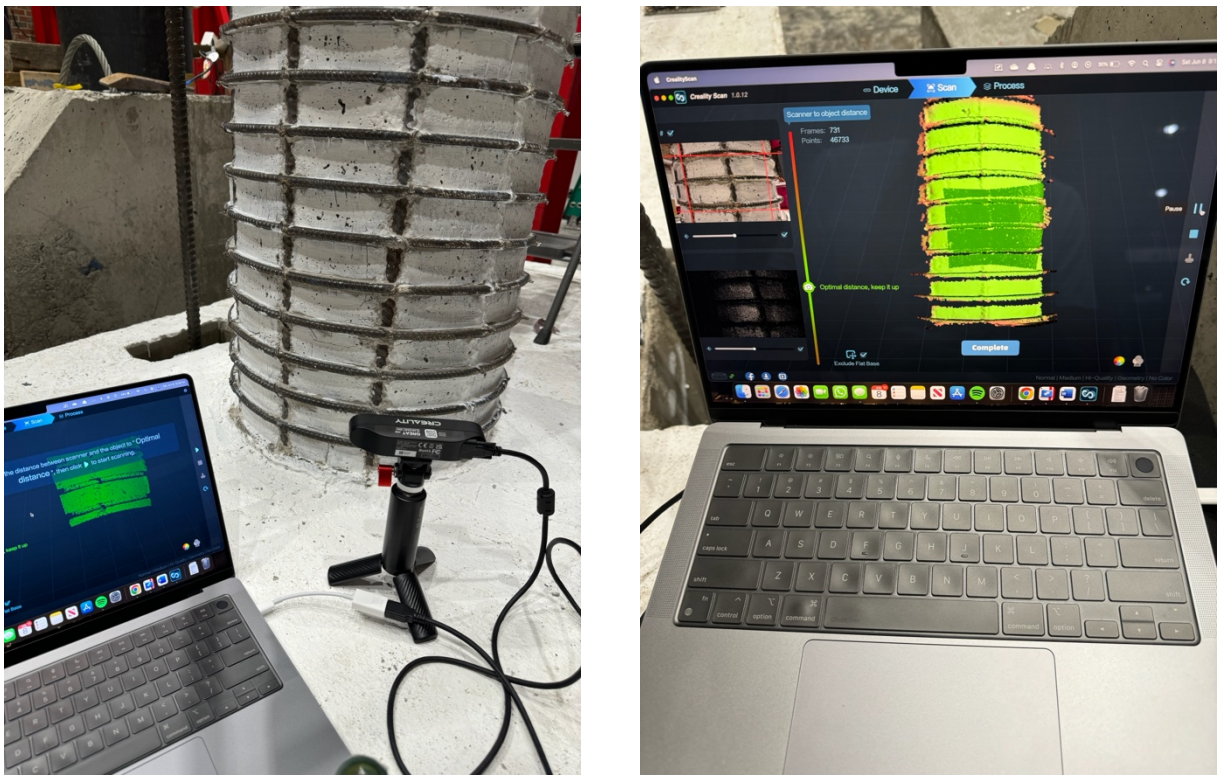



*Figure 5-5: Portable 3D scanner*

The following two sections summarize the 3D scanning process and findings for both the large-scale tests and the material tests.

### *5.3.1 Scanning of Large-Scale Tests*

As discussed in Section 3.1.2, the longitudinal steel for the large-scale tests was corroded prior to constructing the cage and casting. This allowed for the 3D scanning of the corroded bars. Initially, the scans of the longitudinal bars were used to verify the corrosion levels. The surfaces of the bars were scanned using the portable scanner seen in Figure 5-5. The scans from the scanner were transferred to Autodesk Fusion 360, a CAD software, where they were converted into mathematical meshes. The cross section of the meshes were then measured at small intervals to verify the desired level of corrosion. Following the casting and cleaning process of the large-scale columns, outlined in Section 3.1.2, the exposed longitudinal bars in the plastic hinge were scanned once again. The process and interface of the scanning program can be seen in Figure 5-6.




(a) (b)

*Figure 5-6: Scanning of large-scale columns: (a) scanning column; (b) scanner interface*

The scans of the column were analyzed after the column tests had concluded. For the extreme bars on the North side (N2, N3, N4) and South side (S2, S3, S4), pits were identified in the 3D meshes at one-inch intervals and their depths were measured. Special care was taken to identify pits that were in regions of bar fracture during the test. An example of measuring the depth of a pit from a column test can be seen in Figure 5-7. Please note that the measurements displayed in Figure 5-7 are scaled up as a result of Autodesk Fusion 360. These measurements were scaled down to accurately reflect the correct dimensions. The pit geometry was then related to various parameters such as column strength, displacement, and strain before buckling.

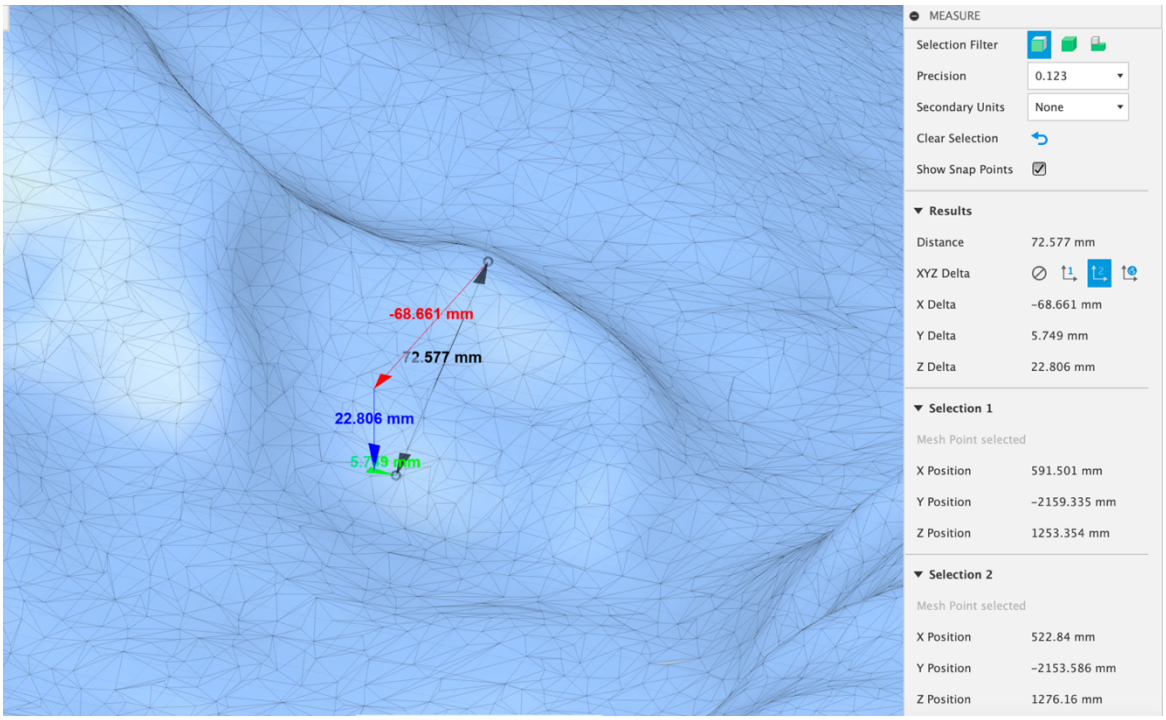



*Figure 5-7: Measuring column pit geometry – units not to scale*

### *5.3.2 Column Test Scanning Results*

To investigate how pit depth relates to bending strain, bending strains were calculated for all the column tests with Optotrak data. This is further discussed and presented in Section 6.1.4. Pit depth to bar diameter ratios (PDBD) were plotted against bending strains found before bar fracture as seen in Figure 5-8. A linear trend was observed between bending strain before fracture and PDBD as shown in Equation 5-4, and as the dashed line in Figure 5-8:

$$Bending\ Strain\ Before\ Fracture = 0.11 - 0.83(PDBD) \qquad \textit{Equation 5-4}$$

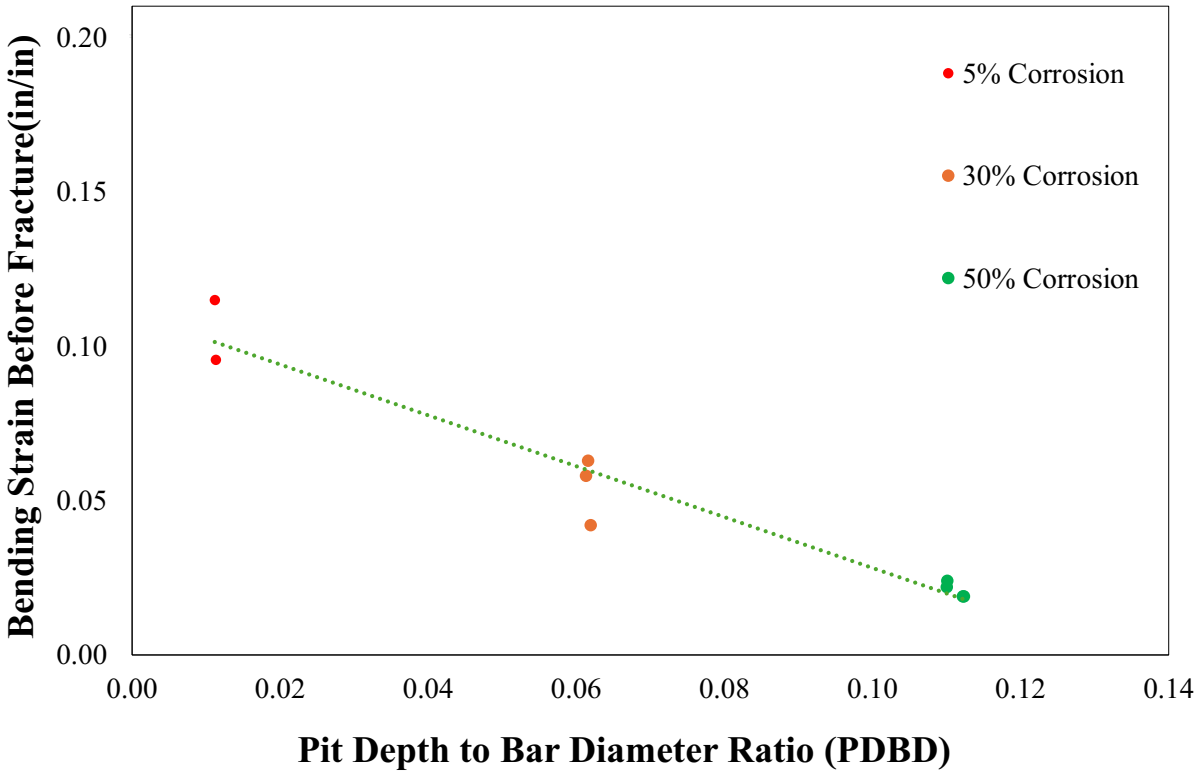



*Figure 5-8: Pit depth and bar diameter ratio versus bending strain before fracture*

### *5.3.3 Scanning of Material Test Specimens*

Rebar specimens that were used in both tension and BBT tests, were scanned prior to testing using the portable scanner. Similar to the longitudinal bars in the large-scale columns, pits in the 3D meshes were identified at one-inch intervals, with their depths recorded. Particular attention was given to locating pits in areas where bar fractures occurred during the material tests. The pit geometry was then related to various parameters such as max specimen stress, strain, and critical bending strain.

### *5.3.4 Material Test Scanning Results*

To investigate how pit depth relates to stress, pit depth to bar diameter ratios (PDBD) were plotted against maximum tensile stresses found in Section 5.1.2. Other measurable parameters were considered such as pit diameter however they were not explored during this phase of the project. The results can be seen in Figure 5-9. For each level of corrosion, the PDBD where bar fracture occurred was found and labeled. Additionally, a linear trend was observed between maximum tensile stress and PDBD as shown in Equation 5-5 and the dashed line in Figure 5-9:

$$Maximum\ Tensile\ Stress = 99.3 - 333.1(PDBD) \qquad \textit{Equation 5-5}$$

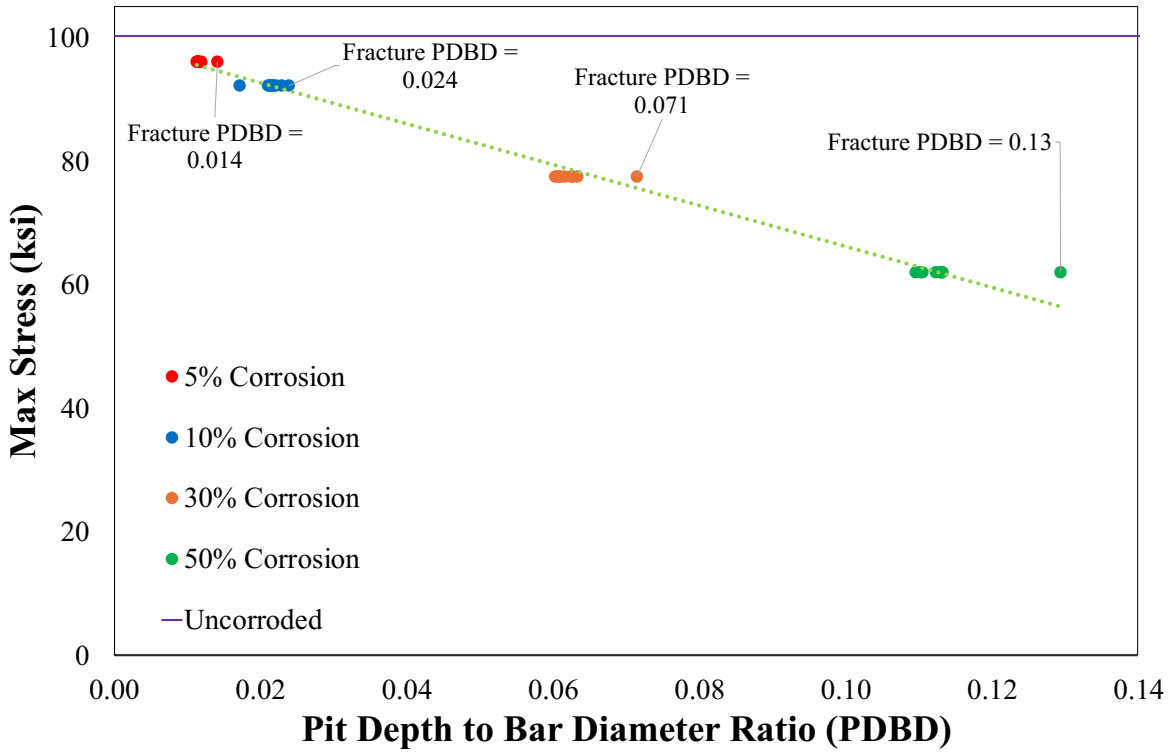



*Figure 5-9: Pit depth and bar diameter ratio versus maximum tensile stress*

PDBD was also plotted against strain at fracture as seen in Figure 5-10. The linear trend observed between the strain at fracture and PDBD is expressed as Equation 5-6 and the dashed line in Figure 5-10:

$$Fracture\ Strain = 0.16 - 0.53(PDBD) \qquad \textit{Equation 5-6}$$

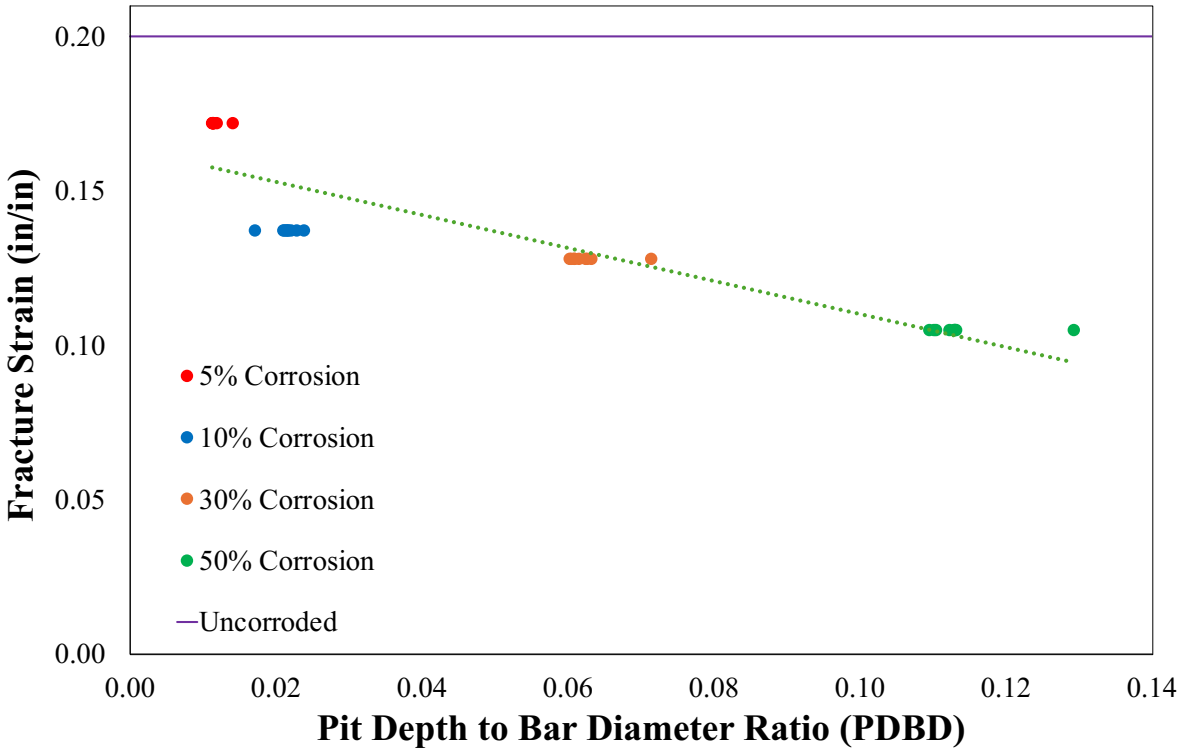



*Figure 5-10: Pit depth and bar diameter ratio versus strain at fracture*

For each BBT test specimen, the PDBD was plotted versus bending strain as seen in Figure 5-11. The critical bending strain values calculated in Section 5.2.2 are plotted as dashed lines. A linear trendline is observed between the critical bending strain and PDBD as shown in Equation 5-7 and dashed line in Figure 5-11:

$$Critical\ Bending\ Strain = 0.12 - 0.82(PDBD) \qquad \textit{Equation 5-7}$$

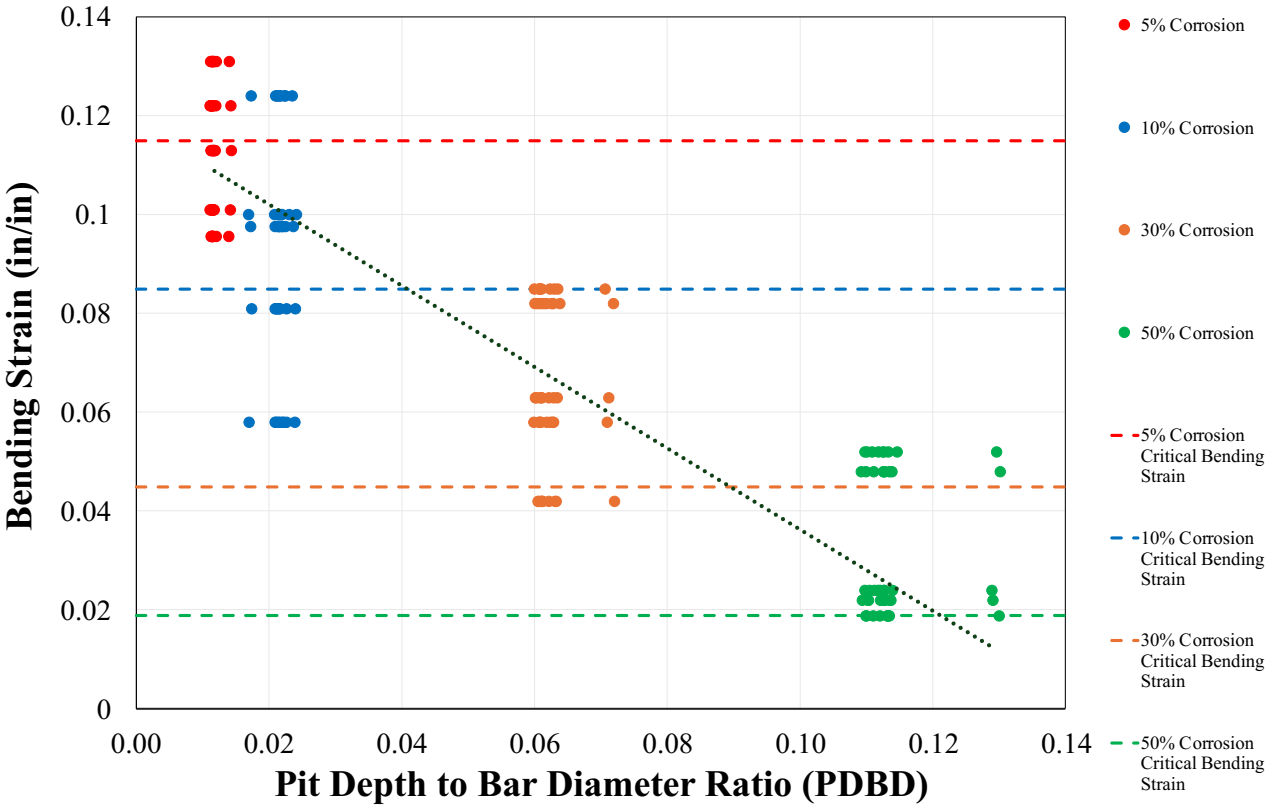



*Figure 5-11: Pit depth and bar diameter ratio versus bending strain*

It is useful to compare Equation 5-4 and Equation 5-7. Recall that Equation 5-4 is based on scans from the longitudinal bars in the column tests, while Equation 5-7 comes from scans of bars in the BBT tests. This comparison allows for an assessment of how the PDBD correlates with bending strain. Figure 5-12 displays both trend lines.

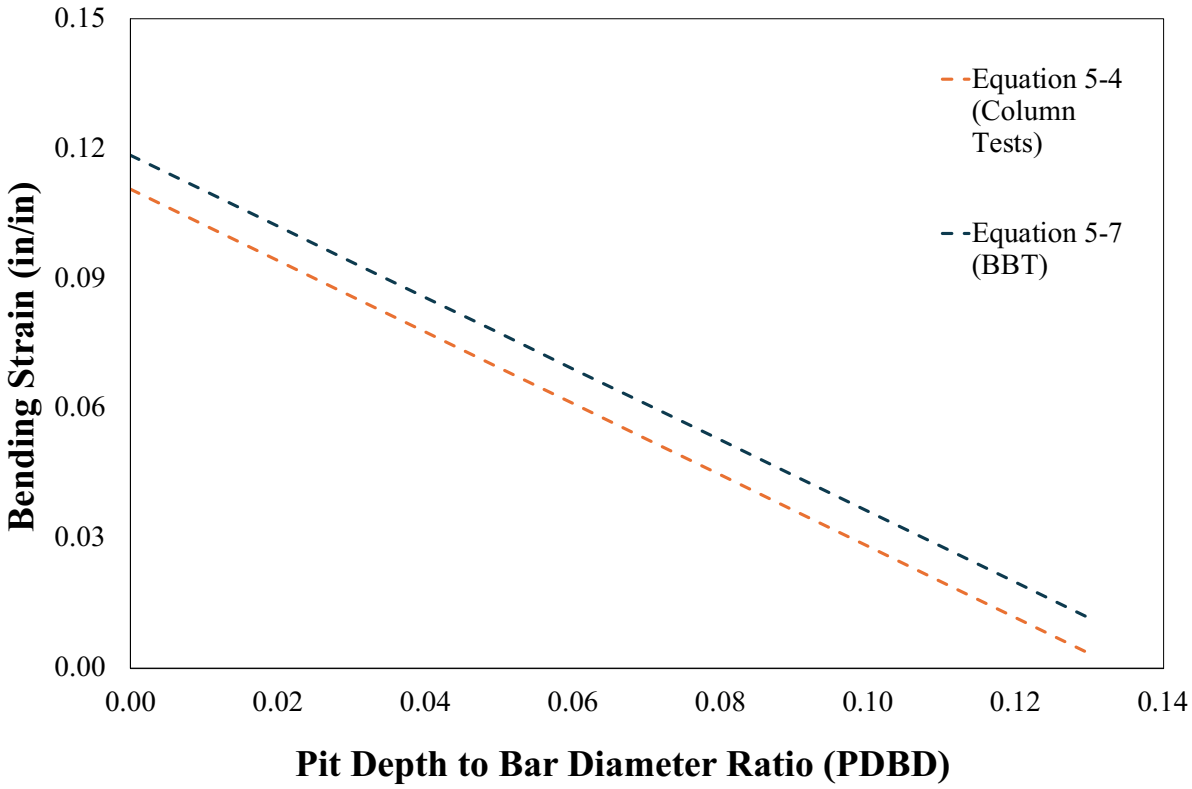



*Figure 5-12: Comparison of column tests and BBT pit depth and bar diameter ratio versus bending strain equations*

As Figure 5-12 shows, the trendlines for the BBT and the column tests are similar, except that the trendline for the BBT lies above the trendline for the column tests. It should be noted that Equations 5-4 through 5-7 are illustrative and based on a limited series of tests. Final recommendations will require additional investigation; however, the concept of using the PDBD as a critical measure to define various parameters appears promising.

# CHAPTER 6: RESULTS AND CORRELATION BETWEEN LARGE-SCALE TESTS AND MATERIAL TESTS

The objective of this research is to understand how corrosion affects the seismic performance of reinforced concrete bridge columns. To achieve this goal, a series of large-scale tests and material tests were conducted, as outlined in the previous chapters. The following chapter will be divided into two sections. The first section will compare the results from the four large-scale tests outlined in Chapter 4. The four column tests are summarized below in Table 6-1. The second section will compare the results from the large-scale tests to the results from the material level characterization discussed in Chapter 5.

*Table 6-1: Column test matrix*

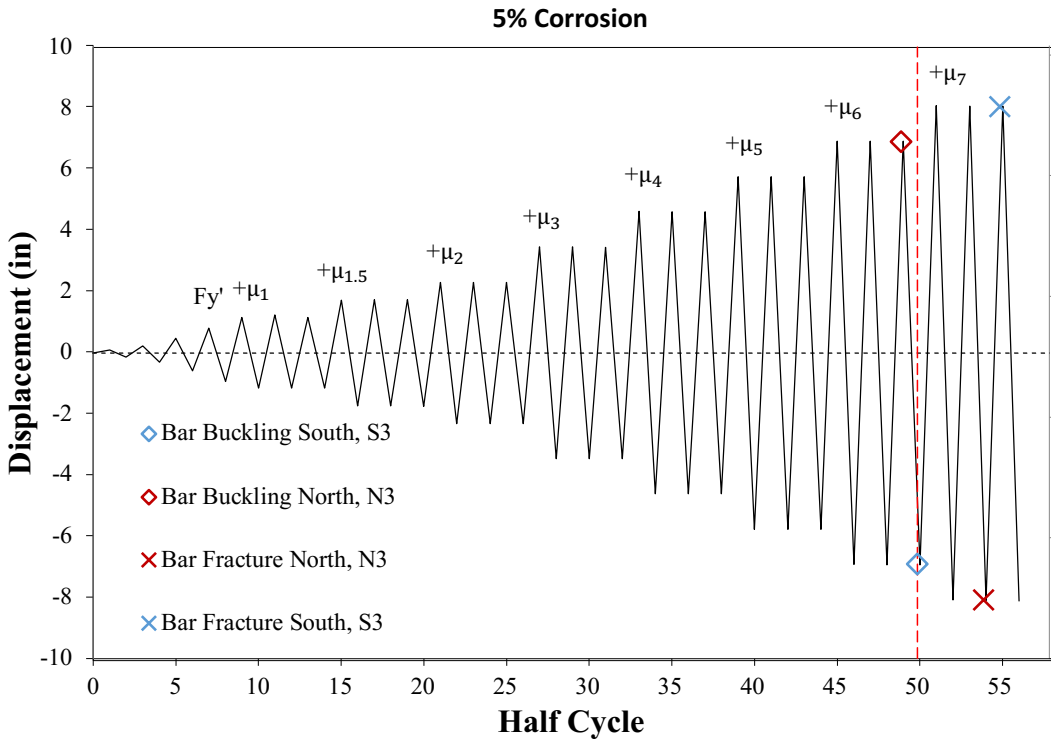
| Column Number | Dia. (in) | *L/D* Ratio | Longitudinal Steel | Transverse Steel (Spirals) | Axial Load Ratio | Corrosion Level |
|---|---|---|---|---|---|---|
| 1 | 18 | 5.33 | Gr. 60, 10 #6 (1.7%) | Gr. 60 #3 @2” (1.3%) | 10% | 10% |
| 2 | 18 | 5.33 | Gr. 60, 10 #6 (1.7%) | Gr. 60 #3 @2” (1.3%) | 10% | 5% |
| 3 | 18 | 5.33 | Gr. 60, 10 #6 (1.7%) | Gr. 60 #3 @2” (1.3%) | 10% | 30% |
| 4 | 18 | 5.33 | Gr. 60, 10 #6 (1.7%) | Gr. 60 #3 @2” (1.3%) | 10% | 50% |

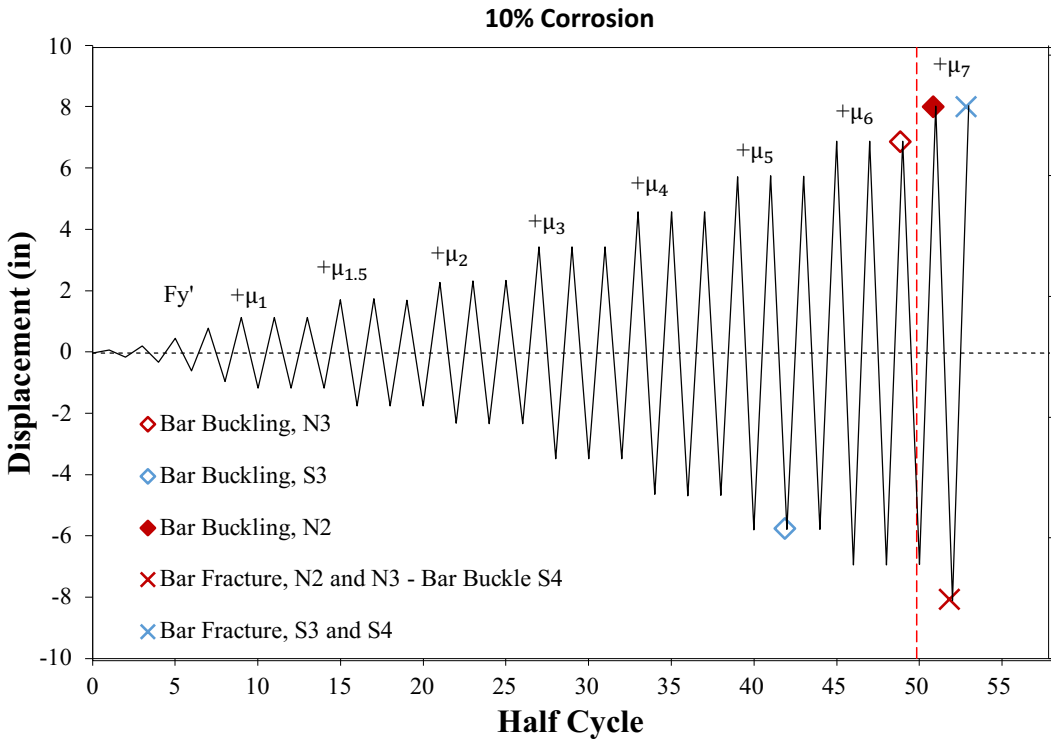
## 6.1 Large-Scale Tests Results

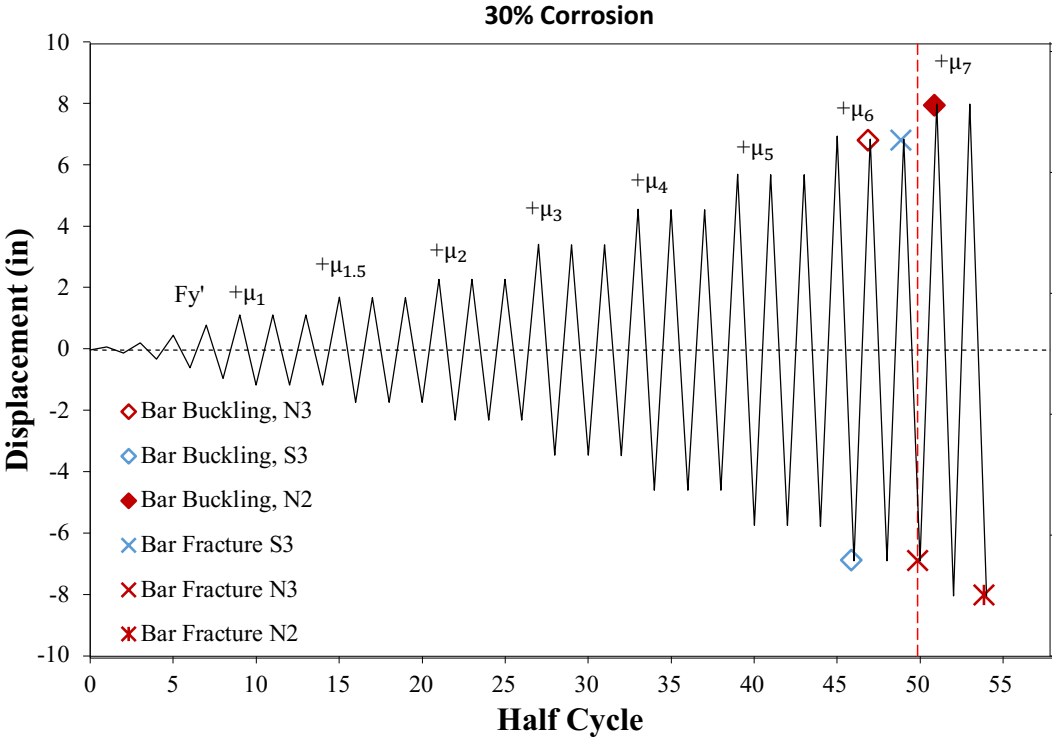
### *6.1.1 Global Response*

To compare the global response of each column, the following items will be compared: load history, backbone curve, and bar buckling and fracture limit states. Because all four columns had the same detailing and displacement history, it is possible to directly compare column performance. The goal of this section is to provide insight in how corrosion affects the overall response of bridge columns.

The load history of all four columns can be seen in Figure 6-1 with bar buckling and bar fracture limit states shown. To provide a reference point to help with visual comparison, each load history graph in Figure 6-1 has a vertical red dashed line at half cycle 50. Comparing the load histories of the four column tests, the buckling of bars occurred at similar levels of displacement. However, for higher levels of corrosion, bars fractured rapidly after buckling, and in the case of the column with 50% corrosion, some bars fractured without visual buckling. Additionally, for higher levels of corrosion the bar fractures were characterized as brittle in failure.




10% Corrosion
Displacement (in)
Half Cycle
Fy'
+μ1
+μ1.5
+μ2
+μ3
+μ4
+μ5
+μ6
+μ7
Bar Buckling, N3
Bar Buckling, S3
Bar Buckling, N2
Bar Fracture, N2 and N3 - Bar Buckle S4
Bar Fracture, S3 and S4


30% Corrosion
Displacement (in)
Half Cycle
Fy'
+μ1
+μ1.5
+μ2
+μ3
+μ4
+μ5
+μ6
+μ7
Bar Buckling, N3
Bar Buckling, S3
Bar Buckling, N2
Bar Fracture S3
Bar Fracture N3
Bar Fracture N2

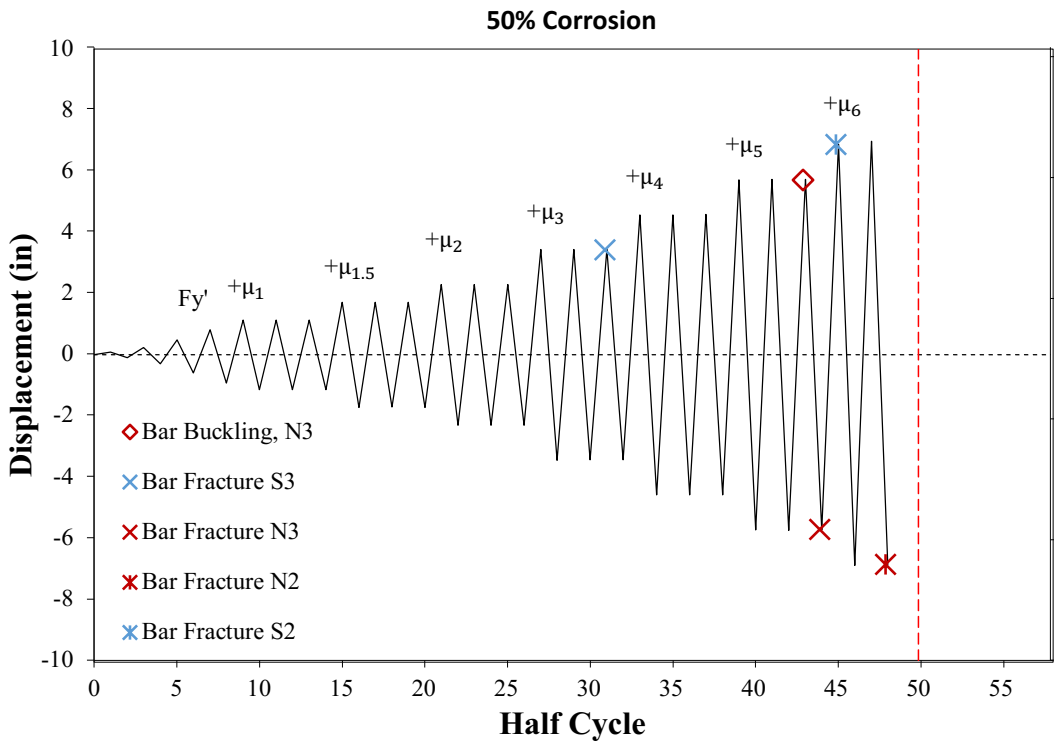
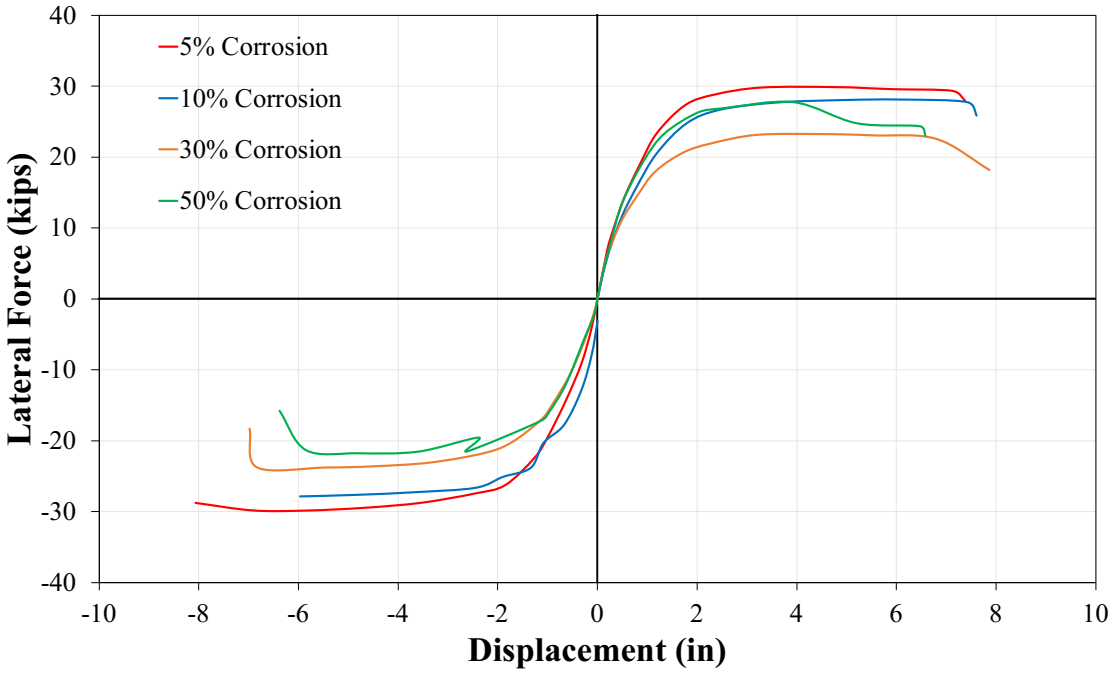
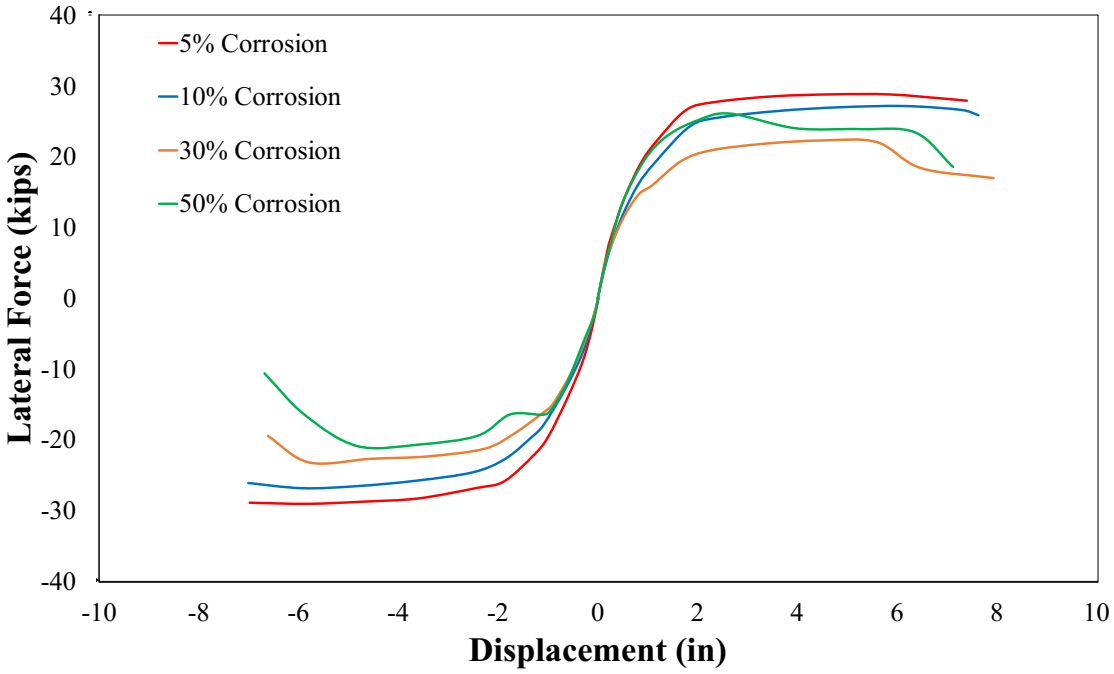



*Figure 6-1: Load history comparison of all column tests*

The backbone response of all the column tests can be seen in Figure 6-2.




(a)

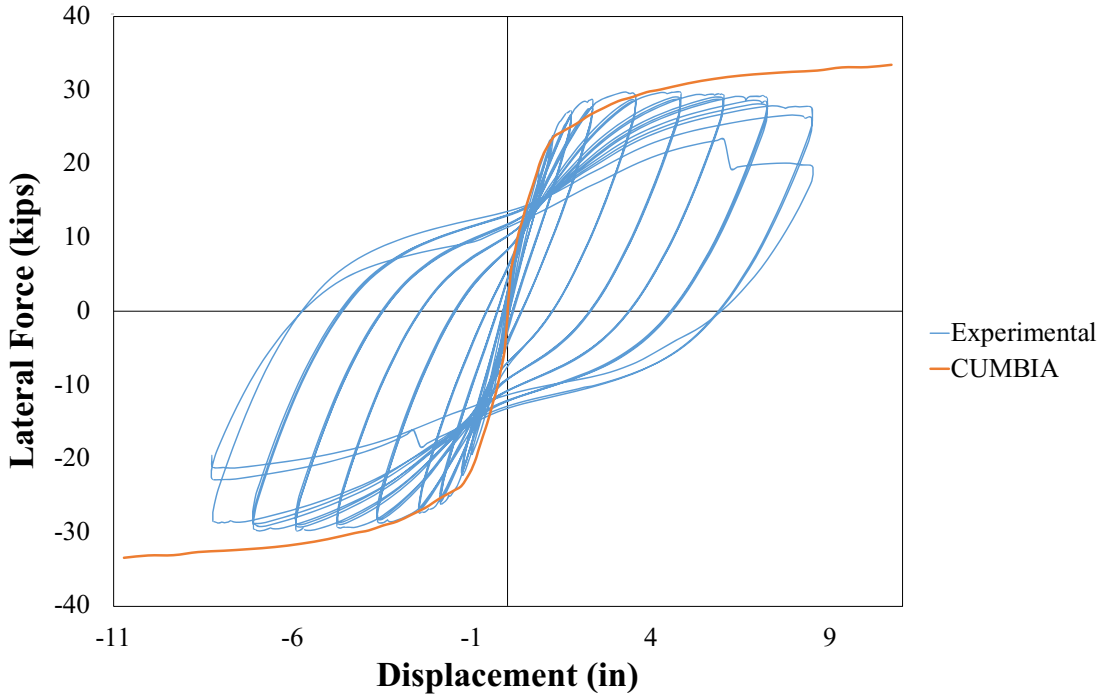



(b)

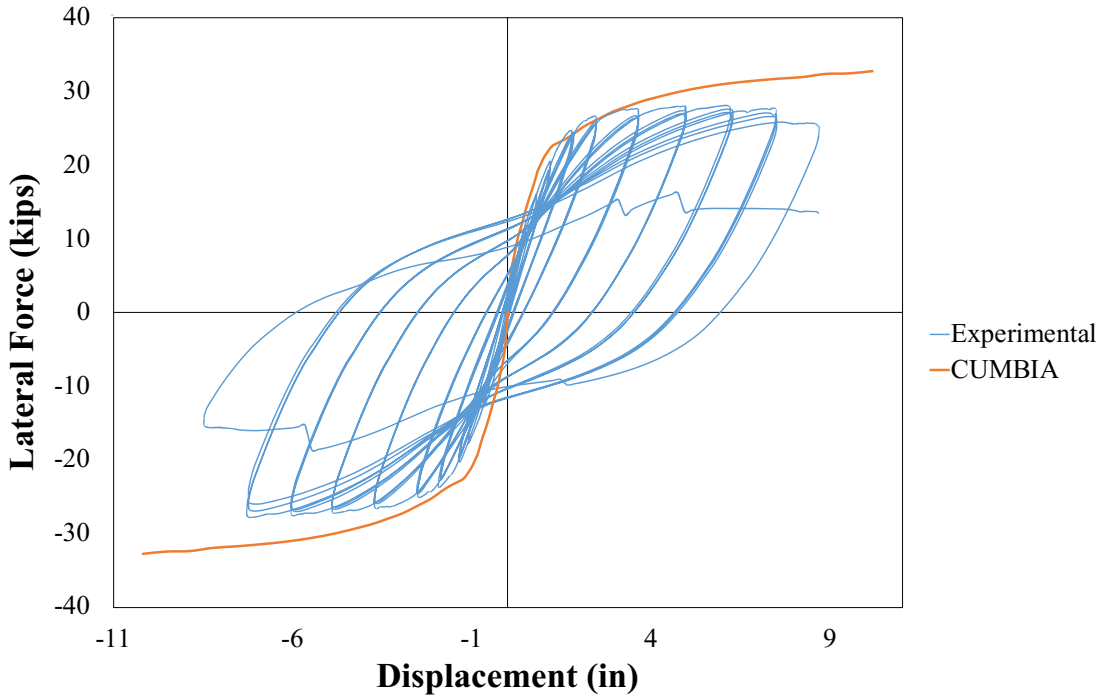
*Figure 6-2: Backbone comparison of all column tests: (a) first cycle; (b) third cycle*

As Figure 6-2 shows, the backbone curves for all four tests are similar except for a general reduction in strength with increase of corrosion levels. Although the initial stiffnesses for the four tests were similar, for higher levels of corrosion as displacements increased, a reduction of stiffness is observed. This is explored further in Section 6.1.5.

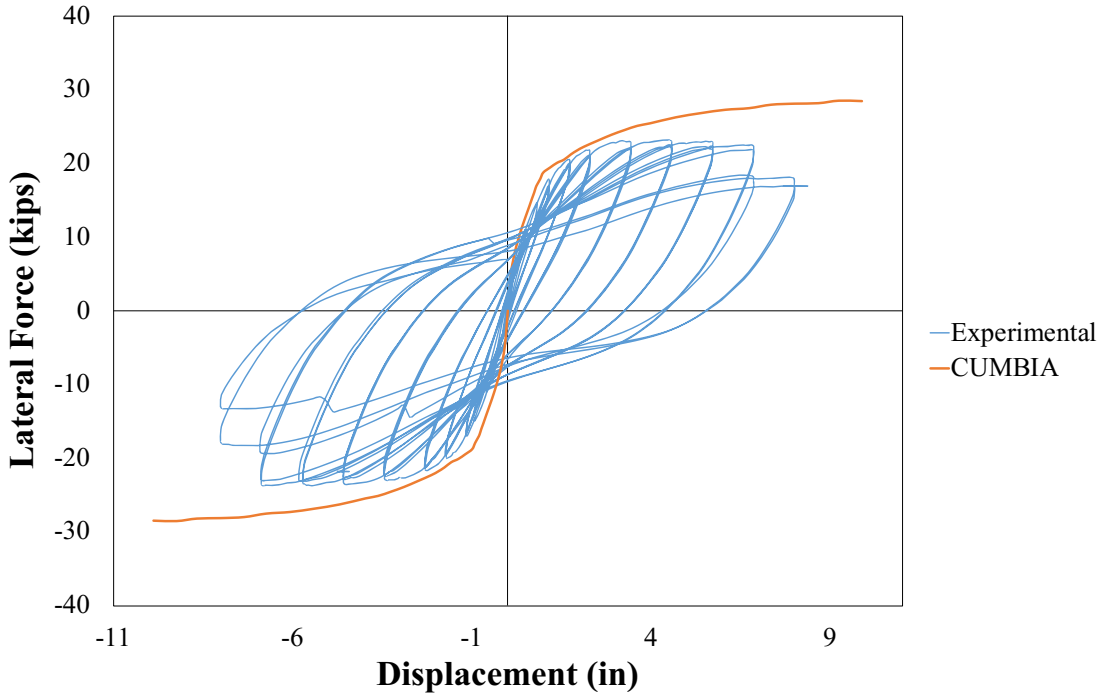
To analyze how the experimental results align with current analytical modeling practices, a monotonic moment-curvature analysis was conducted using CUMBIA, a collection of MATLAB codes developed Montejo and Kowalsky (2007). CUMBIA uses confined and unconfined concrete models developed by Mander et al. (1988) and King et al. (1986). The program predicted the force-displacement response of each test, using the corresponding concrete and steel properties. The actual stress-strain graphs from the corroded material tests were inputted into the program. The cross-sectional area of the longitudinal steel was uniformly reduced in the program to achieve the desired level of corrosion. The predictions were then compared to the experimental force-displacement results, as seen in Figure 6-3.


Lateral Force (kips)
40
30
20
10
0
-10
-20
-30
-40
-11
-6
-1
4
9
Displacement (in)
Experimental
CUMBIA

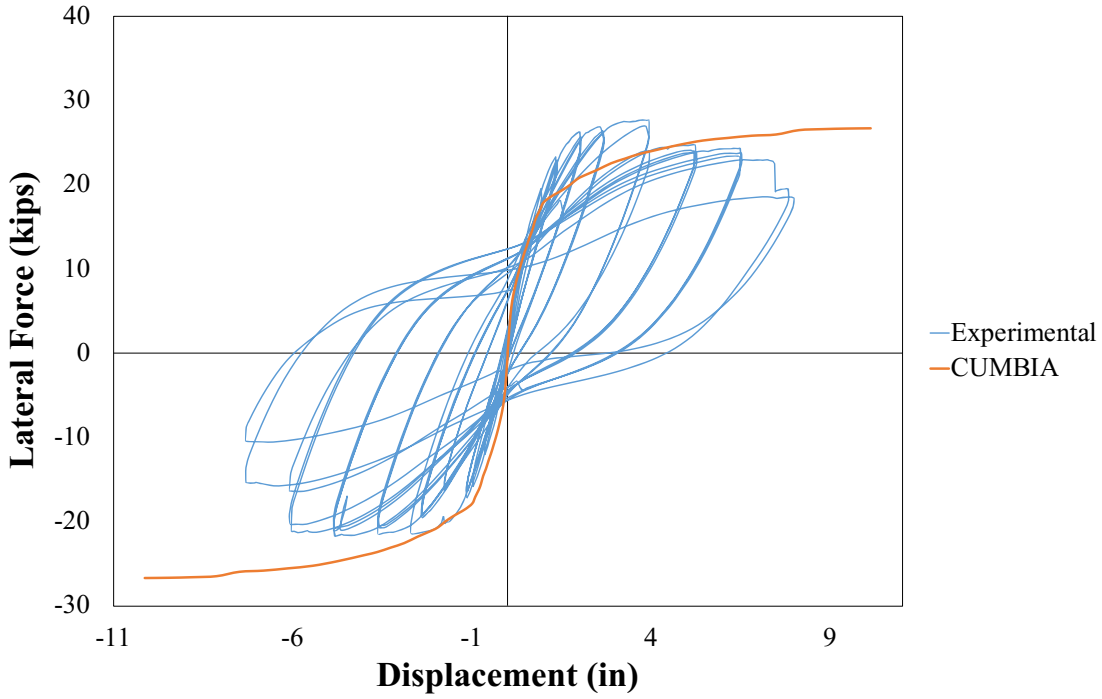
(a)


Lateral Force (kips)
40
30
20
10
0
-10
-20
-30
-40
-11
-6
-1
4
9
Displacement (in)
Experimental
CUMBIA

(b)




(c)




(d)

*Figure 6-3: Comparison of experimental vs. CUMBIA backbone curve: (a) 5% corrosion; (b) 10% corrosion; (c) 30% corrosion; (d) 50% corrosion*

As shown in Figure 6-3, although the actual column tests were similar, CUMBIA generally overpredicted the column performance. This overprediction is due to the program assuming uniform section loss, rather than accounting for the non-uniform pit corrosion observed in the actual longitudinal steel. The presence of pits in the steel creates stress concentrations that significantly compromise the material's structural integrity and performance.

### *6.1.2 Axial Strain Demands*

In this section, the strain profiles from the column tests with Optotrak data are compared. As discussed in Section 4.2.2, strains were calculated using position data from the Optotrak LED markers. Strain profiles were calculated for the first cycle of each ductility following yield. The maximum axial strains, calculated as the average of the extreme bars N3 and S3, for both tension and compression can, be seen in Table 6-2 and Table 6-3.

*Table 6-2: Axial tension strain summary*

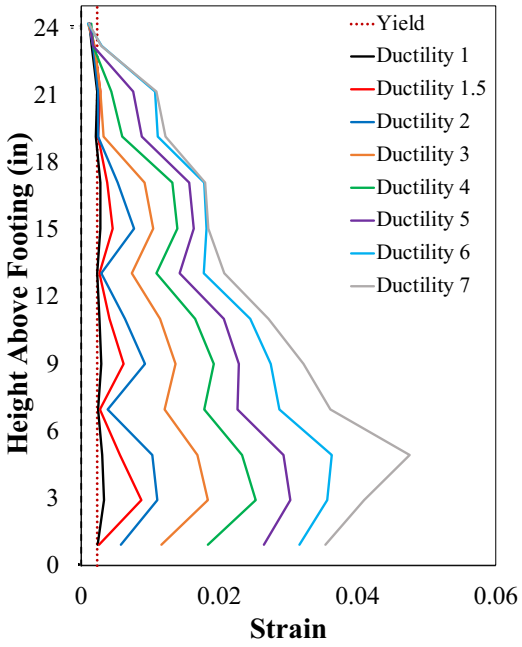
| Column Corrosion Level | Measured Strain (%) | | | | | | | |
|---|---|---|---|---|---|---|---|---|
| | $\mu_1$ | $\mu_{1.5}$ | $\mu_2$ | $\mu_3$ | $\mu_4$ | $\mu_5$ | $\mu_6$ | $\mu_7$ |
| 5% | 0.34 | 0.92 | 1.13 | 1.80 | 2.42 | 2.98 | 3.57 | 5.19 |
| 30% | 0.44 | 0.88 | 1.28 | 2.24 | 3.13 | 4.30 | 5.63 | - |
| 50% | 0.46 | 1.12 | 1.87 | 3.4 | - | - | - | - |

*Table 6-3: Axial compression strain summary*

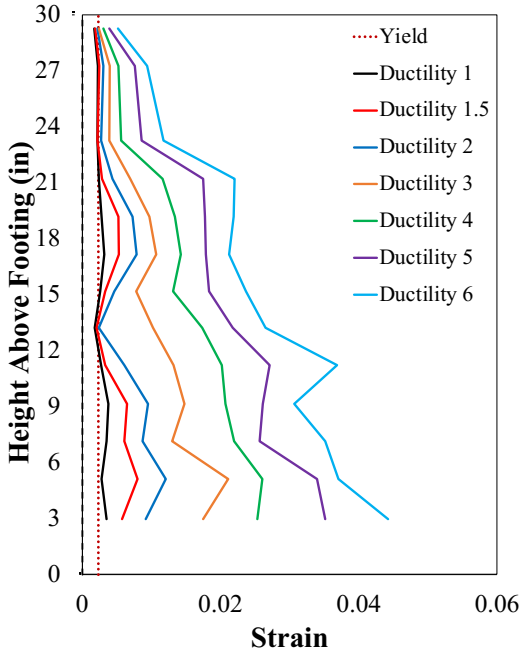
| Column Corrosion Level | Measured Strain (%) | | | | | | | |
|---|---|---|---|---|---|---|---|---|
| | $\mu_1$ | $\mu_{1.5}$ | $\mu_2$ | $\mu_3$ | $\mu_4$ | $\mu_5$ | $\mu_6$ | $\mu_7$ |
| 5% | 0.23 | 0.37 | 0.48 | 0.81 | 1.10 | 1.61 | 2.35 | - |
| 30% | 0.25 | 0.35 | 0.47 | 0.97 | 1.19 | 1.53 | 1.57 | 4.22 |
| 50% | 0.27 | 0.69 | 0.66 | 1.02 | 1.26 | 2.97 | 4.66 | - |

As seen in Table 6-2 and Table 6-3, the maximum measured axial strains are higher for higher levels of corrosion at any given ductility. This can be explained by reduction of load-carrying capacity with higher levels of corrosion, leading to larger deformations and higher axial strains under the same loading conditions. The strain profiles from the North or South extreme bar,

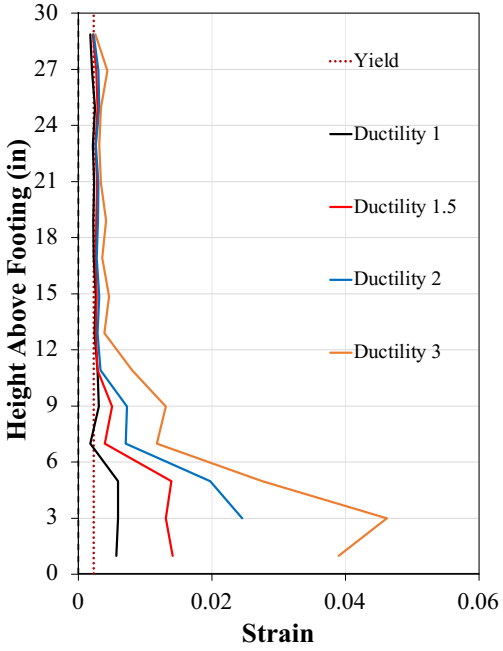
N3 or S3, for each column test with Optotrak data available are compared in Figure 6-4 and Figure 6-5. As discussed in Section 4.2.2, the spread of plasticity for each profile is a visual approximation.




(a)

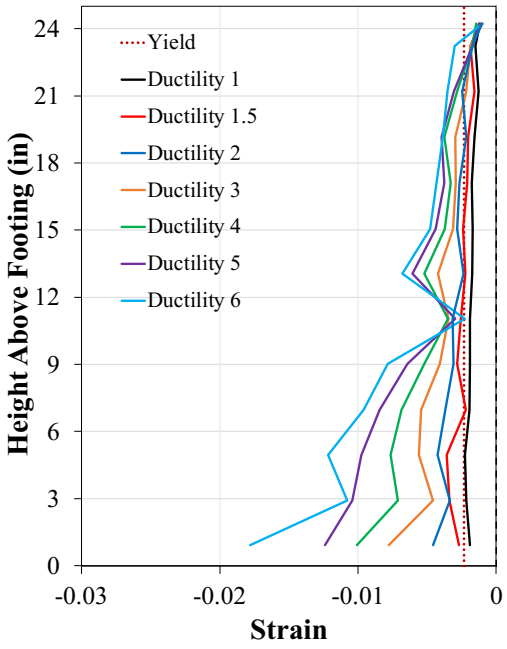



(b)

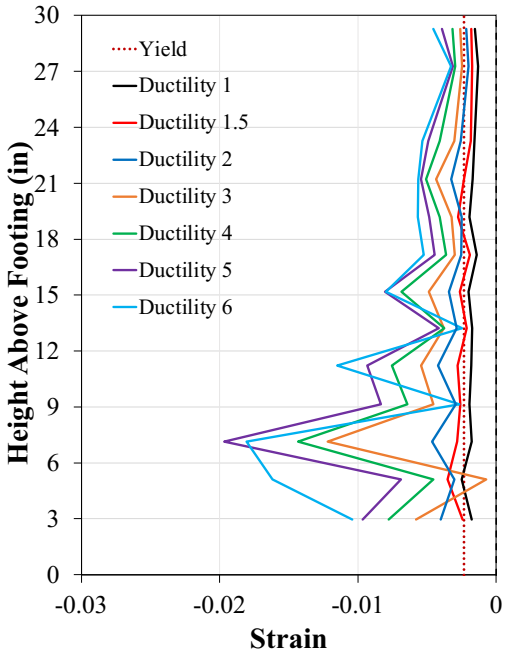



(c)

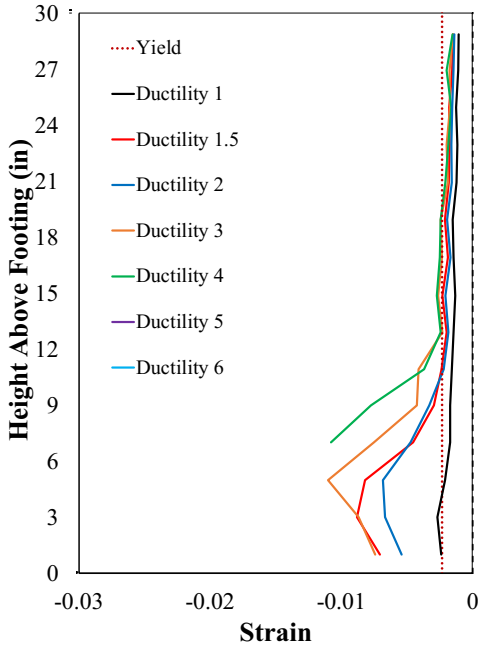
*Figure 6-4: Tension strain profiles: (a) 5% corrosion; (b) 30% corrosion; (c) 50% corrosion*




(a)




(b)




(c)

*Figure 6-5: Compression strain profiles: (a) 5% corrosion; (b) 30% corrosion; (c) 50% corrosion*

As Figure 6-4 and Figure 6-5 show, the extent of plasticity decreases with higher levels of corrosion, likely as a consequence of greater localization of strains.

### *6.1.3 Damage Limit States*

As illustrated in Section 4.2.5, strain histories of the longitudinal bars can be correlated to damage limit states of the column such as concrete cracking, concrete crushing, bar buckling, and bar fracture. The strain at the damage limit states for all the column tests with Optotrak data can be seen in Table 6-4. For concrete cracking and crushing, the maximum strain values were determined at the ductility level where the corresponding damage was observed, and an average was taken between the North and South extreme bars, N3 and S3. Concrete crushing was typically measured during compression cycles. For bar buckling and bar fracture, the strain values were found by plotting strain versus displacement as shown in Section 4.2.2, and an average was taken between the North and South extreme bars, N3 and S3.

*Table 6-4: Damage limit states comparison*

| Damage State | Measured Strain (in/in) |
|---|---|

| | 5% Corrosion | 30% Corrosion | 50% Corrosion |
|---|---|---|---|
| Concrete Cracking | 0.003 | 0.0011 | 0.0011 |
| Concrete Crushing | 0.0074 | 0.0056 | 0.00715 |
| Bar Buckling | 0.0350 | 0.0329 | 0.0321 |

### *6.1.4 Bending Strain*

To understand the strain distribution and capacity of the buckled longitudinal bars, bending strains were calculated using the same procedure as the BBT tests in Section 5.1.1. Bending strains were calculated for each longitudinal bar that fractured using the Optotrak data of four to five LED markers in different regions of the bar. A fourth-order polynomial was fit to these points to approximate the bar position in the last compression cycle before fracture. Because the LED markers were glued to the surface of the longitudinal bars, the LED positions had to be corrected to the bar's neutral axis. To calculate the bar's curvature, φ, Euler-Bernoulli beam theory was utilized. The curvature was calculated as the second derivative of the displaced shape, *w*, as show in Equation 6-1. Because at maximum curvature the displacements are at a minimum, the curvature can be approximated as the second derivative of position, as shown in Equation 6-2. Maximum bending strain, $e_b$, would then be calculated by multiplying curvature by half the rebar specimen diameter as seen in Equation 6-3.

$$\varphi = \frac{\frac{d^2w}{dx^2}}{\left[1 + \left(\frac{dw}{dx}\right)^2\right]^{3/2}} \qquad \textit{Equation 6-1}$$

$$\varphi \approx \frac{d^2w(x)}{dx^2} \qquad \textit{Equation 6-2}$$

$$e_b = \varphi \frac{d_b}{2}$$ *Equation 6-3*

The bending strains were plotted for each loading cycle to give a bending strain history. Critical bending strain, $e_{cr}$, values was also calculated for each column test, using the methods discussed in Section 5.1.1. The bending strain histories for all the column tests with Optotrak data available are plotted below in Figure 6-6. For each column test, the bending strains for the extreme longitudinal bars (N2, N3, N4, S2, S3, S4) were found. Bending strain before fracture is denoted by a red "x", and the highest strain without fracture is represented with a black square. The shaded portions represent the longitudinal bars for the different column tests. The values of bending strain before fracture were related to pit geometry in Figure 5-8 in Section 5.3.2.

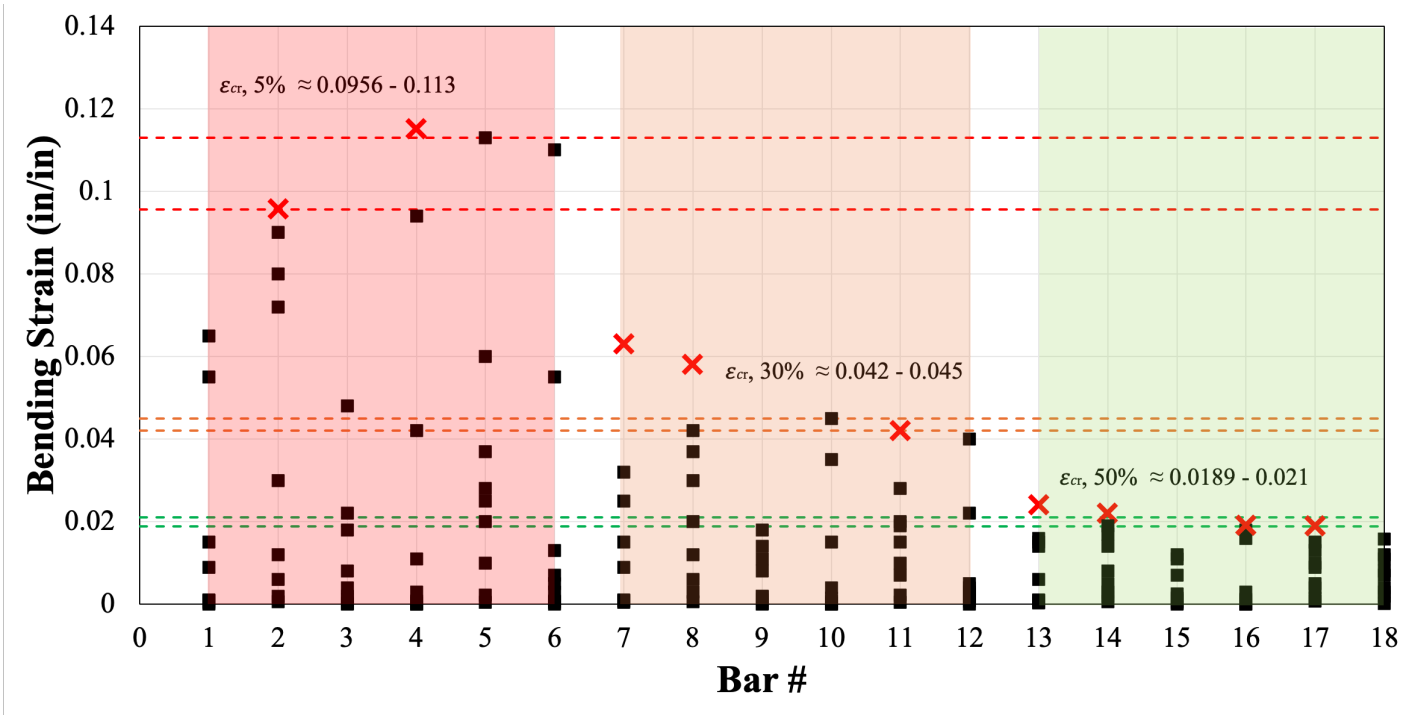



*Figure 6-6: Column tests bending strain history: red – 5% corrosion; orange – 30% corrosion; green – 50% corrosion*

As Figure 6-6 shows, with increasing levels of corrosion, the critical bending strain reduces. This implies that corroded reinforcing steel will fracture at lower levels of bending strain, and that corroded reinforcing steel will sustain less cycles between bar buckling and fracture, as observed in Section 6.1.1. A comparison to uncorroded columns can be found in Appendix D.

### *6.1.5 Cumulative Energy Dissipation*

Finding the energy dissipated through hysteresis in reinforced concrete columns enhances structural integrity assessments and evaluates damage accumulation under cyclic loading. This understanding informs design optimization, predictive modeling, and performance-based approaches, especially in seismic applications. Because all four column tests were subjected to the same displacement history and axial load, the energy at each cycle could be compared directly. To determine the energy dissipation of the columns, the area-based method was used as described in Section 4.1.4. The total cumulative energy of the four column tests can be seen in Figure 6-7. In general, higher levels of corrosion had lower energy dissipation at each cycle.

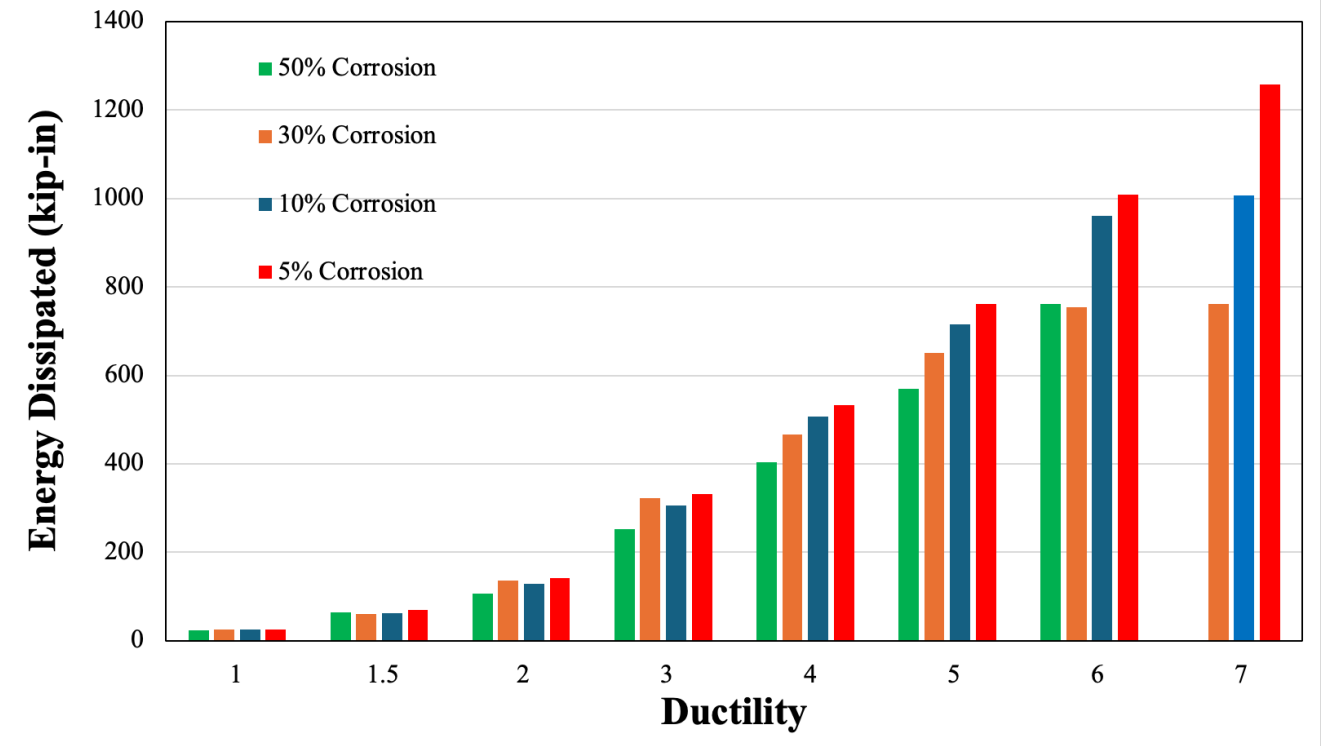



*Figure 6-7: Energy dissipation comparison*

## 6.2 Large-Scale Tests and Material Tests

As discussed in the previous sections, to understand how corrosion affects the seismic performance of bridge columns, material tests as well as large-scale tests were conducted. The goal of this section is to establish a connection between the performance of the reinforcing steel observed in the material tests and the seismic performance of the large-scale tests discussed in Chapters 4 and 5. The results from the BBT tests will specifically be compared to the large-scale tests to assess its relevance in predicting the seismic performance of corroded RC columns.

A total of 30 BBT tests were performed with corrosion levels ranging from 0% to 50%. For each corrosion level a total of 6 BBT tests were performed. In addition, for each corrosion level, the critical bending strain, $e_{cr}$, was found. A total of four large-scale column tests were conducted with corrosion levels ranging from 5% to 50%. Of the four column tests, three had Optotrak data available, allowing for the calculation of stains. For each of these tests, bending strains were calculated along with the critical bending strains. The critical bending strains comparison between the materials tests and the column tests can be seen in Table 6-5 as well as Figure 6-8.

*Table 6-5: Comparison summary critical bending strains of BBT vs. column tests*

| Corrosion Level | Critical Bending Strain, $e_{cr}$ (in/in) | |
|---|---|---|
| | BBT Test | Column Test |
| 5% | 0.115 | 0.0956 – 0.113 |
| 10% | 0.085 | N/A |
| 30% | 0.045 | 0.042 – 0.045 |
| 50% | 0.019 | 0.0189 – 0.021 |

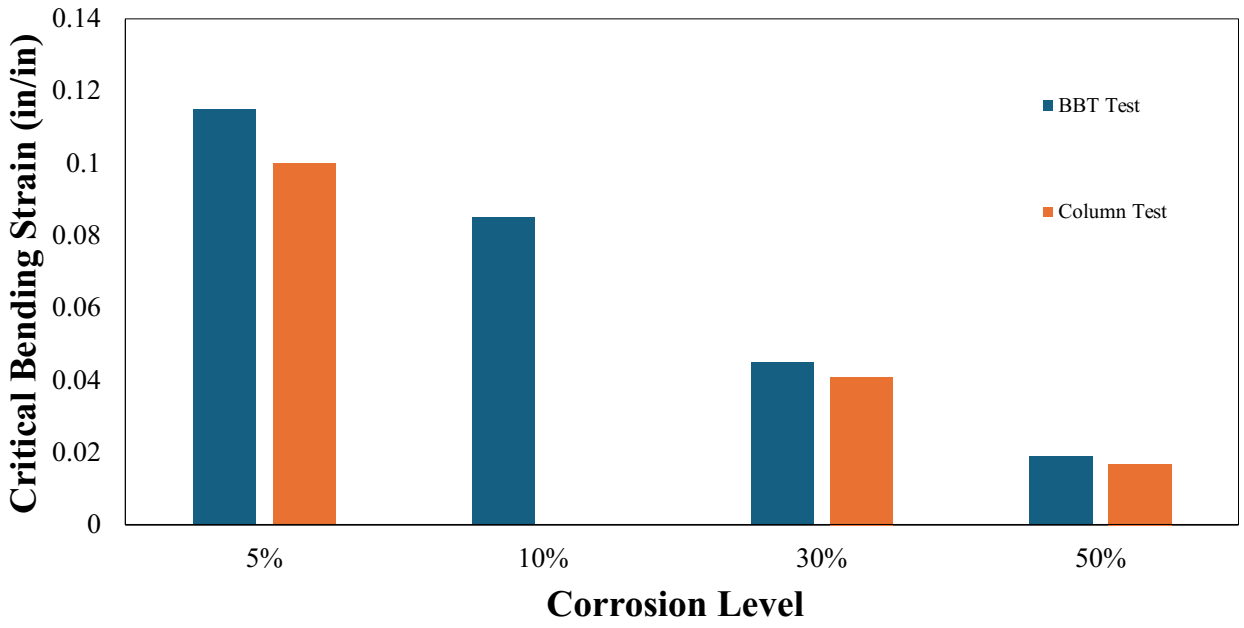



*Figure 6-8: Comparison of critical bending strains of BBT vs. column tests*

As Table 6-5 and Figure 6-8 show, the BBT test results correlate well with the column tests with critical bending strain values varying from 9% to 14%. In all cases, the critical bending strain values from the column tests were lower than the BBT tests. There are several possible explanations such as the LED gage length difference between the material tests and column tests, as well as number of loading cycles. Despite these differences, the BBT test remains an effective method for predicting post-buckling of reinforcing steel.

To see how well the 3D scans and BBT results correlate with the 3D scans of the large-scale columns, the pit depth to bar diameter ratios (PDBD) of the fractured longitudinal bars in the column tests were plugged into Equation 5-7, which is based off material tests from Section 5.3.4. The critical bending strains calculated using Equation 5-7, are compared to the actual column critical bending strains calculated using the methods discussed in Section 6.1.4, as seen in Table 6-6. As the results show, the critical bending strains calculated using Equation 5-7, overpredict the actual values by 4% to 38%. There are several possible explanations for the difference such as greater resolution needed from the 3D scans as well as more material tests to refine Equation 5-7.

*Table 6-6: Critical bending strains and 3D scans*

| Corrosion Level | Critical Bending Strain, $e_{cr}$ (in/in) | |
|---|---|---|
| | Equation 5-7 | Column Test |
| 5% | 0.108 - 0.109 | 0.0956 – 0.113 |
| 30% | 0.066 – 0.067 | 0.042 – 0.045 |
| 50% | 0.025 – 0.028 | 0.0189 – 0.021 |

# CHAPTER 7: SUMMARY AND DESIGN RECOMMENDATIONS

The objective of this study was to understand the impact of corrosion on the seismic behavior of bridge columns via material level and large-scale tests. While extensive research in the literature has focused on the impact of section loss due to corrosion, the specific hypothesis of this research is that the geometric imperfections caused by corrosion lead to a reduction in reinforcing bar strain capacity, and hence ductility.

Four circular reinforced concrete columns with identical detailing and varying levels of corrosion, ranging from minimum to severe, were constructed and tested at the CFL at NC State. Tension tests and buckled bar tension (BBT) tests were conducted on corroded material samples to assess the performance at the material level as well as find a correlation between the column tests and the material tests. The use of 3D scanning was implemented to capture the corroded surface of the corroded steel used in the column tests and material tests. The 3D scans helped visualize and measure localized pitting (to investigate the primary hypothesis of this research) and cross-sectional area reduction in the reinforcement. The following outlines the key conclusions found in the project as well as design recommendations.

## 7.1 Conclusions

1. *Corrosion Significantly Impacts Seismic Performance:*

The study shows that increasing corrosion levels lead to a reduction in both the strength and ductility of reinforced concrete bridge columns. The experimental results highlighted that corroded columns experience premature failure under seismic loads due to strain concentrations from corrosion induced pitting which reduce the material strain capacity. Furthermore, corrosion involves more than just cross-sectional loss; the surface imperfections created by corrosion can lead to stress concentrations that significantly compromise the material's structural integrity and performance.

2. *Structural Vulnerability Increases with Corrosion induced imperfections:*

At higher corrosion levels (30% and above), the failure modes changed from ductile to brittle, with columns exhibiting buckling and early fractures in steel reinforcement. This vulnerability highlights the urgent need for preventive maintenance in bridges subjected to corrosion in seismic regions.

3. *Validation of Mechanical Degradation Models:*

The large-scale column tests aligned closely with the material level Buckled Bar Tension (BBT) tests, further supporting that the BBT test is an effective predictor of performance. This correlation provides confidence in using analytical models for predicting the remaining life of aging infrastructure. In addition, the use of 3D can be used to capture the corroded surface of reinforcing steel. By measuring parameters in the 3D scans such as pit depth, engineers can assess the severity of corrosion and predict the steel's structural integrity. This information aids in estimating corrosion rates, planning maintenance, and implementing proactive strategies to ensure safety and longevity in structures.

4. *Energy Dissipation Diminished by Corrosion:*

As corrosion levels increased, the columns' ability to dissipate energy during seismic loading cycles decreased. This degradation may compromise the overall resilience of the structure.

5. *Importance of Early Detection and Maintenance:*

The study underscores the importance of early detection and treatment of corrosion to maintain seismic performance and avoid catastrophic failures. Regular monitoring and assessment are crucial, especially in seismic zones and coastal areas.

## 7.2 Design Recommendations

1. *Implement Corrosion-Resistant Materials:*

Future designs should prioritize the use of corrosion-resistant materials, such as galvanized or stainless-steel reinforcements, especially for bridge columns located in corrosive environments like coastal regions or areas where de-icing salts are frequently used.

2. *Establish Routine Monitoring Programs:*

Existing structures, particularly in high-risk seismic zones, should be regularly inspected for signs of corrosion. Implementing non-destructive testing methods such as 3D scanning or other advanced techniques can help identify early signs of material loss and geometry of imperfections, allowing for timely interventions.

3. *Strengthen Design Codes for Corroded Structures:*

Building codes and seismic design standards should be updated to incorporate the effects of corrosion over time. Structural engineers should factor in the expected degradation of materials when calculating seismic load resistance, especially in older bridges that may not have been designed with long-term corrosion in mind.

4. *Retrofit Aging Infrastructure:*

Older, corroded bridges should be retrofitted by replacing vulnerable steel. This could be accomplished by smoothing imperfections, splicing in new material, or hinge relocation, amongst other options.

5. *Further Research into Corrosion Effects:*

While the study provides significant insights into the impacts of corrosion on seismic performance, more research is needed to investigate the long-term effects of varying environmental conditions. Future studies should explore different corrosion levels, material compositions, and real-world corrosion cases to refine predictive models further. This could include shake table tests with corroded columns and additional material tests with 3D scanned corroded specimens.

# CHAPTER 8: REFERENCES


Almusallam, A. A. (2001). Effect of degree of corrosion on the properties of reinforcing steel bars. *Construction and Building Materials*, *15*(8), 361–368. https://doi.org/10.1016/S0950-0618(01)00009-5

Andisheh, K., Scott, A., & Palermo, A. (2021). Effects of corrosion on stress–strain behavior of confined concrete. *Journal of Structural Engineering*, *147*(7), 04021087. https://doi.org/10.1061/(ASCE)ST.1943-541X.0003005

Barcley, L., & Kowalsky, M. (2019). Critical bending strain of reinforcing steel and the buckled bar tension test. *Materials Journal*, *116*(3), 53–61. https://doi.org/10.14359/51715583

Calderon, V. A. (2022). *Condition Dependent Performance Based Seismic Design*. North Carolina State University.

Di Carlo, F., Meda, A., & Rinaldi, Z. (2017). Numerical evaluation of the corrosion influence on the cyclic behaviour of RC columns. *Engineering Structures*, *153*, 264–278. https://doi.org/10.1016/j.engstruct.2017.10.020

D. J. King, M. J. N. Priestley, and R. Park, "Computer Programs for Concrete Column Design," *Res. Rep. 86/12*, 1986.

Du, Y. G., Clark, L. A., & Chan, A. H. C. (2005). Residual capacity of corroded reinforcing bars. *Magazine of Concrete Research*, *57*(3), 135–147. https://doi.org/10.1680/macr.2005.57.3.135

Ghods, P., Isgor, O. B., McRae, G., & Miller, T. (2009). The effect of concrete pore solution composition on the quality of passive oxide films on black steel reinforcement. *Cement and Concrete Composites*, *31*(1), 2–11. https://doi.org/10.1016/j.cemconcomp.2008.10.003

Kashani, M. M., Crewe, A. J., & Alexander, N. A. (2012). Nonlinear stress–strain behaviour of corrosion-damaged reinforcing bars including inelastic buckling. *Engineering Structures*, *48*, 417–429. https://doi.org/10.1016/j.engstruct.2012.09.034

Kowalsky, M. J. (2000). Deformation Limit States for Circular Reinforced Concrete Bridge Columns. *Journal of Structural Engineering*, *126*(8), 869–878. https://doi.org/10.1061/(ASCE)0733-9445(2000)126:8(869)

Mander, J. B., Priestley, M. J. N., & Park, R. (1988b). Theoretical stress-strain model for confined concrete. *Journal of Structural Engineering*, *114*(8), 1804–1826. https://doi.org/10.1061/(ASCE)0733-9445(1988)114:8(1804)

Meda, A., Mostosi, S., Rinaldi, Z., & Riva, P. (2014). Experimental evaluation of the corrosion influence on the cyclic behaviour of RC columns. *Engineering Structures*, *76*, 112–123. https://doi.org/10.1016/j.engstruct.2014.06.043

Mohammed, A. M. Y., Ahmed, A., & Maekawa, K. (2016). Effect of corrosion on ductility of RC columns. *APICENS-1433*, 13.

Montejo, L., & Kowalsky, M. (2007). CUMBIA—Set of codes for the analysis of reinforced concrete members. *CFL Technical Rep. No. IS-07*, *1*.

Montejo, L., Marx, E., & Kowalsky, M. (2010). Seismic Design of Reinforced Concrete Bridge Columns at Subfreezing Temperatures. *ACI Structural Journal*, *107*.

Muthulingam, S., & Rao, B. N. (2014). Non-uniform time-to-corrosion initiation in steel reinforced concrete under chloride environment. *Corrosion Science*, *82*, 304–315. https://doi.org/10.1016/j.corsci.2014.01.023

Priestley, M. J. N., Calvi, G. M., & Kowalsky, M. J. (2007). *Displacement Based Seismic Design of Structures* (I. Press, Ed.; First Edition). IUSS Press.

Rajput, A. S., & Sharma, U. K. (2018). Corroded reinforced concrete columns under simulated seismic loading. *Engineering Structures*, *171*, 453–463. https://doi.org/10.1016/j.engstruct.2018.05.097

Vu, N. S., Yu, B., & Li, B. (2017). Stress-strain model for confined concrete with corroded transverse reinforcement. *Engineering Structures*, *151*, 472–487. https://doi.org/10.1016/j.engstruct.2017.08.049

Yuan, Z., Fang, C., Parsaeimaram, M., & Yang, S. (2017). Cyclic Behavior of Corroded Reinforced Concrete Bridge Piers. *Journal of Bridge Engineering*, *22*(7), 04017020. https://doi.org/10.1061/(ASCE)BE.1943-5592.0001043

Zhang, Q., Zheng, N.-H., Gu, X.-L., Wei, Z.-Y., & Zhang, Z. (2022). Study of the confinement performance and stress-strain response of RC columns with corroded stirrups. *Engineering Structures*, *266*, 114476. https://doi.org/10.1016/j.engstruct.2022.114476

Zhao, Y., Karimi, A. R., Wong, H. S., Hu, B., Buenfeld, N. R., & Jin, W. (2011). Comparison of uniform and non-uniform corrosion induced damage in reinforced concrete based on a Gaussian description of the corrosion layer. *Corrosion Science*, *53*(9), 2803–2814. https://doi.org/10.1016/j.corsci.2011.05.017

# APPENDICES

# APPENDIX A: STANDARD OPERATION PROCEDURE FOR ACCELERATED CORROSION

This section outlines the standard operating procedure (SOP) for accelerated corrosion. Please exercise caution and adhere to the provided guidelines to ensure safe and effective practices. The following SOP is based off the work of Calderon (2022).

This process employs an electrolytic method to accelerate the corrosion in reinforcing steel bars. The setup includes:

- **Anode**: Made of stainless-steel mesh
- **Cathode**: Composed of the reinforcing steel bar
- **Electrolytic Solution**: Sodium chloride solution at a concentration of 0.3M (1.75% NaCl)

A current is applied to facilitate the oxidation process, and Faraday's law is utilized to calculate the time required to achieve the desired level of corrosion.

---

***Chemicals and Equipment***

The reinforcing steel bars submerged in a calcium chloride saturated solution. The required chemicals are listed below:

- Sodium chloride (NaCl)
- Distilled water

Other equipment needed:

- Beaker 500 ml
- Glass mixing rod
- Disposable 1 gallon bucket or equivalent container
- Measuring scale
- Spoon for handling chemicals
- Paper sheets for spills
- Funnel
- Stainless-steel mesh
- Stainless-steel wire

- Power supply
- Alligator clips
- Large container(s)
- Wire brush

---

***Safety Equipment***

Personal protective equipment:

- Safety glasses/goggles
- Nitrile gloves with puncture resistance
- Lab Coat

---

***Procedure***

The following procedure is for 1 liter of saturated solution. Concentrations can be multiplied by the desired volume as needed.

**Step 1: Calculate Corrosion Time**

- Determine the desired level or corrosion in the form of mass loss.
- Calculate the estimated time required to reach a desired level of corrosion, utilizing Faraday's 2nd Law of Electrolysis:

$$t = \frac{m_{loss} * n * F}{I * A_m}$$

Where:

$t = \text{time (seconds)}$

$m_{loss} = \text{mass loss (grams)}$

$n = \text{charge number}$

$F = \text{Faraday constant } (\frac{1}{mol})$

$I = \text{Current (amp)}$

$A_m = \text{Atomic mass } (\frac{\text{grams}}{\text{mol}})$

---

**Step 2: Prepare the Work Area**

- Lay packing paper on the counter or table where specimen preparation will occur.
- Place the packing paper underneath each container.

---

**Step 3: Prepare the Sodium Chloride Solution**

- Turn on the scale and ensure it is level.
- In a 1-gallon container, measure out 0.3M of NaCl (17.5 g per L of water):
    - **17.5 g of sodium chloride (NaCl)**
    - **1 L distilled water**

---

**Step 4: Saturate the Assembly**

- Place the steel specimens in the containers and surround them with the stainless-steel mesh. Fully saturate the assembly with the sodium chloride solution.

---

**Step 5: Make Electrical Connections**

- Connect the positive current from the power supply to the steel specimen using alligator clips and stainless-steel wire (See Figure A-1).
- Connect the negative current from the power supply to the stainless-steel mesh surrounding the steel specimen using alligator clips (See Figure A-1).
- Ensure all connections are secure.

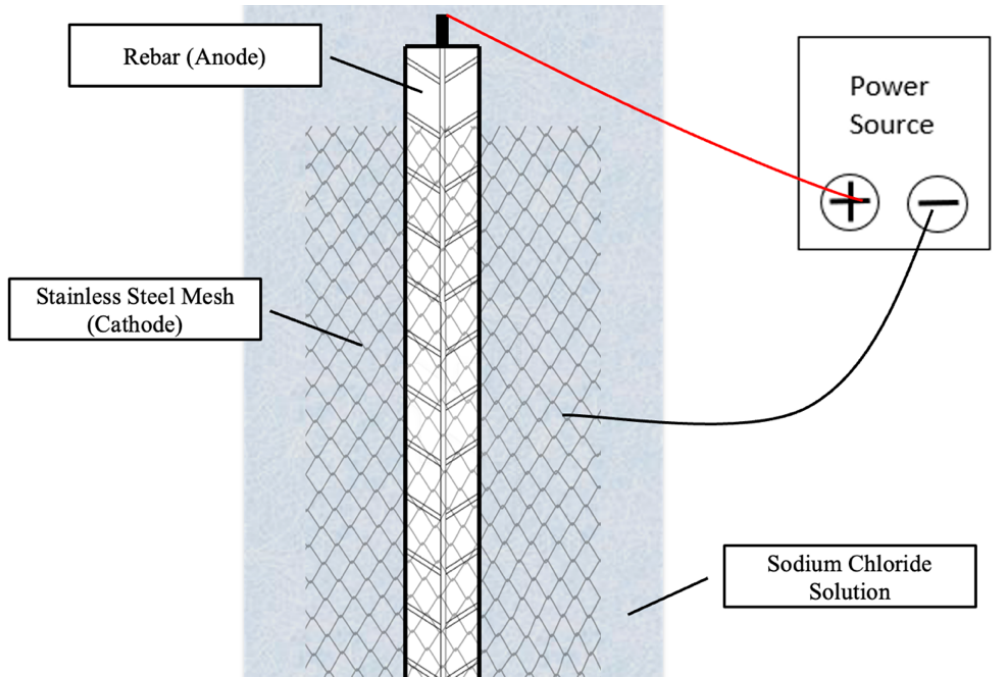



*Figure A – 1: Accelerated corrosion setup schematic*

---

**Step 6: Turn on the Power Supply**

- Set the current and voltage according to the values calculated for the desired level of corrosion, and intimate current.

---

**Step 7: Adjust Voltage if Necessary**

- If needed, adjust the voltage to maintain the desired current.

---

**Step 8: Wait for the Calculated Time**

- Allow the process to run for the time calculated using Faraday's Equation for the desired level of corrosion.

---

**Step 10: Clean Up After Corrosion**

- Follow the corrosion cleaning procedure.

---

***Cleaning Procedure***

**Step 1: Turn off Power Supply**

- Turn off power supply and wait approximately 10 seconds to allow for current to dissipate.
- Disconnect all connections to power supply

---

**Step 2: Remove and Clean Steel Specimens**

- Carefully remove the steel specimens from the containers.
- Wash and scrub the steel specimens using a wire brush and water above a designated waste container.
- Carefully pour the used sodium chloride from the large container(s) into a designated waste container.
- Clean any droplets in the working area.

---

# APPENDIX B: STANDARD OPERATION PROCEDURE FOR 3D SCANNING

This section outlines the standard operating procedure (SOP) for scanning and processing corroded steel specimens. Please note that this SOP has been specifically developed for use with the designated 3D scanner and accompanying software applications. As a result, performance and outcomes may vary depending on the specific equipment and software used, as well as the unique characteristics of each specimen. Users are encouraged to adapt the procedures as necessary to suit their individual systems and requirements.

---

***Equipment and Software***

- 3D scanner: CR-Scan Ferret
- 3D scanner software: CrealityScan (Windows, Mac, or Android)
- Laptop (Windows or Mac) or compatible mobile device
- Other software: Autodesk Fusion 360 (Windows or Mac)

---

***Procedure***

**Step 1: Prepare 3D Scanner**

- Assemble 3D scanner according to provided instructions.
- Attach the USB-C cable to the scanner and plug it into a laptop or compatible mobile device.
- Connect to the scanner: On the device, go to the Wi-Fi settings and search for the scanner's network.
- Launch the CrealityScan software: The splash page should show that the scanner is plugged in and detected.
- Name the project: Choose a name for the scan project and the folder path where the files will be saved.
- Select object options: Choose the object option that best fits your scan, the scan size, the geometry mode, the accuracy, and color mapping.

---

**Step 2: Scan**

- Position the object: Place the object on a turntable to rotate it smoothly or move the scanner itself.
- Scan: The app will show a preview image and a point cloud in real time. Follow the prompts to move the scanner at the correct distance from the target (See Figure B-1).




*Figure B-1: Scanning interface*

- Save the files.

---

**Step 3: Process 3D Scans**

- Open Autodesk Fusion 360 on a computer.
- Open the 3D scan file, which will be in stereolithography (STL) format (.stl).

- Using the various measure tools in Autodesk Fusion 360, measure the desired parameters (See Figure B-2).

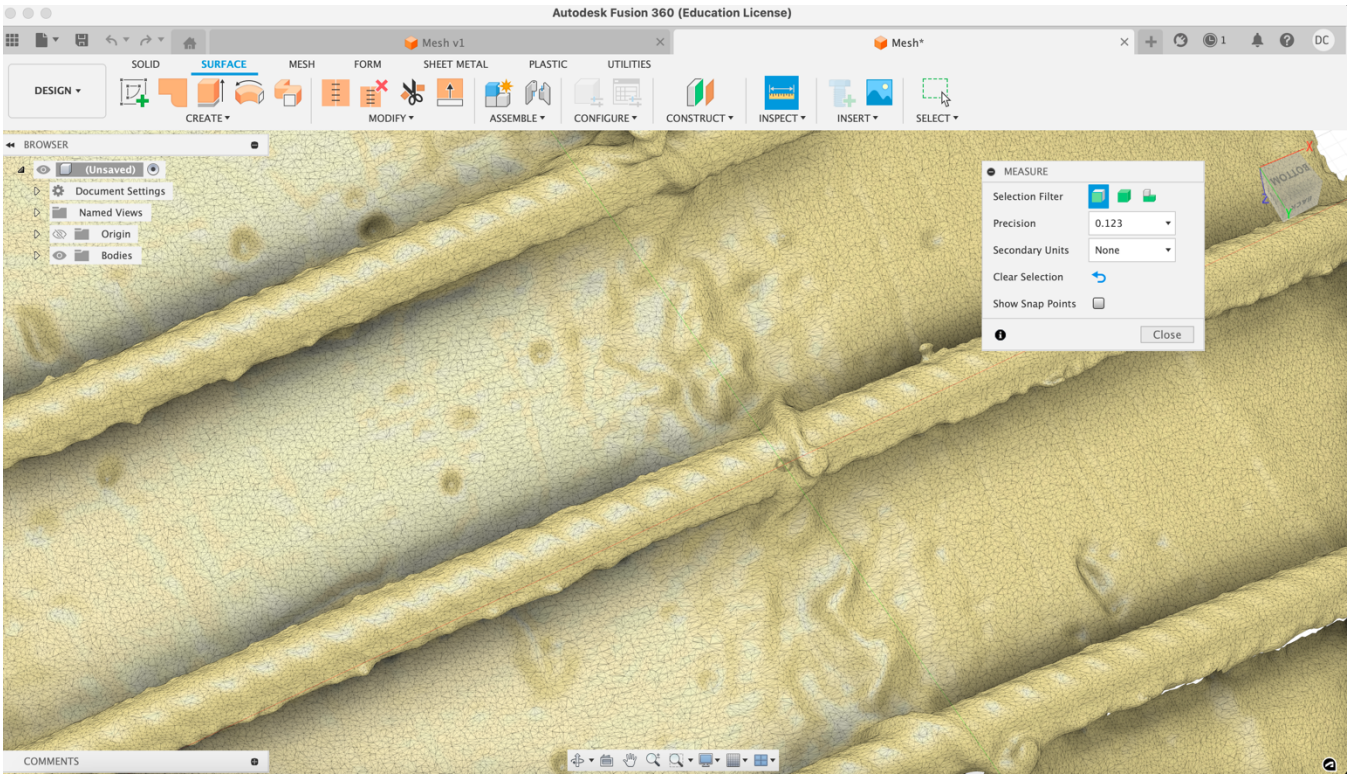



*Figure B-2: Autodesk Fusion 360 interface*

# APPENDIX C: 3D SCAN RESULTS

This section shows the results from the 3D scans. For the reinforcing steel used in the large-scale tests and material tests, pits were identified in the 3D meshes at one-inch intervals and their depths were measured. Special care was taken to identify pits that were in regions of bar fracture. The following shows the pit depth to bar diameter ratios (PDBD) of the material tests as well as large-scale tests.

***Tension Tests***

*Table C-1: Tension test scan data*

| Interval | Pit Depth to Bar Diameter Ratio (PDBD) | | | |
|---|---|---|---|---|
| | 5% Corrosion | 10% Corrosion | 30% Corrosion | 50% Corrosion |
| 1 | 0.01150 | 0.0221 | 0.0632 | 0.1132 |
| 2 | 0.01134 | 0.0229 | 0.0602 | 0.1101 |
| 3 | 0.01412 | 0.0215 | 0.0615 | 0.1130 |
| 4 | 0.01136 | 0.0210 | 0.0624 | 0.1122 |
| 5 | 0.01141 | 0.0214 | 0.0609 | 0.1105 |
| 6 | 0.01140 | 0.0217 | 0.0608 | 0.1095 |
| 7 | 0.01187 | 0.0212 | 0.0627 | 0.1129 |
| 8 | 0.01126 | 0.0238 | 0.0604 | 0.1129 |
| 9 | 0.01145 | 0.0171 | 0.0714 | 0.1293 |

***BBT Tests***

*Table C-2: BBT test scan data*

| Interval | Pit Depth to Bar Diameter Ratio (PDBD) | | | | |
|---|---|---|---|---|---|
| | 5% Corrosion | | | | |
| 1 | 0.01153 | 0.01174 | 0.01132 | 0.01158 | 0.01179 |
| 2 | 0.01121 | 0.01121 | 0.01142 | 0.01142 | 0.01126 |
| 3 | 0.01426 | 0.01400 | 0.01421 | 0.01395 | 0.01432 |
| 4 | 0.01126 | 0.01147 | 0.01163 | 0.01147 | 0.01158 |
| 5 | 0.01153 | 0.01163 | 0.01158 | 0.01126 | 0.01153 |
| 6 | 0.01126 | 0.01158 | 0.01137 | 0.01153 | 0.01174 |
| 7 | 0.01200 | 0.01205 | 0.01179 | 0.01205 | 0.01195 |
| 8 | 0.01116 | 0.01142 | 0.01116 | 0.01137 | 0.01132 |
| 9 | 0.01153 | 0.01137 | 0.01158 | 0.01158 | 0.01158 |
| 10% Corrosion | | | | | |
| 1 | 0.0223 | 0.0219 | 0.0221 | 0.0216 | 0.0222 |
| 2 | 0.0225 | 0.0231 | 0.0225 | 0.0226 | 0.0227 |
| 3 | 0.0218 | 0.0214 | 0.0216 | 0.0214 | 0.0214 |
| 4 | 0.0212 | 0.0208 | 0.0209 | 0.0213 | 0.0209 |

| | | | | | |
|---|---|---|---|---|---|
| 5 | 0.0216 | 0.0213 | 0.0214 | 0.0213 | 0.0216 |
| 6 | 0.0215 | 0.0218 | 0.0219 | 0.0216 | 0.0220 |
| 7 | 0.0210 | 0.0216 | 0.0215 | 0.0210 | 0.0211 |
| 8 | 0.0235 | 0.0241 | 0.0237 | 0.0239 | 0.0239 |
| 9 | 0.0173 | 0.0169 | 0.0173 | 0.0174 | 0.0170 |
| 30% Corrosion | | | | | |
| 1 | 0.0635 | 0.0637 | 0.0634 | 0.0628 | 0.0632 |
| 2 | 0.0599 | 0.0608 | 0.0601 | 0.0598 | 0.0605 |
| 3 | 0.0611 | 0.0617 | 0.0611 | 0.0618 | 0.0612 |
| 4 | 0.0623 | 0.0627 | 0.0621 | 0.0626 | 0.0621 |
| 5 | 0.0608 | 0.0604 | 0.0610 | 0.0606 | 0.0616 |
| 6 | 0.0607 | 0.0613 | 0.0607 | 0.0609 | 0.0610 |
| 7 | 0.0629 | 0.0625 | 0.0628 | 0.0624 | 0.0631 |
| 8 | 0.0606 | 0.0600 | 0.0602 | 0.0607 | 0.0606 |
| 9 | 0.0706 | 0.0718 | 0.0711 | 0.0709 | 0.0720 |
| 50% Corrosion | | | | | |
| 1 | 0.1145 | 0.1125 | 0.1138 | 0.1127 | 0.1131 |
| 2 | 0.1107 | 0.1098 | 0.1104 | 0.1102 | 0.1098 |
| 3 | 0.1125 | 0.1133 | 0.1119 | 0.1124 | 0.1131 |
| 4 | 0.1117 | 0.1126 | 0.1116 | 0.1120 | 0.1119 |
| 5 | 0.1100 | 0.1110 | 0.1111 | 0.1102 | 0.1109 |
| 6 | 0.1097 | 0.1091 | 0.1097 | 0.1093 | 0.1099 |
| 7 | 0.1124 | 0.1137 | 0.1125 | 0.1136 | 0.1133 |
| 8 | 0.1132 | 0.1125 | 0.1125 | 0.1134 | 0.1132 |
| 9 | 0.1295 | 0.1300 | 0.1287 | 0.1289 | 0.1298 |

***Large-Scale Tests***

*Table C-3: Large-scale scan data*

| Height Above Footing (in) | | 0.92 | 2.91 | 4.94 | 6.96 | 9.01 | 11.03 | 13.05 | 15.05 |
|---|---|---|---|---|---|---|---|---|---|
| 5% Corrosion | S2 | 0.01134 | 0.01136 | 0.01140 | 0.01126 | 0.01137 | 0.01137 | 0.01135 | 0.01136 |
| | S3 | 0.01129 | 0.01130 | 0.01132 | 0.01132 | 0.01147 | 0.01136 | 0.01137 | 0.01131 |
| | S4 | 0.01135 | 0.01136 | 0.01151 | 0.01150 | 0.01131 | 0.01139 | 0.01136 | 0.01140 |
| | N2 | 0.01126 | 0.01145 | 0.01139 | 0.01140 | 0.01151 | 0.01143 | 0.01132 | 0.01141 |
| | N3 | 0.01139 | 0.01122 | 0.01145 | 0.01147 | 0.01139 | 0.01142 | 0.01142 | 0.01150 |
| | N4 | 0.01135 | 0.01145 | 0.01146 | 0.01140 | 0.01150 | 0.01139 | 0.01137 | 0.01135 |
| | S2 | 0.02207 | 0.02129 | 0.02155 | 0.02103 | 0.02141 | 0.02169 | 0.02119 | 0.02190 |

| | | | | | | | | | |
|---|---|---|---|---|---|---|---|---|---|
| 10% Corrosion | S3 | 0.02141 | 0.02194 | 0.02115 | 0.02169 | 0.02190 | 0.02162 | 0.02213 | 0.02165 |
| | S4 | 0.02156 | 0.02210 | 0.02132 | 0.02121 | 0.02151 | 0.02152 | 0.02141 | 0.02169 |
| | N2 | 0.02165 | 0.02125 | 0.02105 | 0.02182 | 0.02169 | 0.02140 | 0.02188 | 0.02173 |
| | N3 | 0.02160 | 0.02173 | 0.02188 | 0.02160 | 0.02190 | 0.02146 | 0.02171 | 0.02161 |
| | N4 | 0.02174 | 0.02184 | 0.02124 | 0.02158 | 0.02188 | 0.02130 | 0.02181 | 0.02147 |
| 30% Corrosion | S2 | 0.06021 | 0.06244 | 0.06084 | 0.06042 | 0.06192 | 0.06076 | 0.06123 | 0.06083 |
| | S3 | 0.06141 | 0.06220 | 0.06197 | 0.06124 | 0.06196 | 0.06187 | 0.06144 | 0.06124 |
| | S4 | 0.06089 | 0.06029 | 0.06123 | 0.06149 | 0.06035 | 0.06047 | 0.06071 | 0.06252 |
| | N2 | 0.06095 | 0.06147 | 0.06125 | 0.06100 | 0.06112 | 0.06049 | 0.06228 | 0.06154 |
| | N3 | 0.06144 | 0.06095 | 0.06167 | 0.06165 | 0.06244 | 0.06149 | 0.06213 | 0.06150 |
| | N4 | 0.06209 | 0.06159 | 0.06088 | 0.06192 | 0.06229 | 0.06102 | 0.06079 | 0.06095 |
| 50% Corrosion | S2 | 0.11012 | 0.11223 | 0.10951 | 0.11290 | 0.11170 | 0.10994 | 0.11239 | 0.11230 |
| | S3 | 0.11248 | 0.11035 | 0.11091 | 0.11003 | 0.11216 | 0.11114 | 0.11091 | 0.11088 |
| | S4 | 0.11096 | 0.11088 | 0.11300 | 0.11180 | 0.11279 | 0.11281 | 0.11287 | 0.11219 |
| | N2 | 0.11254 | 0.11280 | 0.11060 | 0.11224 | 0.11247 | 0.11159 | 0.11216 | 0.11165 |
| | N3 | 0.11234 | 0.11221 | 0.11268 | 0.11234 | 0.11209 | 0.11224 | 0.11296 | 0.11239 |
| | N4 | 0.11292 | 0.11034 | 0.11258 | 0.11209 | 0.11237 | 0.11247 | 0.11148 | 0.11186 |

Note: The red values are the locations of bar fracture

# APPENDIX D: DATA FROM PREVIOUS RESEARCH

The following appendix presents data from previous research conducted at NC State. This section aims to provide comparisons with the research presented in this report. Figure D-1 compares the force-displacement responses of a previously tested column with identical detailing and no corrosion (Goodnight et. al 2015, Test 19), to the force displacement response of the column with 5% corrosion.

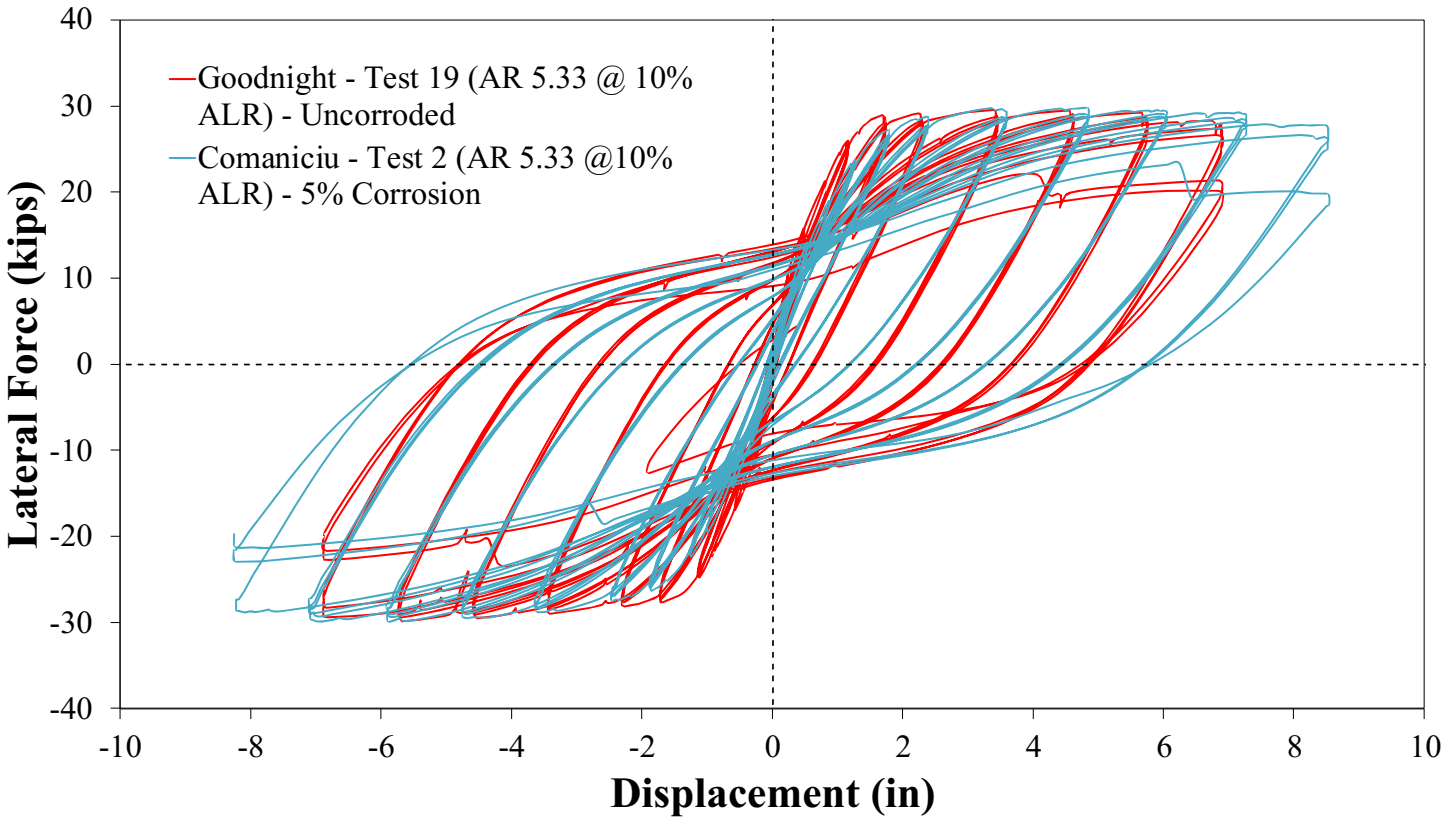



*Figure D-1: Force-displacement response comparison*

As shown in Figure D-1, the column with 5% corrosion performed similarly to the uncorroded column, despite the corrosion. This comparable performance can be attributed to differences in material strengths and construction methods. For this reason, the column with 5% corrosion was selected as the baseline for this research project.

Table D-1 presents BBT results from Barcley Kowalsky (2019), while Table D-2 shows the BBT results from this research project. Table D-1 includes Grade 60 and Grade 80 steel specimens from various manufacturing processes. The results in Table D-1 specifically pertain to Grade 60 micro-alloy steel.

*Table D-1: BBT results – Barcley and Kowalsky (2019)*

| Mill | Manufacture Process | Designation | Critical Bending Strain |
|---|---|---|---|
| 1 | Micro-alloying | Grade 60 | 0.14 |
| | | Grade 80 – v0 | 0.14 |
| | | Grade 80 – v1 | 0.10 |
| | | Grade 80 – v2 | 0.13 |
| | | Grade 80 – v2b | 0.10 |
| 2 | Micro-alloying | Grade 60 | 0.14 |
| | | Grade 80 – v0 | 0.14 |
| | | Grade 80 – v1 | 0.16 |
| 3 | Quench and Self-Tempered | Grade 80 – #5 | 0.14 |
| | | Grade 80 – #6 | 0.14 |

*Table D-2: BBT results – Comaniciu (2024)*

| Corrosion Level | Critical Bending Strain, $e_{cr}$ (in/in) |
|---|---|
| 5% | 0.115 |
| 10% | 0.085 |
| 30% | 0.045 |
| 50% | 0.019 |

Figure D-2 shows the bending strain history for uncorroded columns with detailing identical to that of the columns tested in this research project. Figure D-3 displays the bending strain history for the corroded columns tested in this research project.

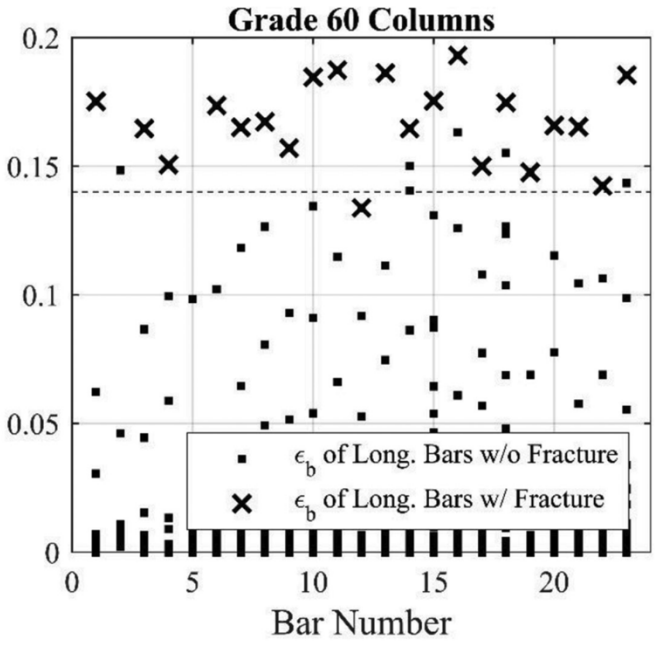



*Figure D-2: Bending strain history – Barcley and Kowalsky (2019)*

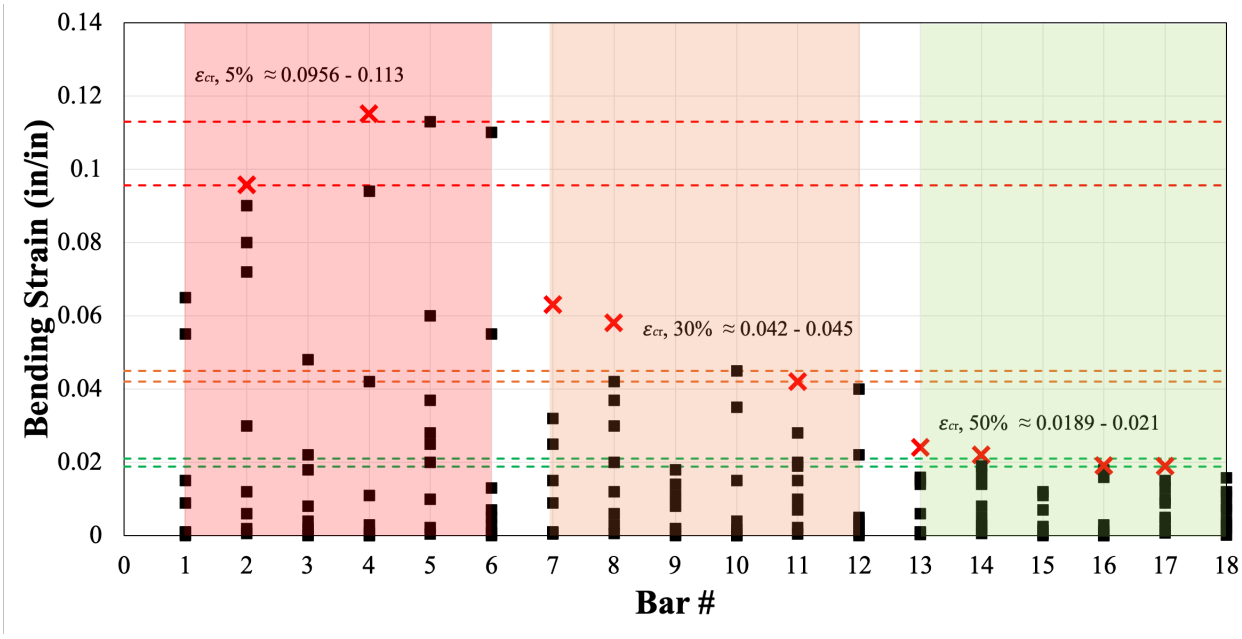



*Figure D-3: Bending strain history – Comaniciu (2024): red – 5% corrosion; orange – 30% corrosion; green – 50% corrosion*